Numerical Modelling of Thermally Induced Regional and Local Scale Flows in MacKenzie Basin, New Zealand

A thesis
submitted in fulfillment
of the requirements for the degree
of
Doctor of Philosophy
in the
University of Canterbury

by

Peyman Zawar-Reza

University of Canterbury
2000

Table of Contents

Chapter 3

Chapter 4

Chapter 5

List of Figures

List of Tables

List of Symbols

Symbol	Description
C_d	drag coefficient
C_p	specific heat of air at constant pressure
C_v	specific heat of air at constant volume
e	turbulent kinetic energy
ε	viscous dissipation
ε	emissivity
F	longwave radiation flux
f	coriolis parameter
g	gravitational acceleration
H	height of the model top
k	Von Karman constant
K_e	vertical eddy diffusivity for turbulent kinetic energy
K_h	vertical eddy diffusivity for heat
K_m	vertical eddy diffusivity for momentum
L	latent heat of vaporization
l	turbulent master length scale
N_{BV}	Brunt-Väisälä frequency
P_b	buoyancy production term for turbulent kinetic energy
P_s	shear production term for turbulent kinetic energy
π	Exner function
π_0	synoptic scale reference value for Exner function
Q_E	latent heat flux
Q_G	heat flux from soil
Q_H	sensible heat flux
Q^*	net radiation
q_s	surface mixing ratio
q_a	mixing ratio of air close to ground
R	ratio of drag coefficient for momentum and heat (Businger *et al.* 1971)
R	gas constant for dry air
R_j	expansion ratio for vertical grid spacing
ρ	air density
ρ_0	synoptic scale reference value for air density
σ	Stefan-Boltzmann constant
T_v	virtual temperature
T_{zo}	extrapolated roughness value for temperature
θ	potential temperature
θ_{il}	ice-liquid water potential temperature
θ_v	virtual potential temperature
θ_0	synoptic scale reference value for potential temperature
θ_{zo}	extrapolated roughness length for potential temperature
θ_*	potential temperature scale
r_n	water species mixing ratio
r_*	mixing ratio scale
R_{ib}	bulk Richardson number

S_e	nondimensional eddy diffusivity for turbulent kinetic energy
S_h	nondimensional eddy diffusivity for heat
S_m	nondimensional eddy diffusivity for momentum
ϕ	dependent variables in formulations of the model
T_a	air temperature close to ground
T_s	surface temperature
U	wind speed
u	east-west component of the wind velocity
u_*	velocity scale
v	north-south component of wind velocity
w	vertical component of wind velocity
z	topography height
z_g	local topography height
z_o	roughness length

Acknowledgements

First, I would like to offer my sincere thanks to all those who have helped, and there have been many. I would especially like to thank Associate Professor Andy Sturman for his support as my supervisor. His guidance and wisdom (plus his ability to cook a tremendous cheese sauce) have been invaluable throughout the process of my Ph.D. endeavour. I would also like to thank Dr Dave Whiteman for sponsoring my stay in Pacific Northwest National Laboratories, and Drs Jerome Fast and Shiyuan Zhong for assistance with numerical modelling. Paul Gudiksen and Wayne Stephenson endured hazardous flying conditions during the field campaign, hopefully the experience did not shave too many years off their life spans, thank you for your assistance. Dr Meinolf Kossmann and Andrew Oliphant, thank you also for your friendship and moral support as well as the discussions of a more technical nature.

I would also like to thank Jane Harrison and Julie Cupples for helping me through difficult times, and Chandra Harrison for technical assistance. Maria Borovnic was of great help with her knowledge in Shiatsu.

Financial assistance for this research was provided under the project 'Local and Regional Wind Systems', funded by Marsden fund contract UOC602. I would like to thank all participants in this project for their assistance in fieldwork.

The Department of Geography has also assisted with technical and administrative support, both for the fieldwork necessary to gather the data I have used, and with a friendly supportive environment. Thank you to all the individuals in the department that have made this process bearable.

Abstract

Atmospheric flows that result from surface heating and cooling in complex, mountainous terrain encompass many scales. These flows are induced by horizontal thermal gradients in the atmosphere associated with topographic relief, and are most pronounced when synoptic pressure gradients are weak. At the small-scale end of the spectrum there are slope and along-valley winds, and at the larger scale there are plain-to-basin and plain-to-plateau flows.

The intrusion of a recurring plain-to-basin wind system named the Canterbury Plains Breeze (CPB) into the MacKenzie Basin and Lake Tekapo region is described using both observational data and results from a numerical model. Observational data from a surface monitoring network designed to investigate local flows in the Lake Tekapo area show that the CPB has an important influence on the wind regime in this region. An atmospheric mesoscale numerical model was utilized to investigate the origin and forcing mechanisms for this flow.

The mesoscale model was able to successfully simulate the CPB for a case study day using realistic synoptic scale winds. To isolate the major forcing mechanisms for this flow, additional idealized two- and three-dimensional numerical experiments were conducted. The idealized three-dimensional runs showed that the CPB is a not a sea breeze intrusion into the MacKenzie Basin as was previously thought, and could be generated by orography alone.

The two-dimensional runs showed that although the sea breeze outside the basin does not have a direct impact on the CPB, it can influence the current's intensity by suppressing the mixed layer growth outside the basin, which increases the horizontal

temperature gradient that forces the CPB. Other surface effects, such as soil moisture content and land use also seem to affect the characteristic features of the plain-to-basin flow.

In addition, two high-resolution simulations were performed to investigate the interaction of the CPB with locally generated thermal flows around Lake Tekapo, where the surface monitoring network was established. Results show that early in the afternoon the CPB flows into the region as gap winds through the saddles in the Two Thumb Range, dominating the local winds. These gap winds are localized in nature, and the model runs suggest that the monitoring network was not dense enough to adequately describe the surface flow field around the lake.

It is evident from this research that regional circulation systems, such as the CPB, could transport air pollutants significant distances from the coastal plains, over complex terrain into the relatively pristine environment of the South Island's mountain basins. A knowledge of the physical forcing mechanisms involved in such flows can therefore have important practical applications for air quality issues.

Chapter 1

Introduction

1.1 Background

This thesis attempts to determine the dominant physical mechanisms responsible for the formation of the regional scale Canterbury Plains Breeze (CPB) and its interaction with other, local scale wind systems during settled weather in spring and summer with an atmospheric mesoscale numerical model. This wind system was observed during a field campaign to study local airflows in MacKenzie Basin in the South Island of New Zealand. The airflow originates from atmospheric thermal contrasts between the Canterbury Plains and MacKenzie Basin, the wind is usually of moderate intensity (6 – 12 ms^{-1}) and blows throughout the basin dominating the locally generated circulations. Although its existence to local inhabitants is well known and its disruptive nature disliked by them, previous meteorological studies in the area paid little attention to it, since it was believed to be the inflow of a sea breeze circulation which originates at the coast and then propagates towards the mountain ranges. A visual clue to the existence of the CPB is the formation of waterfall clouds over mountain saddles, which is common on days with quiescent synoptic weather conditions.

1.2 Impetus for Research

The importance of local air circulations for air pollution transport, weather forecasting, and land-use management has been realized in the past four decades. Thermally driven circulations, such as sea breezes and diurnal orographically induced winds, result from an interplay between topographic and thermal forcings. Over simple terrain, these wind systems can be forecast with a high degree of skill since the underlying physical mechanisms that drive them are well understood, and adequately formulated in atmospheric models. An extensive set of earlier literature reviews are provided by Defant (1951) and Flohn (1969), while books by Oke (1992), Atkinson (1981), Barry (1992), and Whiteman (2000) provide suitable in-depth description of these flow systems.

Tourism has long been a part of the economy of MacKenzie Basin, as Mt. Cook/Aoraki and the nearby glaciers are a major attraction for tourists during summer months (Morris *et al.* 1997). Furthermore, the basin provides a focus for hunting, tramping and climbing. The Department of Conservation (DOC) estimates that around 240,000 visitors pass through the area each year. Therefore a knowledge of wind systems that could potentially degrade the air quality in the basin is important. Although no air polluting sources are currently located within the basin, the Canterbury Plains Breeze is capable of transporting large volumes of air from outside the region. Recently, degradation of air quality in basins has been a major concern in Japan (Kurita *et al.* 1990). Even though no local sources of air pollution exist in these basins, high concentrations of air pollutants are often recorded at night. A wind system (analogous to the CPB that flows in the MacKenzie Basin) is presumed to be an important component in transporting polluted air from large industrialized plains outside the Japanese basins (Kimura and Kuwagata, 1993). Hence, these circulations have the potential to transport air pollutants across large distances and degrade air quality in pristine mountainous areas. A knowledge of such a persistent wind system can also aid in flight safety for local aircraft operators, forecasting early morning clouds (often the CPB transports moist coastal air into the basin which, combined with nocturnal cooling of the basin atmosphere, leads to the formation of a basin-wide low stratus cloud in the morning), and soil erosion.

To determine the physical mechanisms responsible for producing a persistent circulation such as the CPB, a numerical modelling approach was chosen. Numerical models can generate dense datasets which can be compared with observational data. A great attraction of modelling approaches is the ability to do sensitivity analysis of interested phenomena, with key physical forcings being added to, or removed from the model runs thereby allowing an assessment of their contribution in driving (forcing) the phenomena. A mesoscale model is utilized in this way in this thesis.

1.3 Atmospheric Scales of Motion

Meteorologists have found it convenient to categorize atmospheric circulations according to their space and time scales, so that they essentially "quantize" the atmosphere. This "quantum view" is supported by spectral analysis of wind speed data which shows strong peaks at frequencies ranging from a few weeks (the planetary scale) to a few days (the synoptic scale). There are also peaks at 1 year, 1 day (diurnal) and a few seconds time scales (Vinnichenko 1970). Therefore, weather phenomena can range from large scale global circulation systems that extend around the Earth to the small eddies responsible for breaking up cigarette smoke. Figure 1.1 presents scales of atmospheric motion for micro and mesoscales as suggested by Orlanski (1975). According to his classification, mesoscale atmospheric phenomena have horizontal scales between 200 m to 2000 km with typical time scales ranging from minutes to days respectively. The primary scales of interest for this thesis are meso-γ and meso-β. The term *mesoscale* was first coined by radar meteorologist Ligda (1951) to describe phenomena that had spatial scales too small to resolve by conventional observations at the time (less than the spacing between cities). Mesoscale circulations include diurnal wind systems such as mountain winds, sea/land (lake/land) breezes, and thunderstorms. Due to the nature of their scale, mesoscale phenomena cannot be studied with the established synoptic network of rawinsondes that exist all over the globe, so that mesoscale meteorologists use dense networks of surface monitoring equipment, balloon-borne sounding systems, remote sensing systems and instrumented aircraft to investigate characteristic features of weather at this scale.

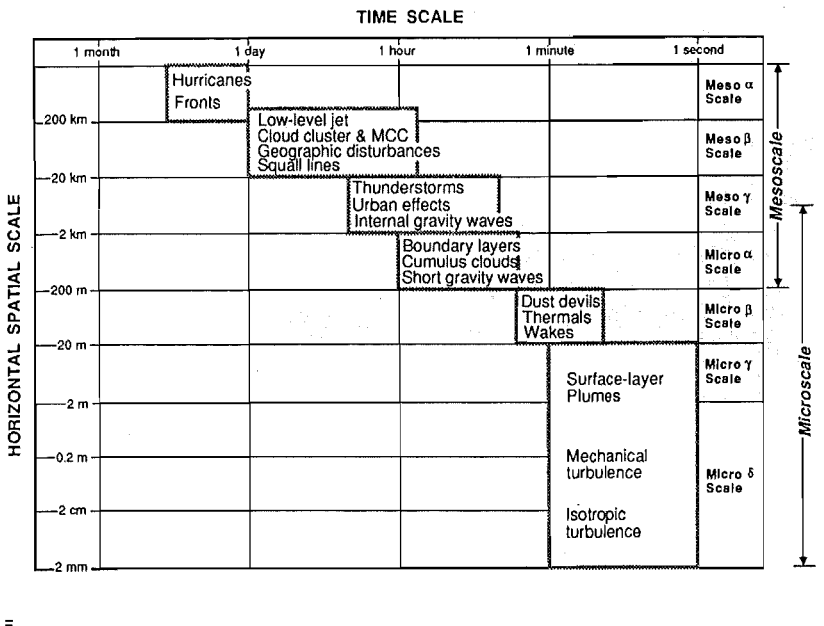

Figure 1.1: Time and space orders-of-magnitude for micro- and mesoscales (after Orlanski, 1975).

1.4 Physiographically Forced Mesoscale Circulations

Earth's surface is the only natural boundary for the atmosphere, and there is a constant exchange of momentum and energy between the two. In mountainous terrain, two types of mesoscale circulation are generated by the interaction between the atmosphere and topography. Terrain-forced flows are the result of dynamical modification of large-scale winds by complex terrain, and thermally-forced flows are produced by horizontal variations in temperature caused by underlying terrain characteristics (Pielke 1984; Whiteman 2000).

1.4.1 Terrain-Forced Flows

When an air current approaches a mountain barrier, it can either flow over it, go around it, or flow through any gaps. If the air mass is stably stratified, standing mountain waves and propagating lee waves can develop in air moving over it (Barry 1992). Because analytic solutions for the two-dimensional case of this type of flow are available, it has been the most extensively numerically simulated phenomenon.

Numerical model results are compared with analytic solutions to test model performance (Lee *et al.* 1989). When an air mass is neutrally or unstably stratified, it can flow over obstacles easily.

When air flows through mountain passes and gaps it is called a gap wind. Gap winds exist because a trans-mountain pressure gradient directs the flow from one side to the other through the gap. The pressure gradient can form as a result of the interaction of synoptic systems with the mountains and/or thermal influences, such as differential heating rates (Doran and Zhong 2000). When a regional scale circulation such as the CPB flows across a mountainous area, part of it can go through gaps and be modified by the local topography leading to strong winds (Figure 1.2).

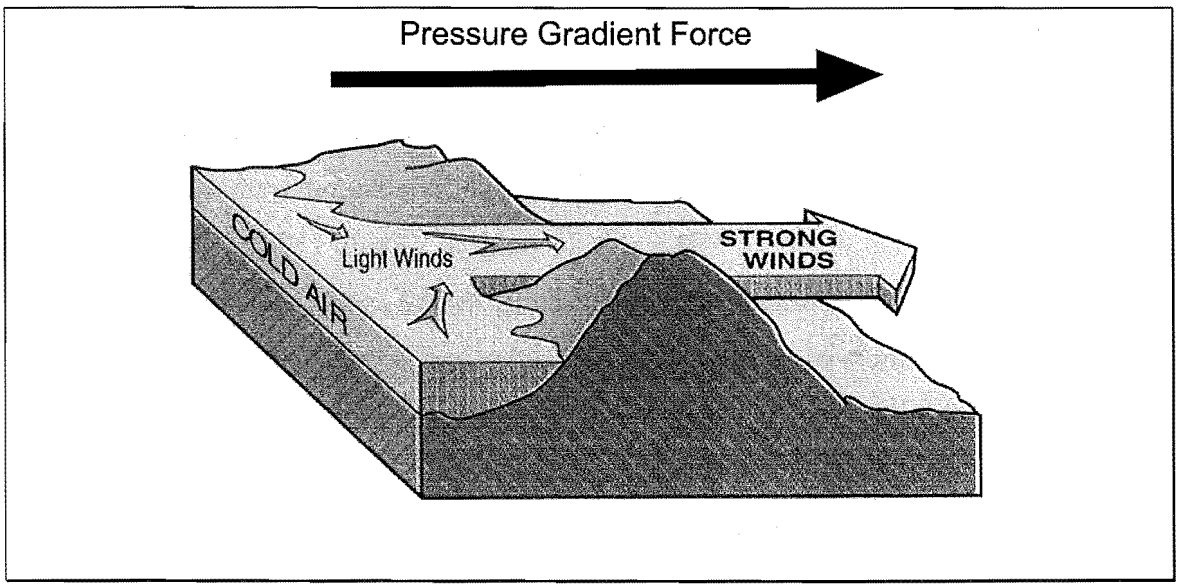

Figure 1.2: Gap winds blow through mountain passes in response to trans-mountain pressure gradient forces (after Whiteman, 2000).

1.4.2 Thermally-Forced Flows

Thermally-forced or thermally-induced circulations result from horizontal temperature gradients caused by spatial variations in the surface energy budget over landscape. These variations originate as a combination of:

- variations in surface thermal properties resulting in differential surface heating (e.g. producing a sea breeze type circulation over flat terrain)

- topography of higher elevation acting as an elevated heat source or sink (causing slope flows).
- surface relief creating a volume heating effect during day and cold air drainage at night (e.g. causing along-valley winds)

The development of scientific inquiry into thermally forced flows in mountainous terrain has evolved along the horizontal scale of the phenomena, from small to large scale. Early observations focused on the small-scale end of the spectrum, starting with observations of slope flows (upslope/downslope or anabatic/katabatic winds). Theoretical explanation of these winds was developed with reference to Bjerknes circulation theorem (Jeffreys 1922). In later years, Wagner (1938) and Defant (1951) expanded the earlier theories with the inclusion of more realistic forcing mechanisms. More recent observations have shown that thermally induced diurnal flows can also be developed at meso-β to meso-α scales (20-2000km), with Tyson and Preston-Whyte (1972) describing a diurnally reversing circulation system between the Natal coast and the Drakensburg Plateau. Yet, Tang and Reiter (1984) gave evidence for a thermally induced circulation that is caused by even larger scale land masses, the plateau-scale circulation of western United States and Tibet. Also, Bannon (pers. comms.) has shown that the Asian monsoon is primarily forced by the heating of the Tibetan Plateau in summer, which acts as an elevated heat source.

The following sections provide a brief descriptive review of thermally forced flow systems that are often observed in MacKenzie Basin and the surrounding regions. These include sea/land breezes over the Canterbury Plains (Sturman and Tapper 1996, McKendry *et al.* 1986), and diurnal mountain winds and lake/land breezes in the MacKenzie Basin (McGowan *et al.* 1995; McGowan and Sturman 1996). A mathematical description is intentionally avoided since general equations formulated for mesoscale atmospheric flows are presented in Chapter 3. These equations together with various physical parameterizations can be numerically solved to provide a more analytic description of the flow systems described below.

a) Sea/Land (Lake/Land) Breezes

Sea and land breezes over flat terrain have been the most studied mesoscale phenomena, a sea (lake) breeze is defined to occur when wind is blowing onshore, whereas a land breeze occurs when wind is blowing in the opposite direction (Atkinson 1981). Defant (1951) offered a qualitative description of sea and land breezes for a situation when large scale synoptic influences are negligible, and assuming no initial pressure gradients (Figure 1.3a). Lake/land breezes can also be described in the same way. The sequence of events is as follows:

- late in the morning, an offshore pressure gradient force is created aloft due to turbulent heating and mixing of the air over land. The isobars over water remain flat since the water surface is not heated as quickly (Figure 1.3b)
- the offshore flow aloft creates a low-pressure region at ground level causing onshore movement of air near the surface (Figure 1.3c)
- the sea breeze advects cooler air onshore, thereby advecting the perturbation to the horizontal pressure gradient some distance inland depending on total heat input to the air and the latitude. The pressure gradient remains strongest at the coastline (Figure 1.3d)
- when the sun sets, longwave radiational cooling becomes the dominant forcing mechanism, allowing the sea breeze to remove the pressure gradient (Figure 1.3e)
- continued surface cooling results in the formation of a high-pressure region aloft over the water which causes the formation of a pressure gradient force directed onshore aloft (Figure 1.3f)
- since air mass is being lost aloft over the water, a low-pressure region is formed near the surface over the water causing the land breeze to blow across the coastline (Figures 1.3g, h).

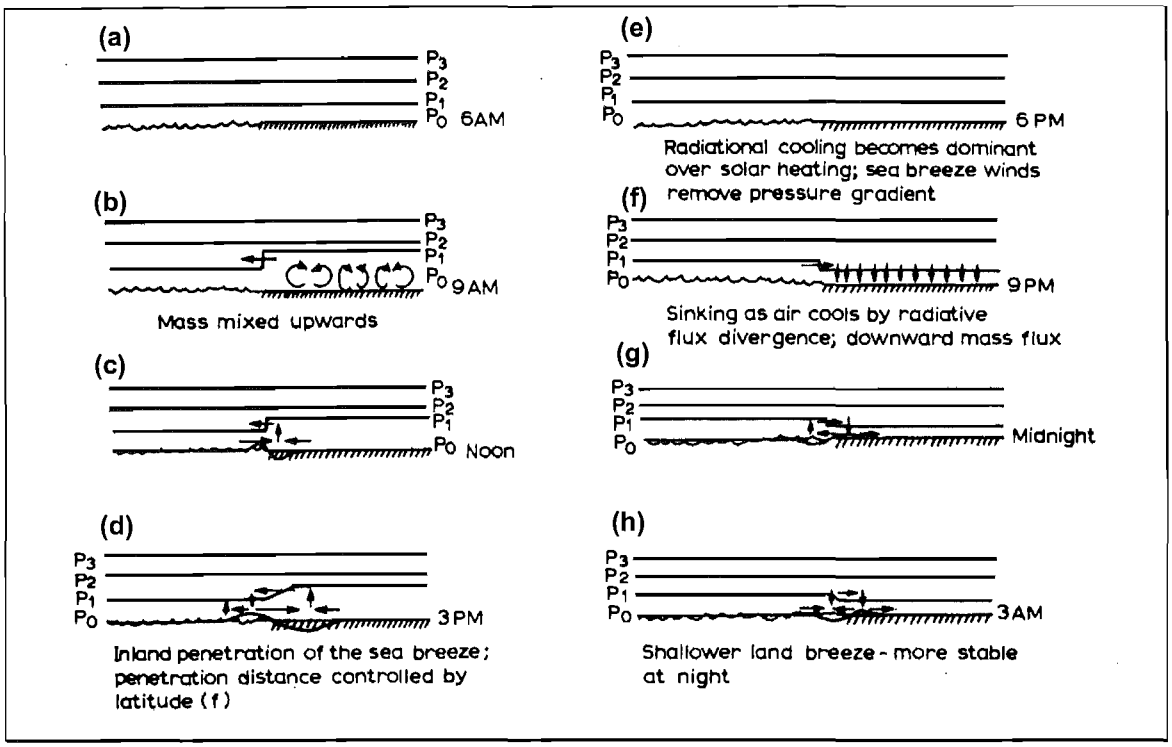

Figure 1.3: Schematic of the diurnal evolution of the sea and land breezes when synoptic pressure gradients are small (after Pielke, 1984).

b) Diurnal Mountain Winds

Literature dealing with atmospheric processes in complex terrain contains numerous alternative terms referring to the same phenomena. This thesis adopts the terminology used by Whiteman (2000), who provides an excellent description of thermally driven diurnal winds in mountainous terrain. He recognized four types of wind system (Figure 1.4):

- The slope wind system comprising of upslope (anabatic) and downslope (katabatic) winds. These winds occur due to horizontal temperature differences between the air close to valley sidewalls and the air over the centre of the valley
- Cross-valley winds, produced by horizontal temperature differences between the air over opposing sidewalls (not illustrated in Figure 1.4). These occur particularly in north-south oriented valleys during morning and evening, when marked contrasts occur in incoming solar radiation.

- Along-valley winds comprised of up-valley (valley) and down-valley (mountain) winds. These winds are induced by horizontal temperature gradients along the valley axis or between the valley and adjacent plains
- The mountain-plain wind system, which results from a horizontal temperature gradient between air over a mountain massif and the air over the surrounding plains.

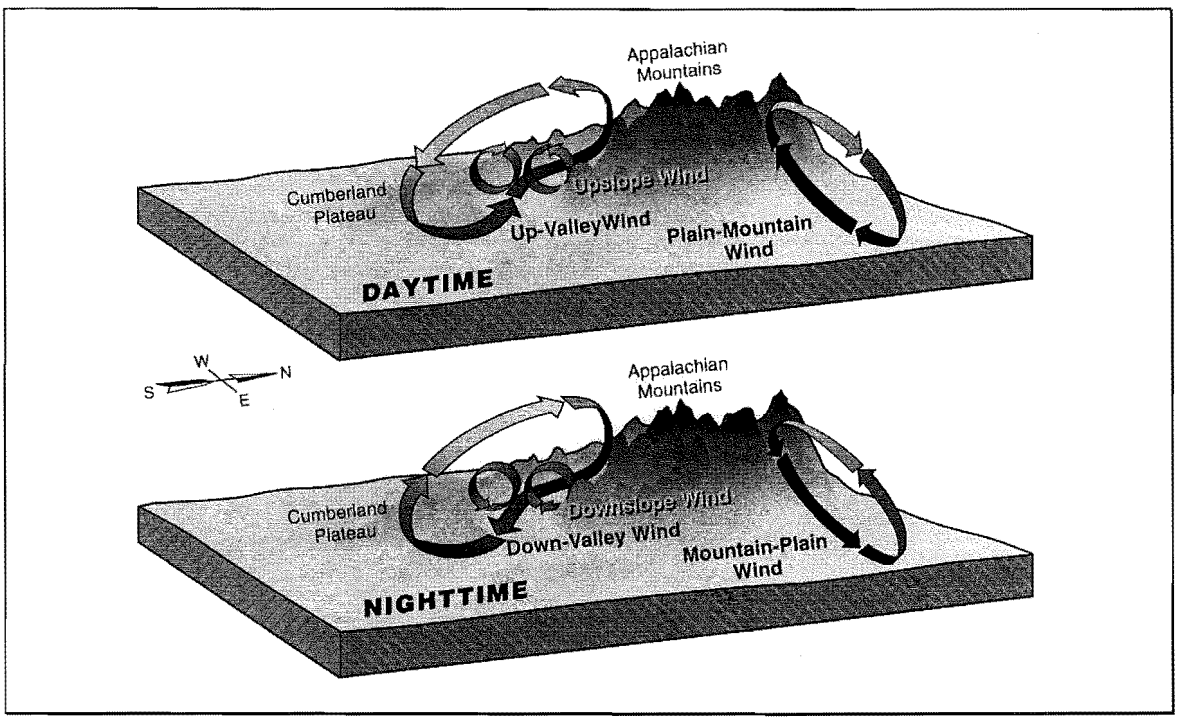

Figure 1.4: Schematic of three interacting diurnal mountain wind systems. Cross-valley flows are not shown in this figure (after Whiteman, 2000).

The principle mechanism in creating a horizontal temperature gradient within valleys can be explained by the concept of a Topographic Amplification Factor (TAF), or volume effect. In an idealized two-dimensional geometry, TAF can be simply defined as the ratio of the area enclosed by the topography in a valley (or a basin) to an area enclosed by an equal-width over an adjacent flat plain area (Steinacker 1984; Whiteman 1990). Assuming equal shortwave/longwave radiation input/output at the top, the atmosphere in the valley (basin) is heated/cooled to a greater degree because it contains less air (Figure 1.5). Therefore during the day, a pressure gradient force directs air into the valley resulting in an up-valley wind (Figure 1.6a), and at night the pressure gradient force reverses leading to a down-valley wind (Figure 1.6b). This is presumably enhanced by cold air drainage, as cold, dense air moves towards low points in the terrain under the influence of gravity.

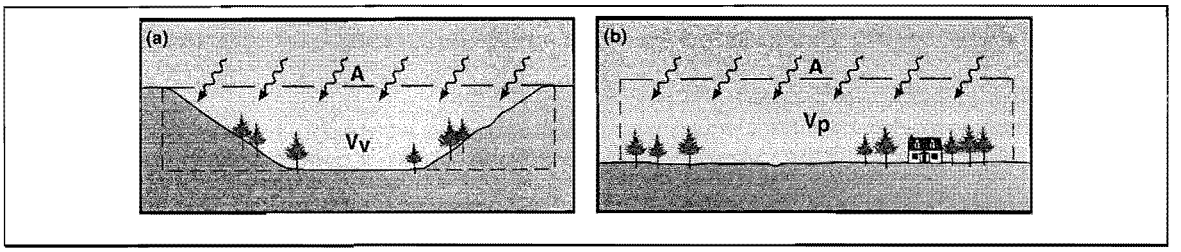

Figure 1.5: Topographic Amplification Factor (TAF). a) The volume of air in the valley (V_v) is smaller than b) the volume of air in a cross section of plains (V_p) given the same area at the top (after Whiteman 2000).

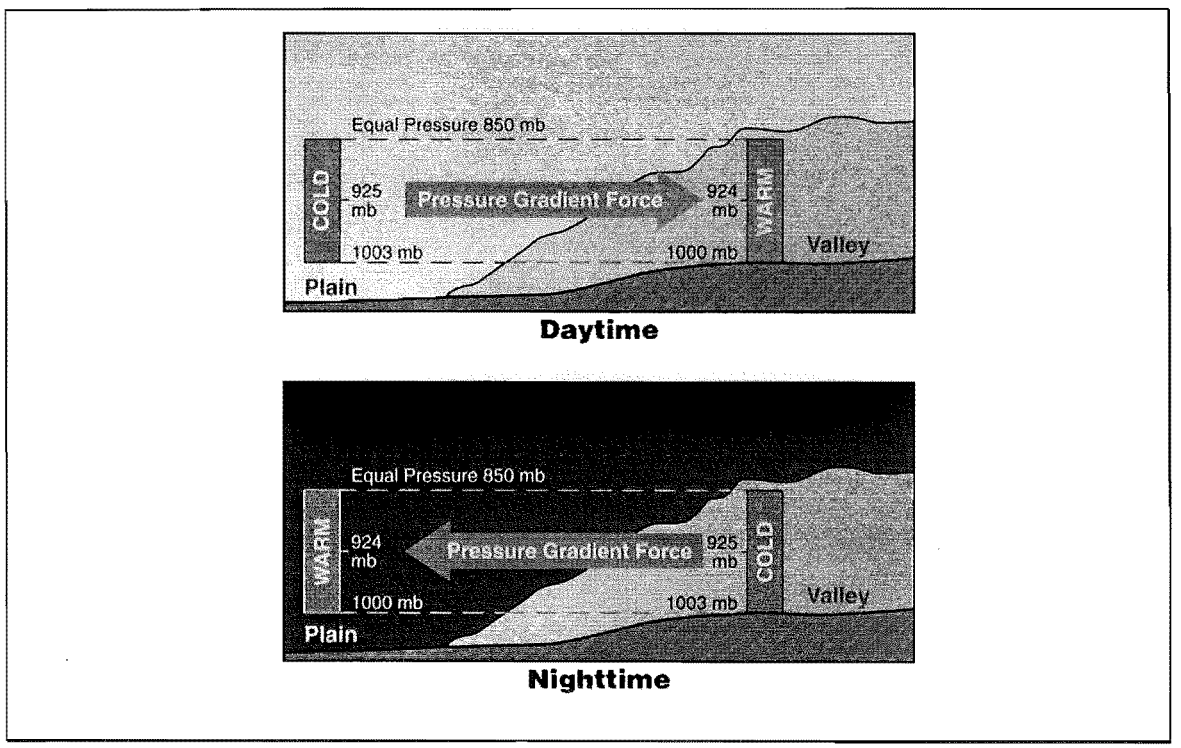

Figure 1.6: Horizontal pressure gradients produce the along-valley wind systems. During the day (night) the atmosphere inside the valley is warmer (colder) than over the plains leading to a lower (higher) pressure in the valley (after Whiteman, 2000).

The mountain-plain circulation develops because the slopes of the mountain massif can act as an elevated heat source/sink and create horizontal temperature gradients between the air over the massif and the nearby plains (Whiteman 1990; Whiteman 2000; Barry 1992). The intensity of this wind system is usually quite weak (< 2 ms^{-1}), and the flow can easily be masked by the prevailing synoptic flow.

c) *Regional Scale Plain-to-Basin Circulations*

Basins can be defined as valleys that have circular or oval shapes. If the basin is broken by deep openings (i.e. passes or saddles), or if mountain ranges on one side of the basin are lower than other sides, a plain-to-basin circulation can easily develop (Kurita *et al.* 1990; Whiteman 2000), with thermally generated gap winds occurring through the passes. This type of circulation has similar origins to the along-valley wind systems. However, if the basin is surrounded by high passes, upslope flows may develop over the basin sidewalls during the day in opposition to the plain-to-basin flow, restricting the penetration of air from outside. Cessation of these upslope winds later in the day (when sensible heat flux reverses) allows a plain-to-basin wind to flow into the basin (De Wekker *et al.* 1998). The coastal ranges that surround MacKenzie Basin contain many passes and gaps, so that the Canterbury Plains Breeze is able to flow through these gaps. It can therefore be categorized as a thermally driven gap wind in this situation (Doran and Zhong 2000). The CPB can also pour into the basin over the ridge crests as the observations show. The principle driving mechanism for the plain-to-basin wind is the horizontal temperature gradient that forms between the air over the basin and the air outside the basin at the same altitude (Doran and Zhong 1994; Doran and Zhong 2000; Whiteman *et al.* 2000). Basin atmospheres often show a larger diurnal temperature range than the atmosphere over a nearby plain at the same elevation (Kondo *et al.* 1989).

If the horizontal scale of the basin is small, a plain-to-basin wind can be classified as a local scale flow, as studied by Whiteman *et al.* (1996) and Fast *et al.* (1996). However, if a basin occupies an extensive area and is a dominating landscape feature in an area, it can exert a major regional meteorological influence. In this case, the flow systems induced by basin topography can be classified as regional.

1.4.3 Regional Scale Winds in the Context of MacKenzie Basin

Throughout the text of this thesis, terms such as local and regional scale flows will be used to describe certain wind systems. Therefore an explanation of these terms in the context of circulation systems observed and modelled in MacKenzie Basin is appropriate at this stage. MacKenzie Basin has a radius of about 30 km, it contains a number of glacially excavated valleys, and Lake Tekapo (the experimental site) is

situated in one such valley. Wind systems that are thermally induced by spatial scales smaller than the basin are referred to as *local scale*, these include lake/land breezes, slope winds, and along-valley winds. Winds generated by thermal contrasts between MacKenzie Basin and the Canterbury Plains (i.e. of a spatial scale larger than the basin) will be referred to as *regional scale*, which includes the Canterbury Plains Breeze.

1.5 Mesoscale Numerical Modelling

Mesoscale atmospheric features as defined in section 1.3, have been studied with numerical models since the early 1970s (Pielke 1985). A numerical model can be defined simply as a computer algorithm that solves time-dependent partial differential equations that describe fluid or gaseous flow using mathematical numerical methods. Numerical methods are used since these equations are non-linear and an analytic solution for them is not known. An explanation of numerical methods used in mesoscale models is beyond the scope of this thesis, although Pielke (1984) provides a comprehensive background. Two broad categories of mesoscale numerical model exist, and these are prognostic and diagnostic models. A brief description of each is provided in the following sub-sections.

1.5.1 Prognostic Models

Prognostic models use the time-dependent partial differential equations to integrate forward in time, which effectively means that the model makes a forecast of the future state of the atmosphere (Pielke 1984). Depending on the chosen horizontal resolution, the forecast can be in minutes or seconds into the future. Currently, a number of prognostic models are available to study mesoscale features in the atmosphere, the most commonly used models include:

- Mesoscale Model (MM5) (Anthes and Warner 1978)
- Advance Regional Prediction System (ARPS) (Droegemeir *et al.* 1993)
- The Regional Atmospheric Modeling System (RAMS) (Pielke *et al.* 1992)

RAMS was the numerical model of choice for this thesis and a detailed description of some of its formulations and features is provided in Chapter 3.

1.5.2 Diagnostic Models

In diagnostic models, time dependency of the equations of fluid motion is either completely eliminated or the time derivative is used over one finite time step. Therefore this type of model does not provide a forecast for evolving mesoscale features of the atmosphere (Pielke 1985). A major drawback in using a diagnostic model is the requirement for extensive datasets, since at least part of the wind field must be known before a simulation can begin. Some examples of diagnostic models include those of Patnack *et al.* (1983), Dickerson (1978) and Danard (1977). The applicability of diagnostic models is limited since they cannot represent phenomena unless observations of them are available.

1.6 Prognostic Mesoscale Modelling in Complex Terrain

1.6.1 General Background

Recent advances in the design of high speed, large memory digital computers has prompted the formulation and use of more comprehensive numerical models to simulate atmospheric processes in complex terrain. Although mesoscale models have been used to investigate a whole range of mesoscale phenomena, a review of all reported cases is beyond the scope of this work. Pielke (1984) offered an extensive background to modelling papers published prior to 1984. The first reported mesoscale simulations were performed to study sea breeze circulations over flat terrain. McPherson (1970) was the first to perform three-dimensional calculations, followed by Pielke (1974), Warner *et al.* (1978), Mahrer and Pielke (1976, 1978), Hsu (1979), Carpenter (1979), and Kikuchi *et al.* (1981).

With the incorporation of a terrain-following coordinate system into the models, mesoscale modeling over complex terrain also became feasible. Slope and along-valley wind systems were simulated by Mahrer and Pielke (1977a, b) with an earlier version of RAMS. The Atmospheric Studies in Complex Terrain (ASCOT) dataset (Dickerson and Gudiksen 1980, 1981) provided valuable observational data for evaluation of mesoscale numerical codes. For example, Yamada (1981) performed a three-dimensional simulation of drainage winds in the ASCOT area in order to evaluate a new turbulence scheme which was incorporated into RAMS (2.5 order turbulent kinetic energy

scheme). Other examples of modelling simulations of along-valley winds include McNider (1981) and Mannouji (1982).

1.6.2 Numerical Studies of Regional Scale Circulation Systems

One of the earlier numerical studies of wind systems in complex terrain was conducted by Mannouji (1982). His simplified two-dimensional model runs showed that mountain winds can be separated into two components according to the scale of the underlying topography. One component is a circulation that is induced by heating/cooling of local relief which he termed slope flows, and the other component is a circulation that is induced by heating/cooling of the whole mountain massif which he termed plain-to-plateau flow. Later on, Bossert and Cotton (1994b) corroborated his findings on scale separation of flow systems with numerical experiments. Perhaps the most comprehensive numerical modelling papers on thermally induced regional scale circulations are those of Bossert and Cotton (1994a, 1994b). By performing a series of systematic idealized numerical experiments, they showed the importance of topographic configuration in generating regional scale circulations along the front range of the Rocky Mountains in the United States.

Using RAMS as a numerical tool, Bossert (1997) showed that similar circulations can also occur in Mexico Basin. He identified a regional scale plain-to-plateau wind system that seems to be a climatological feature in the region. Doran and Zhong (2000) also showed that regional scale horizontal temperature gradients can also be a forcing mechanism for the thermally driven gap winds observed in the southern part of Mexico Basin. Yet again, boundary layer evolution and regional scale circulations in Mexico Basin were the focus of an observational and numerical investigation by Whiteman *et al.* (2000). They were able to confirm Bossert's (1997) conclusion on the importance of regional scale flows in the Mexico Basin, but due to lack of suitable observational data could not provide additional information on the exact nature of this flow system.

Doran and Zhong (1994) recognized the importance of the development of a regional scale horizontal temperature gradient between the air over Columbia Basin and the Pacific Northwest Coast in forcing a circulation system which they termed the "regional drainage flow". Although regional scale thermally induced gap winds were not the focus of a study by Lu and Turco (1995), they were able to show that this wind

system can transport air pollutants originating in the Los Angeles area to the surrounding mountainous area.

Some investigators have specifically used numerical models to investigate characteristic features of plain-to-basin winds. Kimura and Kuwagata (1993) showed that plain-to-basin circulations are thermally induced, and that the flow can intrude into basins much earlier through mountain passes as no opposing upslope wind is present on the basin side. In this case, the plain-to-basin flow manifested itself as a thermally driven gap wind. As mentioned earlier, if no mountain gaps exist, the plain-to-basin circulation flows into the basin after the cessation of basin side upslope winds. De Wekker *et al.* (1998) presented results from 60 idealized two-dimensional numerical simulations with various basin geometries. Their results showed that the key physical mechanism for the formation of plain-to-basin circulation is the existence of a horizontal temperature gradient above mountain ridge height.

In New Zealand, the importance of scale interaction in determining local weather in Canterbury was demonstrated numerically by McKendry *et al.* (1986). Although they recognized the importance of regional scale (100 – 500 km) influences on the development of the Canterbury northeasterly, only dynamic causes of lee trough formation were considered. It will be shown in Chapter 4 that regional scale thermal influences can also lead to northeasterly winds over the Canterbury Plains.

1.7 Thesis Objectives

A numerical modelling component is usually a highly desirable part of any meteorological study. Sophisticated models which describe complex non-linear atmospheric processes have become an invaluable tool in many branches of meteorology, including the study of thermally forced circulation systems in complex terrain (Fast 1995). By controlling some parameters (i.e. the initial and boundary conditions) in model simulations, relationships between atmospheric forcing and feedback mechanisms can be determined on time and space scales not possible in even the most comprehensive observational programme. When properly integrated, numerical modelling and observational studies can be used to complement one another to yield information not available from either. To achieve this goal, one must give

careful consideration to the types of phenomena to be simulated and thereafter select a numerical model which is capable of performing the desired simulation.

There are two philosophies used in the design of a numerical modelling programme:

1. to simulate the characteristics of observed phenomena on a case by case basis with the goal of reproducing specific sets of observations. The advantage here is the ability to verify the model results with actual observational data, thereby verifying the physical formulations in the model and helping to interpret the observations.
2. to design a modelling programme with the goal of reproducing the idealized structures that are representative of actual observational cases to determine the dominant forcing and feedback mechanisms leading to the observed flow phenomena.

The complex topography of the experimental site in MacKenzie Basin and the fact that detailed data on many forcing factors (i.e. soil moisture, vertical temperature structure outside the basin) are not available makes application of the first philosophy less practical for this investigation. For these reasons, the second method is more appropriate.

Therefore, the objectives of this thesis are to use an atmospheric mesoscale model to determine:

- What types of thermally driven circulation systems can develop in the vicinity of MacKenzie Basin?
- If the CPB is an intrusion of the sea breeze that forms along the Canterbury coast.
- What are the characteristics of this circulation system and what are the causal mechanisms?
- How variations in ground wetness affect the characteristics of the CPB through its effect on boundary layer growth.

The approach used in achieving these objectives involves performing a series of idealized two- and three- dimensional numerical experiments and relating the results to field observations.

1.8 Thesis Format

Chapter 2 presents observational data showing the existence of a recurring circulation system named the Canterbury Plains Breeze in MacKenzie Basin. It is seen that this wind system is a common feature of the basin's wind regime during settled weather. Atmospheric sounding data gathered with the use of a light instrumented aircraft and surface observations from a network of weather stations were analyzed for two case study days when thermally induced wind systems were observed.

Chapter 3 offers a more detailed description of the Regional Atmospheric Modeling System (RAMS), and reviews some of the model formulations.

Chapter 4 presents results from coarse resolution three-dimensional model runs, where the role of synoptic scale influences and the sea breeze in generating the CPB is evaluated.

Chapter 5 investigates the physical mechanisms responsible for the development of the CPB by performing systematic two-dimensional numerical model runs.

Chapter 6 is devoted to analysis of results from two high resolution model runs. In this chapter, the interaction between locally generated thermal circulations and the CPB is investigated.

Chapter 7 revisits the initial objectives of the thesis and provides a summary of key findings.

Chapter 2

Observations of Thermally Induced Flows in MacKenzie Basin

2.1 Introduction

In this chapter, results from observational data gathered in January/February 1999 during a field campaign conducted in MacKenzie Basin are presented. The primary aim of the research programme –called the **L**ake **T**ekapo **Ex**periment (LTEX) is to gain a better understanding of atmospheric boundary layer processes and local wind regimes in complex terrain (Sturman *et al.* 2000). Participating scientists were interested in studying a wide variety of meteorological phenomena, ranging from channelling of the pre-frontal foehn wind (locally referred to as *nor'wester*) to the nocturnal development of near surface temperature inversions and local winds close to sloping terrain. Several different types of meteorological data were collected, although the principal dataset used in this thesis is from a network of Automatic Weather Stations (AWS) providing a description of the surface wind field in the basin. In addition, pilot balloons and an instrumented light aircraft were used to complement surface data and provide information on the vertical structure of meteorological variables.

During undisturbed weather, this observational evidence will demonstrate the presence of a recurrent circulation system which influences the wind regime in MacKenzie Basin from early in the afternoon, advecting relatively cold coastal air into the basin.

2.2 Description of the Experimental Site

MacKenzie Basin is the largest enclosed inland basin in the South Island. A picture of the island taken from NASA's Skylab highlights the fact that the Canterbury Plains and MacKenzie Basin are the two most extensive flat regions in the area (Figure 2.1).

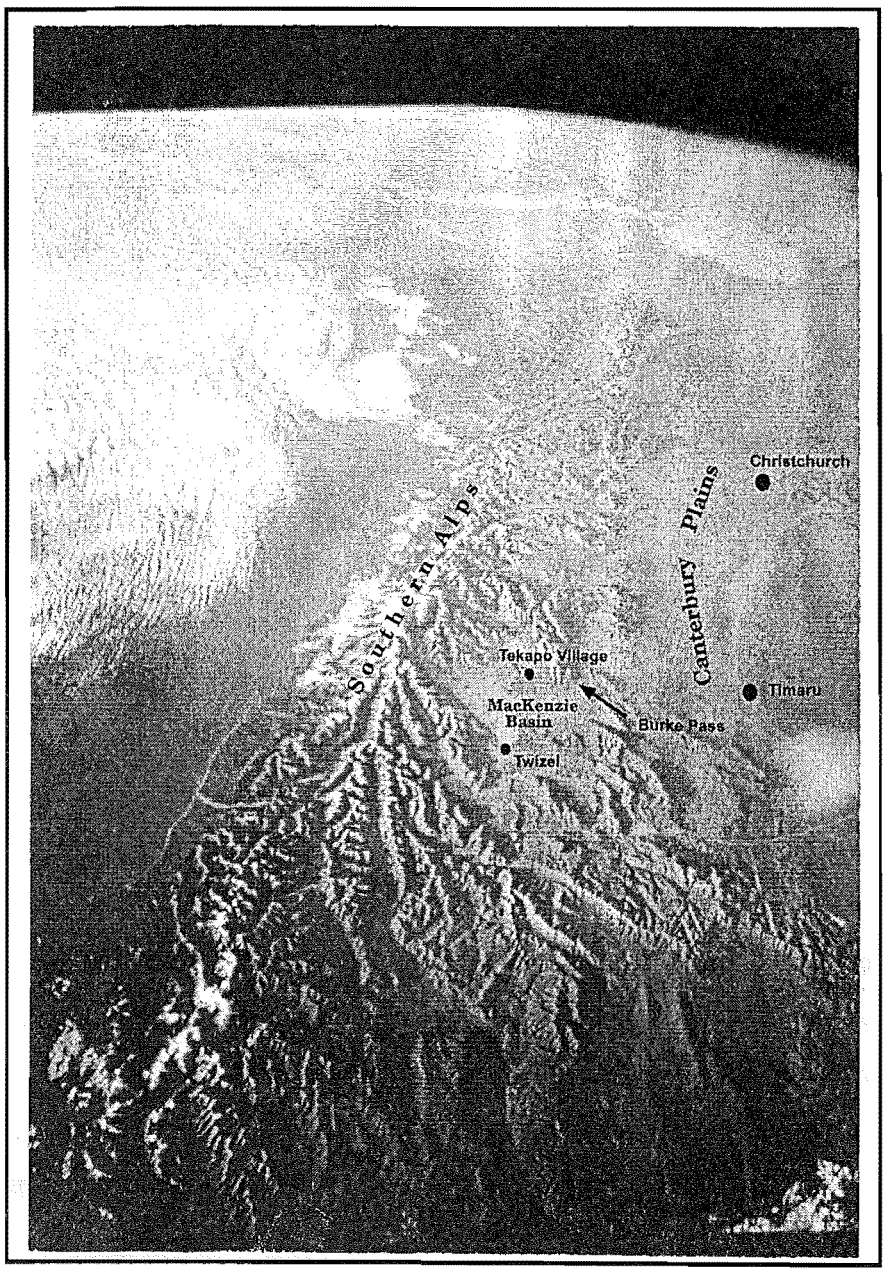

Figure 2.1: Photograph of the South Island taken from Skylab showing the Canterbury Plains and the MacKenzie Basin as two extensive flat areas in the region.

The basin is situated approximately 180 kilometers southwest of Christchurch, and lies in the rainshadow of the Southern Alps. It spans an area of approximately 1500 square kilometers, with an average elevation of 600m.

Three major lakes of glacial origin are situated in the basin, Lake Tekapo (the experimental site) is at the northeastern corner of the basin immediately west of the Two-Thumb Range, while lakes Pukaki and Ohau are situated on the western half of the basin flanking the Ben Ohau Range (Figure 2.2). The local vegetation in the basin consists mainly of tussock grassland. The climate of the basin is typical of the inner montane basins of the South Island, where rain shadow effects and the absence of a moderating maritime influence on the climate are dominant. Average annual rainfall is only 600mm per year, with the number of sunshine hours in excess of 2200. Average daily temperature has a range of 11.6 degrees (Garr and Fitzharris, 1991). Figure 2.3 shows a more detailed map of the Lake Tekapo region where data gathering efforts were concentrated.

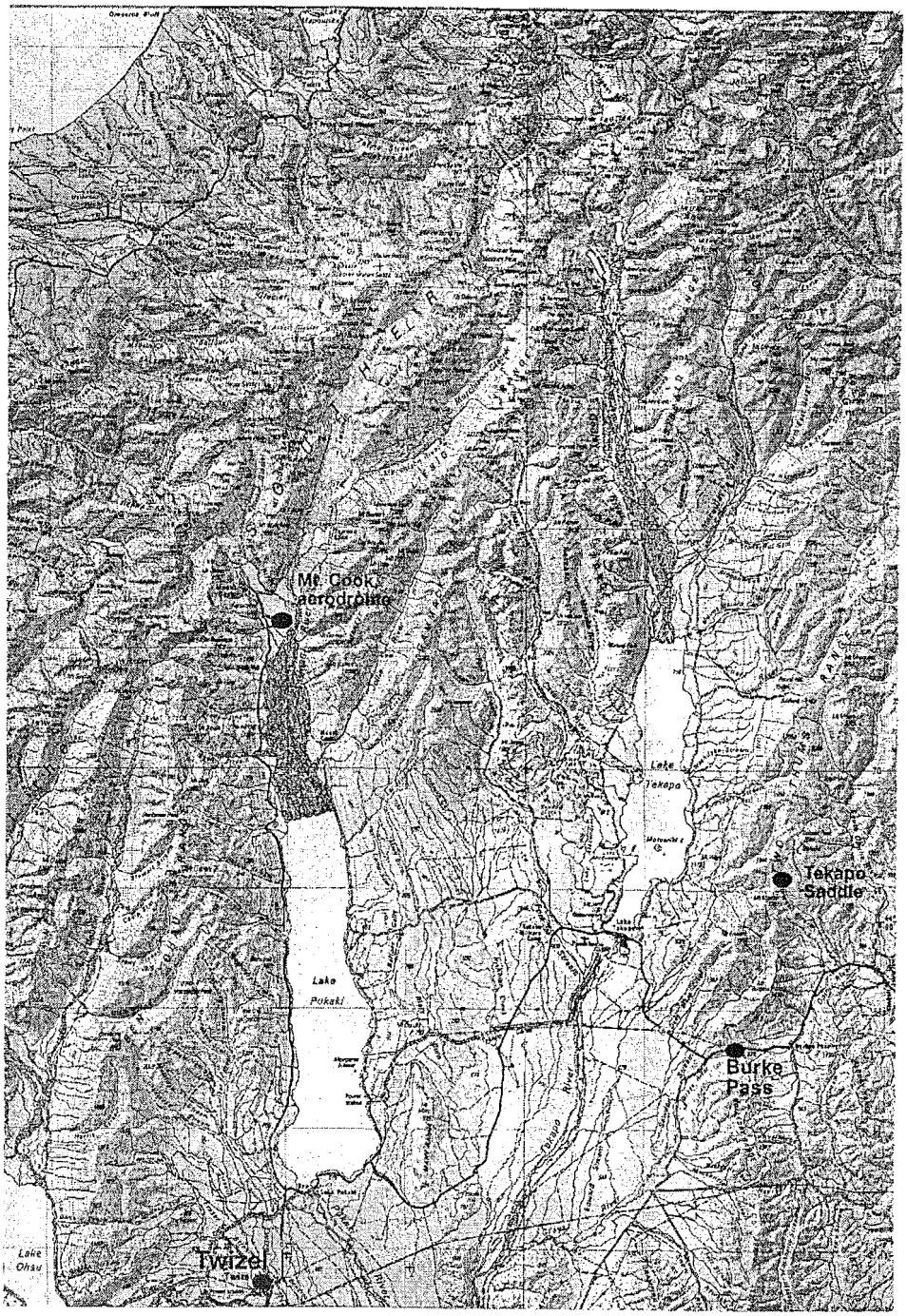

Figure 2.2: Map of MacKenzie Basin.

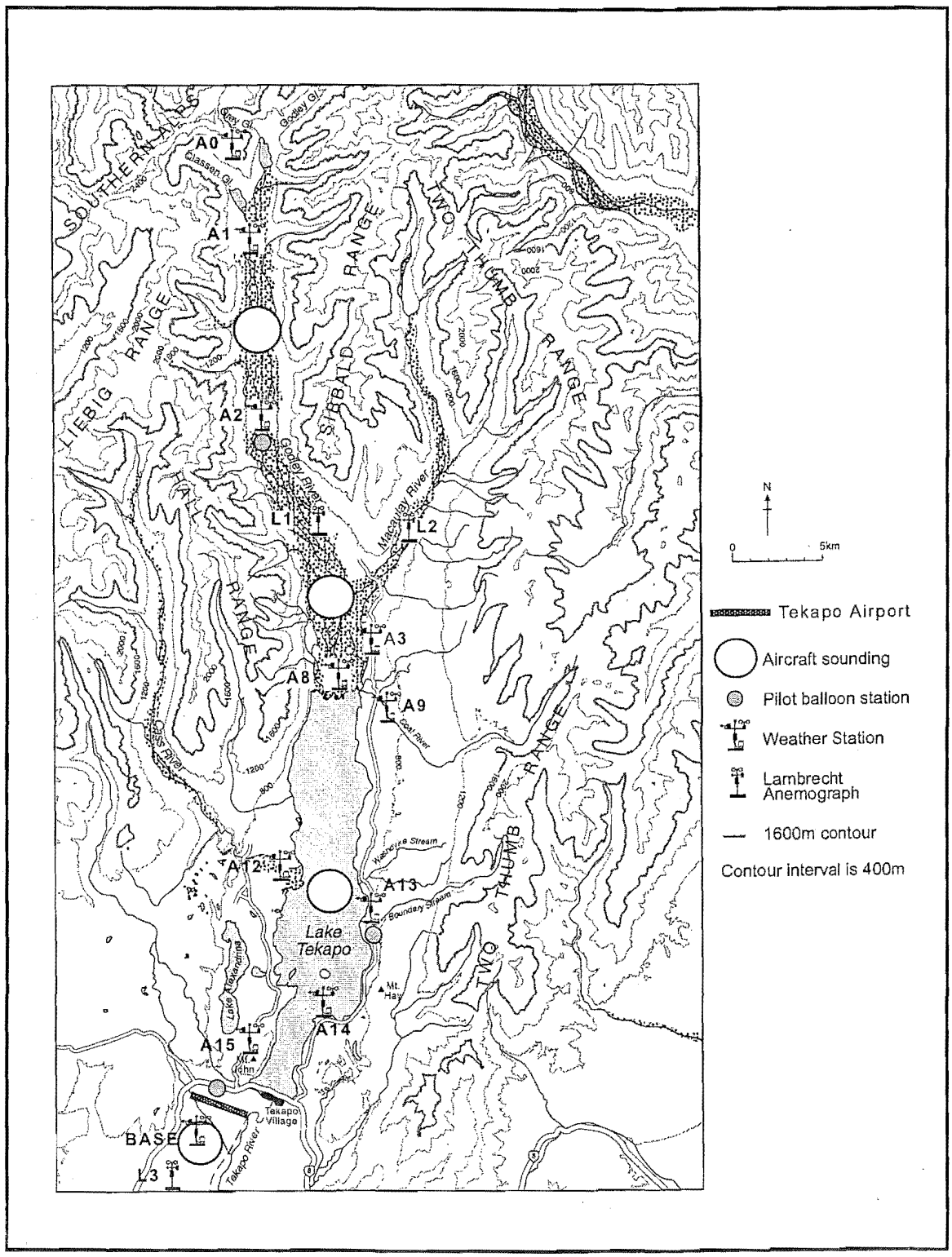

Figure 2.3: Map of Lake Tekapo area showing the location of measuring stations.

2.3 Previous Meteorological Research in the Area

The Southern Alps of New Zealand have a strong influence on the climatology of the region. As such, the Alps have recently been the venue for a major collaborative

meteorological study. The Southern Alps Experiment (SALPEX) was undertaken in three phases from 1993 to 1996. The major aims of the project were in gaining knowledge for improvement of extreme weather forecasts and understanding the role of mountains on cloud and precipitation development (Wratt and Sinclair 1996; Wratt *et al.* 1996). Special data gathering periods occurred when strong northwesterly synoptic flow was prevalent. Therefore, the SALPEX dataset falls into a dynamic forcing framework and could not be used as a supplementary source of information for this thesis. Another study in the area was that of Revell *et al.* (1996) who were interested in simulating wind gusts measured at Mt. Cook aerodrome during the passage of a front (Figure 2.2). RAMS was also their numerical tool of choice, and they showed that the gusts are generated in a turbulent wake associated with flow separation at ridge crests.

McGowan and Sturman (1996) and McGowan, *et al.* (1995) provided relevant background on thermally induced winds observed around Lake Tekapo. These investigations were undertaken to understand the thermal and dynamic physical processes responsible for the initiation of dust storms in the region. In the following section, their findings are discussed in more detail as background to the LTEX dataset.

2.4 Previous Observations of the Canterbury Plains Breeze

Prior investigations of the wind regime in the vicinity of Lake Tekapo identified the occurrence of locally generated thermal circulations due to spatial variations in the landscape. Diurnally reversing, lake/land breezes and valley/mountain circulations were observed to dominate the surface flow field when synoptic pressure gradients were weak. Although the importance of scale in generating a hierarchy of thermal circulations was acknowledged by the investigators, regional scale thermally induced influences on the wind regime were not considered. Observed airflow intruding through Burke Pass and Tekapo Saddle was interpreted as a strong sea breeze, but not as a plain-to-plateau or plain-to-basin circulation. Therefore, the existence of the Canterbury Plain Breeze was not considered, and its meteorological signal was associated with other phenomena.

McGowan and Sturman (1996) concluded that when synoptic pressure gradients are weak, thermally induced circulations are generated in Lake Tekapo Basin during summer and spring. A local scale lake breeze was often observed to interact with the valley wind system during daytime. They also presented results of analysis from a 30

year record of wind data from an anemograph located on Mt. John located near the southwest corner of Lake Tekapo (Figure 2.3). An interesting feature observed in this record is small frequency peaks of airflow from between 50° and 90° from 1400 to 2100 NZST in both spring and summer. They associated this airflow with the channelling of the Canterbury coast northeasterly through Tekapo Saddle. Although onset and cessation time of this feature suggests an underlying thermal forcing, it was initially interpreted as a sea breeze rather than topographically generated.

Results from a case study day (6th November 1992) were presented by McGowan *et. al.* (1995) to illustrate thermodynamic characteristics and temporal variations of the lake breeze circulation. Synoptic conditions on this day were conducive for generating thermally forced wind systems. Vertical profiles of wind speed and direction were obtained on an hourly basis from a site north of Lake Tekapo. A peculiar feature of the vertical wind structure is the detection of a 1500 m deep southerly current of moderate intensity (5 ms^{-1}) at 1800 NZST (their Figure 9). Although the thermal origin of this current was recognized, it was believed to be a combined lake breeze-valley wind airflow. However the time of onset, depth and the intensity of the flow suggest that other explanations are possible. An alternate explanation for the phenomena reported by McGowan *et. al.* (1995) and McGowan and Sturman (1996) is that during quiescent synoptic conditions, a wind system that is induced by the horizontal temperature gradient between the atmosphere inside and outside the basin is observed in the afternoon during spring and summer months. The investigation of this hypothesis is one of the major objectives of this thesis.

2.5 The Lake Tekapo Experiment (LTEX)

The LTEX research programme lasted for three years, during which two one month field campaigns, one in November/December 1997 and another in January/February 1999 were conducted (Sturman *et al.* 2000). An El Niño event dominated the first campaign which resulted in a very high incidence of strong westerly foehn winds. Consequently, days that were suitable for the development of thermally induced winds were rare. In contrast, the 1999 campaign was carried out during a La Niña event, resulting in a higher frequency of undisturbed anticyclonic weather. When settled anticyclonic synoptic weather systems dominated the region, special observation periods (SOPs) were conducted to collect a more intensive dataset. During the SOPs,

radiosondes, pilot balloons and an instrumented light aircraft collected vertical profiles of temperature, relative humidity and wind speed and direction at several sites.

As the primary focus of this thesis is numerical modelling, an exhaustive explanation of data collection techniques is avoided. A brief description of the monitoring network is provided below.

2.5.1 Surface Meteorological Monitoring Network

The surface monitoring network of LTEX was not designed to capture the meteorological signal of the regional scale wind system. Complex topography and remoteness of the region presented logistical challenges, and the monitoring network design reflected a greater interest in investigating local scale phenomena in the vicinity of Lake Tekapo. In addition, the importance of the CPB for the wind climatology of the region was not recognized following the first field campaign in 1997, since persistent northwesterly foehn winds dominated the period.

Table 2.1 provides a summary of the surface weather stations, and Figure 2.3 provides information on their location. In the naming convention used to label the stations, the letter A indicates an automatic weather station and L indicates a Lambrecht anemometer site. Some stations were only mounted temporarily and did not provide a continuous dataset, and other stations were operated over an extended period. Supplementary surface data were also obtained from weather stations at Twizel operated by Landcare Research (Figure 2.2), and at Panorama Ridge in the upper Godley Valley operated by the Electrical Corporation of New Zealand (station A0, Figure 2.3).

Table 2.1: Summary of surface monitoring network. Height of the sensor is indicated in the parenthesis. Definition for symbols are as follows: ambient air temperature (Ta), relative humidity (RH), wind direction (dir), wind speed (U), shortwave radiation (K↓), soil temperature (Ts), skin surface temperature (T_{SURF}), and pressure (P).

Name	Parameters	Observation frequency
A1	Ta,RH (0.2, 2.4m) U, dir (2.5), K↓, Ts(0.1m)	Long term (1 hr) SOP (10 mins)
A2	Ta,RH (0.2, 2m),U,dir (2.1m),P	SOP (10 mins)
A3	Ta,RH(1.6m),U,dir(3.2m),P	SOP (5 mins)
A7	Ta,RH(1.6m),U,dir(3.2m),P	SOP (5 mins)
A8	Ta, RH, U (1.03, 3.9, 9.05m), U (6.09m), dir (9.05m), Ts (0.1m),P	Long term (1 hr) SOP (10 mins)
A12	Ta (0.6, 3.13m), RH (3.13m), U,dir (3.4m) Ts (0.1m), K↓	Long term (1 hr) SOP (10 mins)
A13	Ta,RH (3.12m), U, dir (3.37m),Ts (0.1m),P	Long term (1 hr) SOP (10 mins)
A14	Ta, RH (1.4m) U, dir (1.55m)	SOP (15 mins)
A15	Ta, RH (3.14m), U,dir (3.34m), Ts (0.1m)	Long term (1 hr) SOP (10 mins)
BASE	Ta,RH (3.2m), U,dir (10m),Ts (0.1m), P,K↓,$T_{surf.}$	Long term (1 hr) SOP (10 mins)
L1	U,dir (2.4m)	SOP (Continuous)
L2	U,dir (2.4m)	SOP (Continuous)
L3	U,dir (2.4m)	SOP (Continuous)

2.5.2 Boundary Layer Observation Techniques

a) Pilot Ballooning

The pilot balloon technique provided the ability to obtain vertical profiles of wind speed and direction up to an altitude of 2000 meters above the ground when conditions were favorable. Three pilot balloon stations were setup during the special observational periods (Figure 2.3), and as only three theodolites were available, the double theodolite method which gives more precision was not employed. When a single theodolite is used to track the released balloons, several assumptions have to be made which could lead to errors in calculation of wind speed and height as summarized by Rider and Armendariz (1970). The first assumption neglects the effects of vertical air motion, and presumes that the balloon has a constant ascent rate. The ascent rate is derived from measurements of the balloon's weight and lift when filled with hydrogen. It can be seen that the assumption of zero vertical wind speed could lead to gross errors

in mountainous terrain during strong winds when considerable vertical velocities might be generated. Another factor that may lead to errors in calculation of wind speed and height is variation of air density with altitude. Note that these errors become larger with increasing height, so that near surface winds are more reliable.

b) Aircraft Data

An instrumented light aircraft (Piper-181) obtained vertical profiles of pressure, temperature and relative humidity for the SOP on February 2nd and 12th. The aircraft proved to be a very economical way of gathering data in remote areas. On February 12th , the aircraft managed to complete four flights (each being one and half hours in duration), obtaining a total of 16 vertical profiles at four sites (Figure 2.3).

2.5.3 Wind Regime in the Basin During LTEX 99

The complex topography of the experimental site gives rise to a hierarchy of topographically induced, multi-scale wind systems, making analysis of surface data a challenging task. In the following sub-sections, it will be shown that the Canterbury Plains Breeze is a persistent feature of the wind climatology of MacKenzie Basin. Although its exact nature cannot be determined due to both paucity of data outside the basin and the complicated topography inside, numerical experiments in the following chapters will provide some insight to its origin and its three dimensional characteristics. The limited amount of data collected in the field allows evaluation of model results in the basin.

Previous studies paid much attention to investigating the surface wind regime around Lake Tekapo. In this section, a close examination of daytime surface flow at Base and Twizel weather stations for the duration of the field campaign in 1999 is made (Figures 2.2, 2.3).

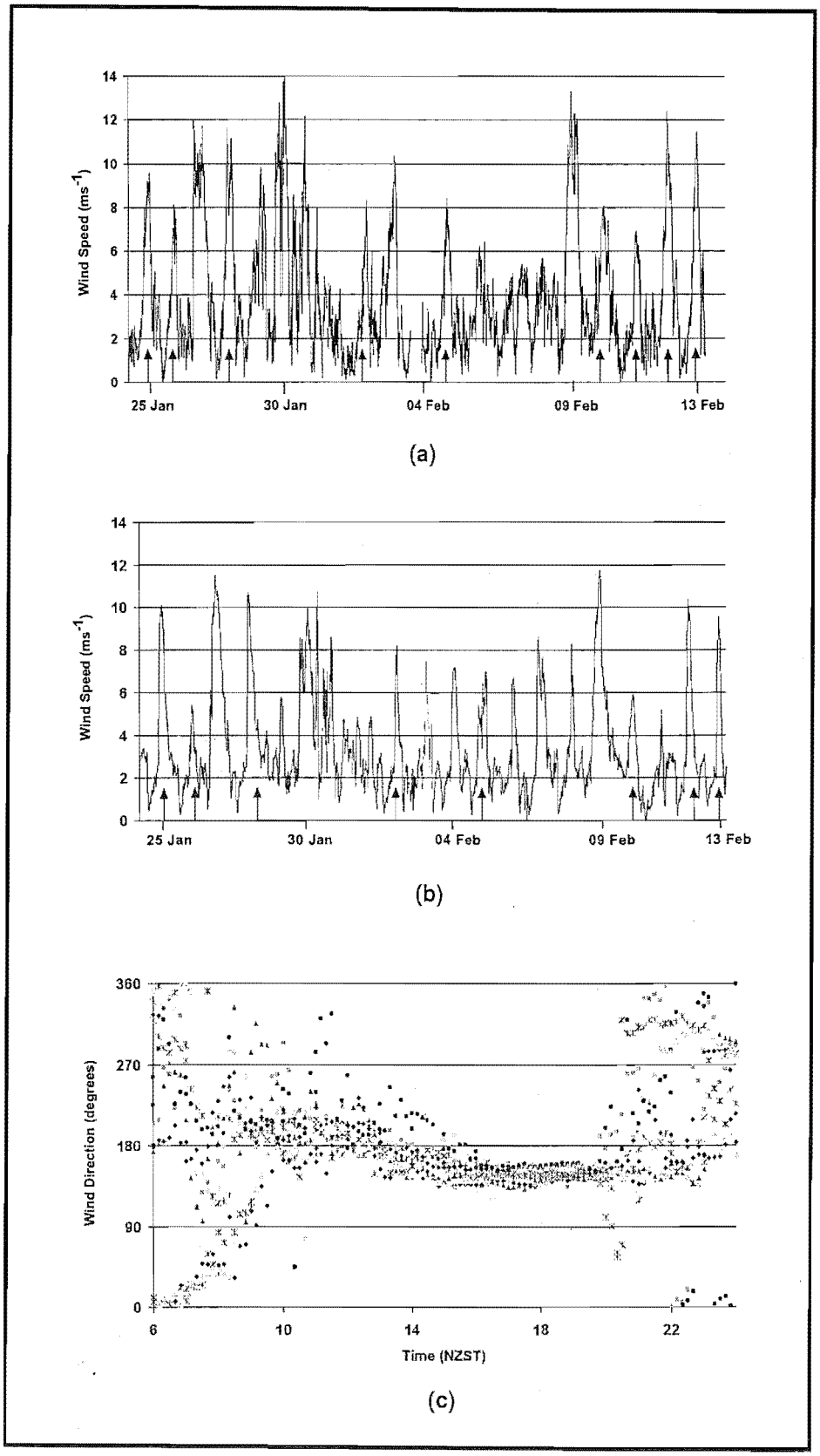

Figure 2.4: **Time series of (a) ten minute averages of wind speed for Base site, and (b) 30 minute averages of wind speed for Twizel, and (c) scatterplot of ten minute averages of wind direction for the Base site on the days when CPB intrusion into the basin took place (arrows indicate the days when the CPB was detected by the surface station).**

Figures 2.4a, b present time series of wind speed for Base and Twizel stations, respectively. The measurements are considered to be representative of the conditions in MacKenzie Basin, since both surface stations are situated in relatively uncomplicated physical settings (i.e. not situated in valleys). Of particular interest, is the periodic appearance of strong winds in MacKenzie Basin, which can also occur with the grounding of synoptic airflow associated with prefrontal foehn west to northwesterly winds (McGowan *et al.*1995). The arrows on Figure 2.4a indicate days that were ideal for the development of thermally induced flows. On these days:

a) weak synoptic pressure gradients existed over the region

b) the basin was mostly cloud free for a significant portion of the day, as determined from measurements of short-wave radiation at Base station

c) surface wind speeds before 1200 NZST were less than 6 ms^{-1} (higher wind speeds would suggest an existing synoptic scale influence).

At the Base weather station, strong southeasterly winds were measured on all nine days, with an onset time of around 1400 NZST. Figure 2.4c shows a scatterplot of 10- minute-average wind direction data against time of day from the Base site for these nine days, indicating that the strong winds only occurred from a narrow range of directions. The strong airflow was usually well established by 1500 NZST, and on most days it ceased shortly after sunset. A strong easterly wind also occurred at Twizel on each day except for 11th February (Figure 2.4b). On this day, the easterly intrusion only reached an intensity of 6 ms^{-1} at the Base site. Therefore it seems that generally, the Canterbury Plains Breeze is strong enough to dominate the surface flow throughout the basin when it is blowing. The base station is located 8 km from Burke Pass and the limited range in wind direction might indicate that the CPB is channelled by the pass, although no weather stations were situated in or close to the pass to confirm this hypothesis. What is evident is that the strong easterlies are a basin wide phenomenon, and the physical scale of the forcing does not seem to be local in nature. Figure 2.5 shows that for the 12th February case study day, the easterly current reached the Base station first and about an hour later arrived at the Twizel site. Assuming that the density current's propagation speed is roughly equal to wind speed perpendicular to micro-front, with an average wind speed of 8 ms^{-1} air can travel about 28 km suggesting that the observed strong winds at Twizel are part of the same circulation observed at Base.

Therefore, the observations at these two stations reveal the existence of a recurrent flow phenomenon across the basin. In its most basic form, this flow manifests itself as a high-speed easterly with early to late afternoon onset period, and on most days it ceases at these two sites shortly after sunset.

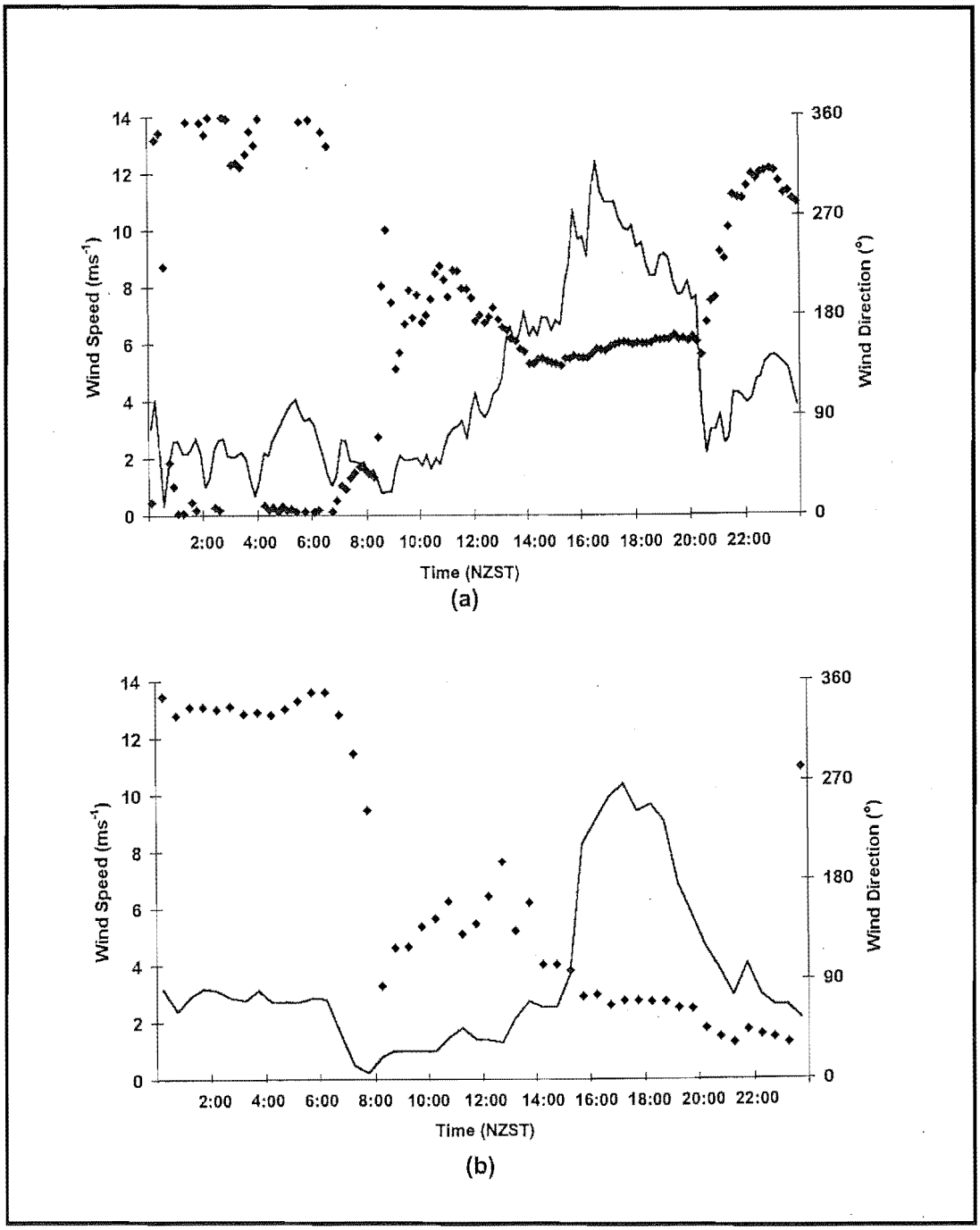

Figure 2.5: (a) Time series of ten minute averages of wind speed and direction for the Base site on 12th February, (b) time series of 30 minute averages of wind speed and direction for the Twizel station on 12th February (solid line represents wind speed, and diamonds represent wind direction).

2.5.4 Case Study Days: 2nd and 12th February 1999

In this section, a closer examination of the evolving wind field and boundary layer development in the experimental area for the SOPs held on 2nd and 12th February 1999 is provided. On 2nd February, data collection efforts were concentrated at the northern end of Lake Tekapo to gather information on nocturnal katabatic flows, consequently pilot ballooning data are not available throughout the day. However, the aircraft obtained three vertical profiles before noon and one profile in the evening over the Base site. On 12th February, observational efforts concentrated on the study of daytime thermally induced circulations along the lake and in Godley Valley, so that the instrumented aircraft flew four times during the day, in addition, regular pilot balloon data are available from the ballooning stations.

a) Synoptic Weather Conditions

As indicated previously, thermally induced flows are best observed during clear, undisturbed weather, and such a condition existed on both 2nd and 12th February. The slow moving centre of a high-pressure system was situated over the South Island on the 2nd (Figure 2.6a). The anticyclone was not deep, and analysis at 500mb indicates a moderate southwesterly airflow aloft (Figure 2.6b). The 1200 NZST surface analysis on 12th February also indicates anticyclonic synoptic scale circulation over New Zealand (Figure 2.7a), although the high-pressure system was deeper on this day as indicated by 500mb analysis (Figure 2.7b). Therefore, the analysis of synoptic data indicates that although surface pressure gradients were weak on both case study days, on the 2nd February pressure gradients aloft were stronger.

Due to the passage of a cold front on 31st January, the atmosphere inside the basin was about 5 K colder on the 2nd compared to 12th February (Figure 2.8). Interestingly enough, similarity in the difference between the first and the last profiles obtained by the aircraft over the Base site indicates that the basin atmosphere was heated by similar amounts on both days.

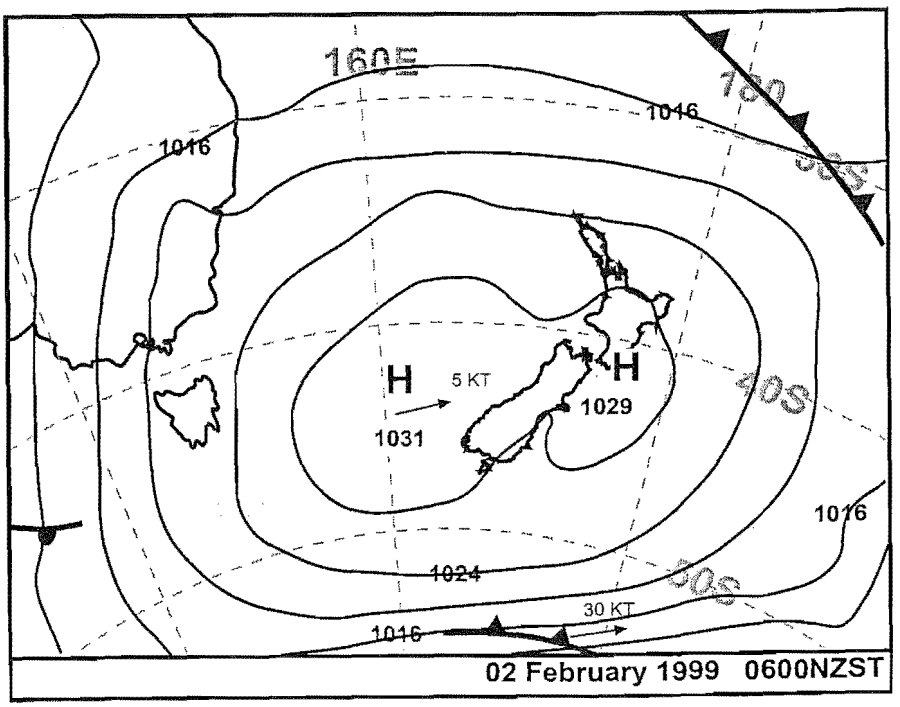

(a)

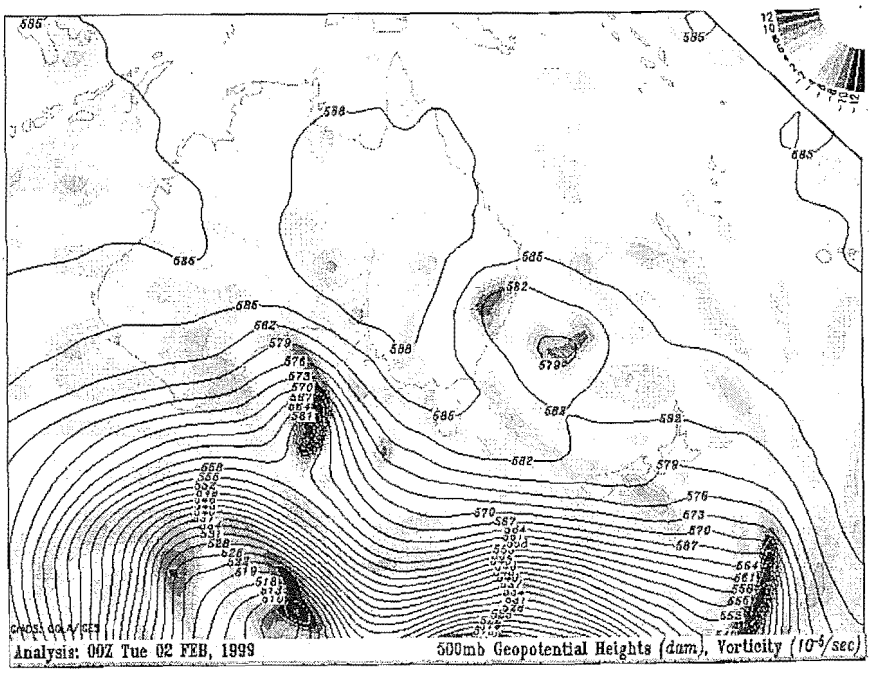

(b)

Figure 2.6: Analysis for (a) 0600 NZST on 2nd February 1999 at surface by New Zealand Meteorological office, (b) 1200 NZST on 2nd February 1999 at 500mb by Institute of Global Environment and Society.

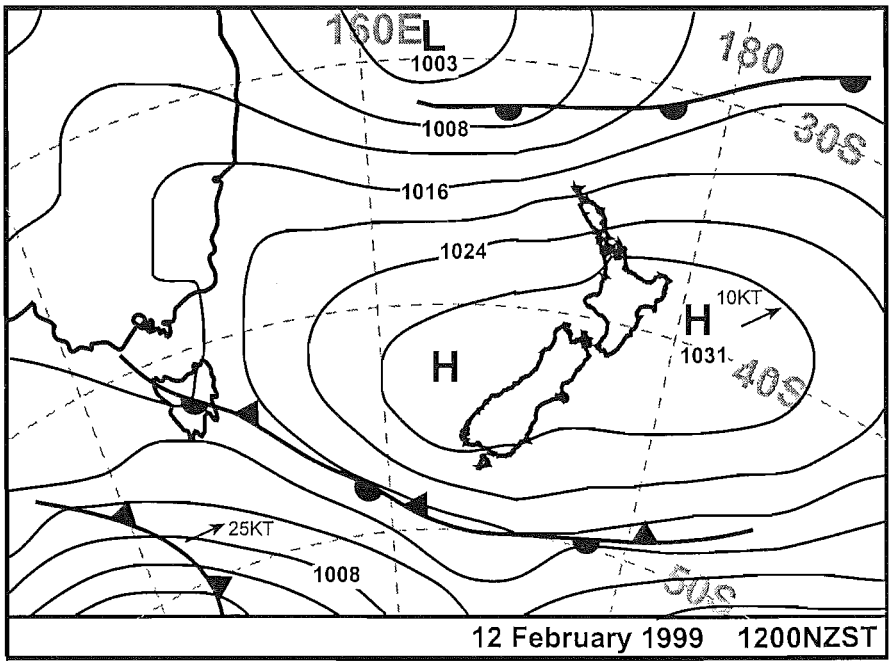

(a)

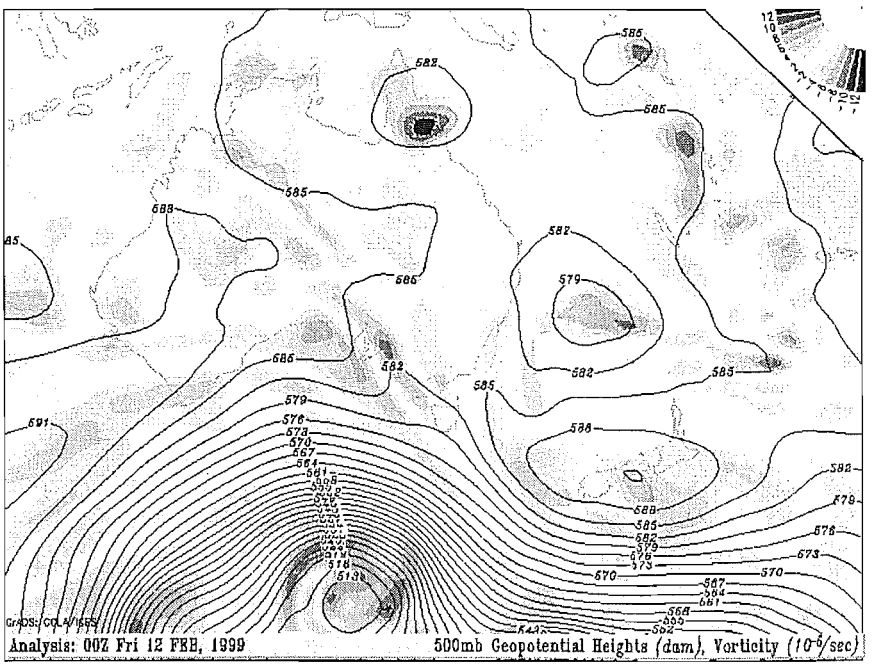

(b)

Figure 2.7: Analysis for (a) 1200 NZST on 12th February 1999 at surface by New Zealand Meteorological office, (b) 1200th NZST on 12 February 1999 at 500mb by Institute of Global Environment and Society.

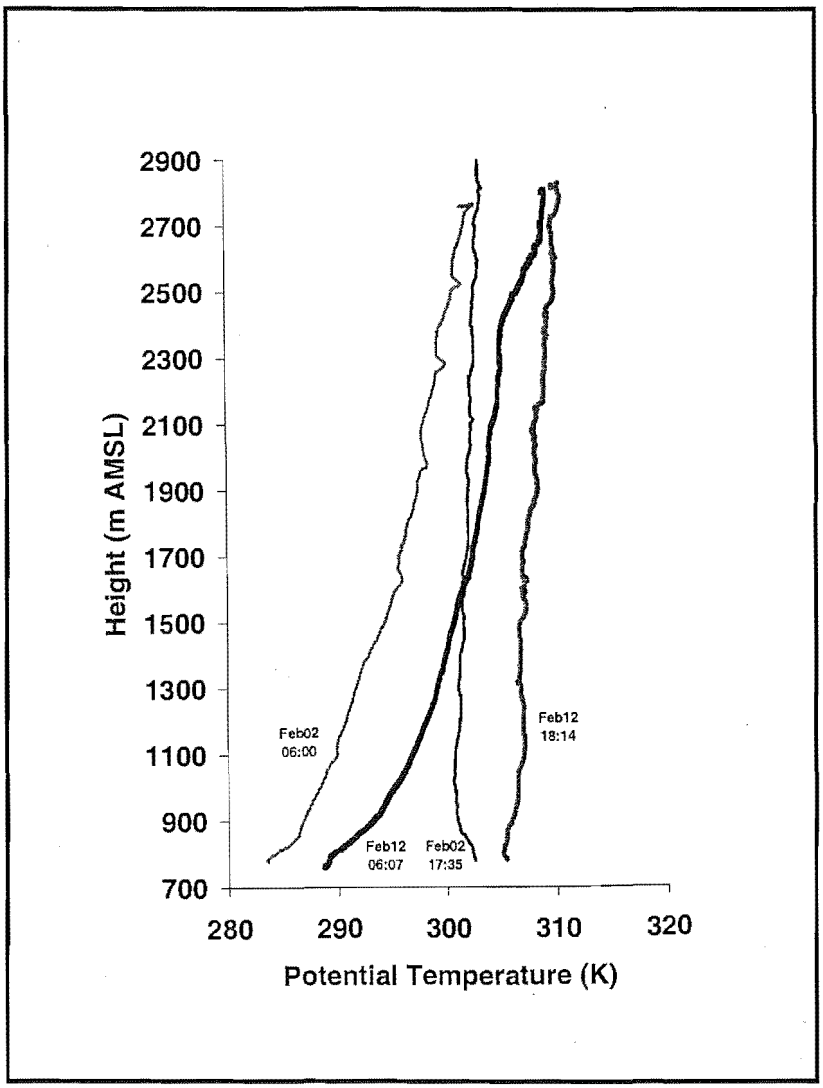

Figure 2.8: Vertical profiles of potential temperature measured by the aircraft over the Base site on 2nd and 12th February.

b) Surface Observations

To gain insight into evolution of surface flow in the MacKenzie Basin and Lake Tekapo region, a series of surface airflow maps were constructed. Surface airflow maps using all available wind data at 1200, 1400, 1600, 1800 and 2000 NZST on 2nd February are presented in Figure 2.9. By 1200 NZST, heating of the land surface around the lake seems to have generated a lake breeze circulation resulting in a divergent flow (Figure 2.9a).

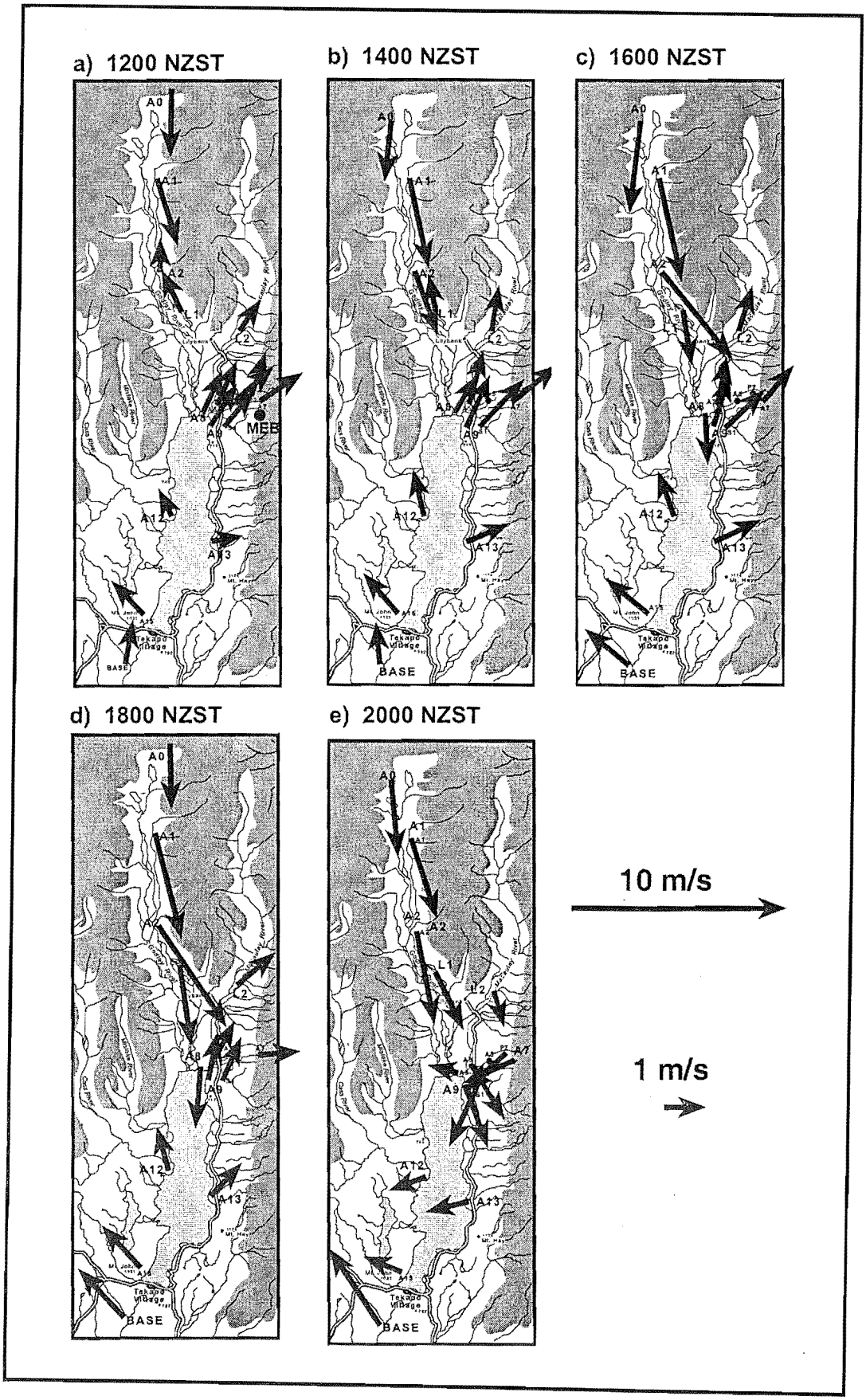

Figure 2.9: Surface flow field on the 2nd February over Lake Tekapo region at (a) 1200 NZST, (b) 1400 NZST, (c) 1600 NZST, (d) 1800 NZST , and (e) 2000 NZST. Wind speed and direction are ten minute averaged values.

During this SOP, a dense network of monitoring stations was placed at the northeast corner of the lake, all the stations indicate a southwesterly flow which is probably a combined upslope-lake breeze circulation. The two most northern stations in Godley Valley detected a moderate northerly wind which seemed to converge with a weak southerly valley wind circulation in Godley Valley. Two hours later at 1400 NZST, the northerly current seems to have propagated further south (Figure 2.9b), and the following diagrams show its progression southward, probably reaching the northern end of Lake Tekapo by 1600 NZST, as detected by station A8 (Figure 2.9c). When the current left Godley Valley, it seemed to flow to the west of the valley circulation causing a horizontal wind shear that is maintained for about two hours between 1600 to 1800 NZST (Figures 2.9c, d). The northerly flow is probably generated by pressure driven channeling (Whiteman and Doran 1993) related to the pressure gradient at higher levels (Figure 2.6b), and/or foehn winds over the main divide (McGowan and Sturman 1996). By 1600 NZST, therefore, the surface airflow pattern in the study area was made more complicated by three main features (Figure 2.9c). These were a southeasterly flow at the Base site caused by the intrusion of the CPB, the locally forced diverging flow over the lake, and the northerly current established over Godley River delta. The northerly current weakened, and was retreating northward by 2000 NZST (Figure 2.9e), probably in response to cessation of surface heating and decoupling of surface flow from airflow aloft. However, the CPB was still evident at the Base site and moderate cold air drainage initiated over Lake Tekapo. Time series of specific humidity and temperature data obtained by a mobile energy balance station located over the eastern slopes (indicated by MEB on Figure 2.9a) suggest that the downslope wind was advecting moist air down the slope, indicating a coastal origin for the airmass (Figure 2.10). The easterlies detected by stations A12 and A13, and the downslope winds on the Two Thumb Range are likely to be part of the plain-to-basin circulation.

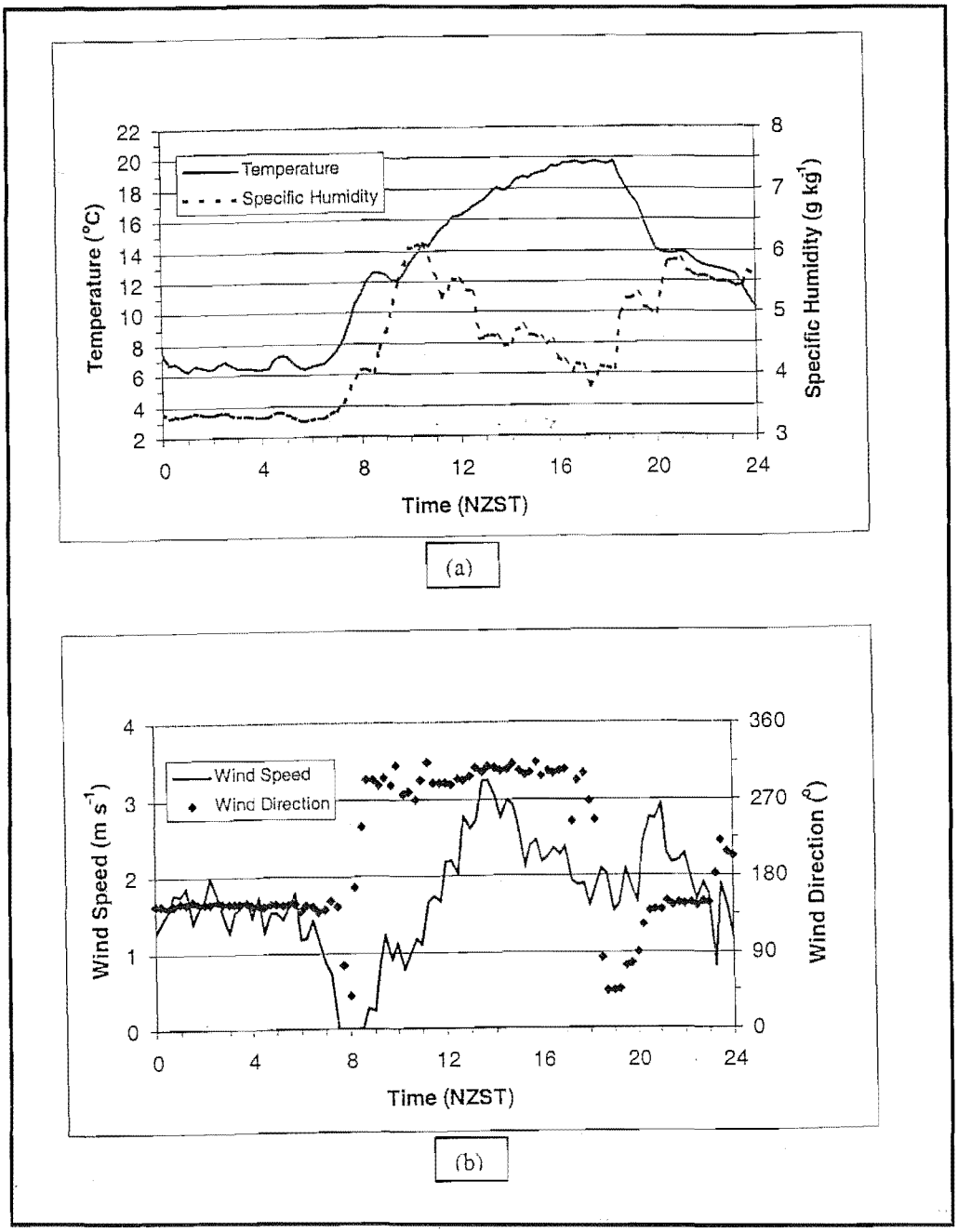

Figure 2.10: Time series of (a) temperature and specific humidity, and (b) wind speed and direction, measured by a mobile energy balance station over the western slopes of the Two Thumb Range (values are 15 minute averages).

The surface wind field on 12th February evolved differently. At 1000 NZST (Figure 2.11a), the stations in Godley Valley detected weak easterlies, these cross-valley winds are probably in response to surface heating of the eastern slopes of the valley leading to cross-valley temperature gradients. Because of the weak upper level winds, the strong northerly current that was observed on the 2nd February was not present. A weak lake breeze circulation had developed around lake Tekapo, which seemed to intensify by 1300 NZST (Figure 2.11b). Up-valley winds were established in

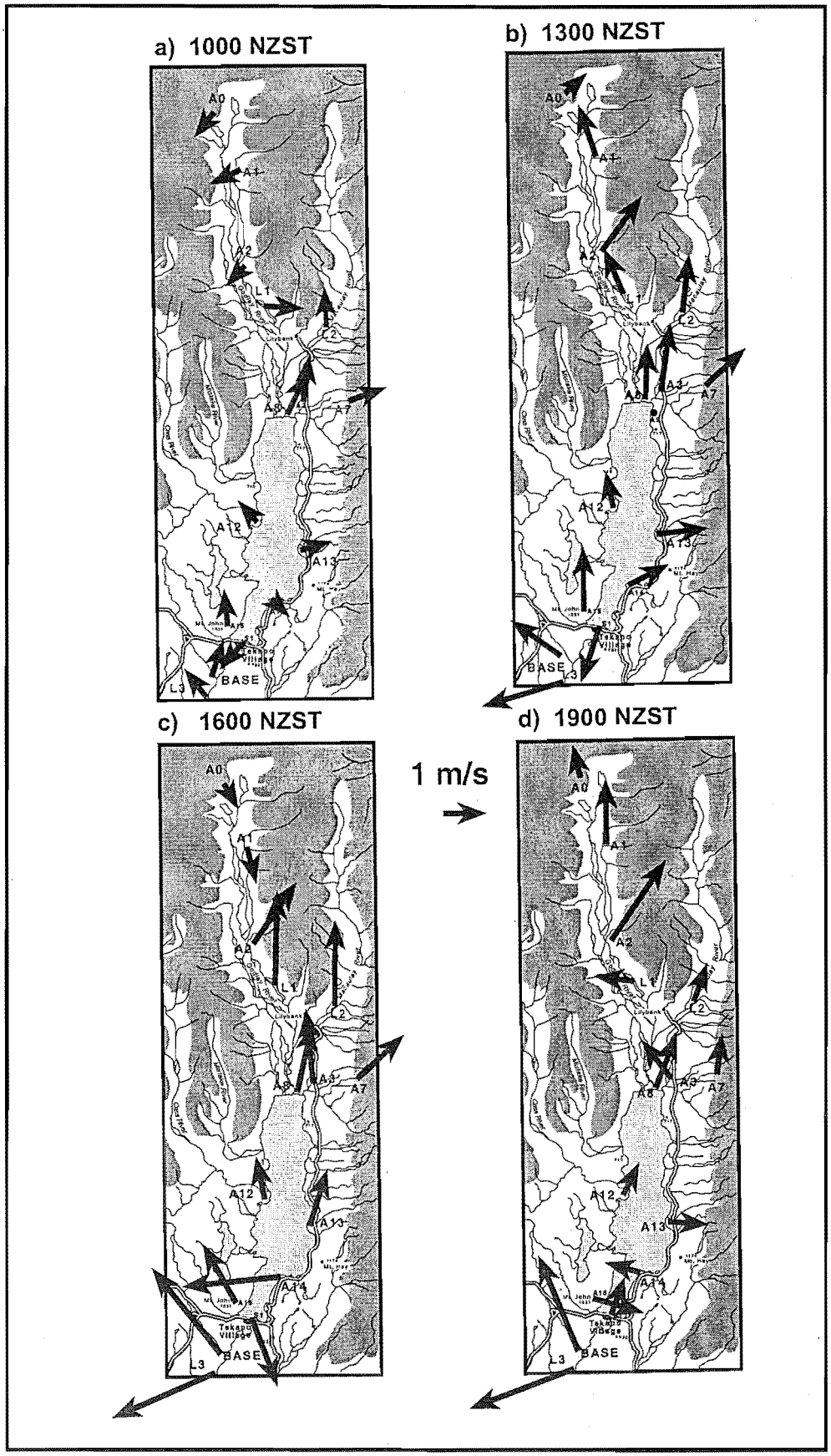

Figure 2.11: Surface flow field on the 12th February over Lake Tekapo region at (a) 1000 NZST, (b) 1300 NZST, (c) 1600 NZST, and (d) 1900 NZST. Wind speed and direction are ten minute averaged values.

Godley and Macaulay Valleys, and the Canterbury Plains Breeze was now detected at the Base and L3 stations. At 1600 NZST, the plain-to-basin wind was also flowing through Tekapo Saddle (Figure 2.1), as detected by station A14, and some parts of the flow are diverted southward by Mt. John (which has an elevation of 1031 m AMSL) as measured by the station in Tekapo Village (Figure 2.11c). A component of this northerly might be the local lake breeze sheltered by the moraine south of the village. The moderate intensity of the up-valley wind at the north end of the lake suggests that the easterly intrusion was channelled towards the two river valleys, in addition, pibal data indicate that a strong southerly current 200 m in depth was blowing at this time over the Boundary stream station (Figure 2.13c). By 1900 NZST, the locally induced thermal flows had weakened, but the CPB had maintained its intensity, and interestingly, a strong current evident at A1 and A2 stations seemed to be propagating northwards in Godley Valley (Figure 2.11d).

Figure 2.12 presents time series of temperature, wind speed and direction for the case study days for the Base weather station. The onset of the CPB at this site occurred at about 1400 NZST on 12th February and at around 1600 NZST on the 2nd (as indicated by the arrows). The arrival of the current was associated with decreasing air temperature, indicating that the CPB was advecting cold air into the basin (Figure 2.12c).

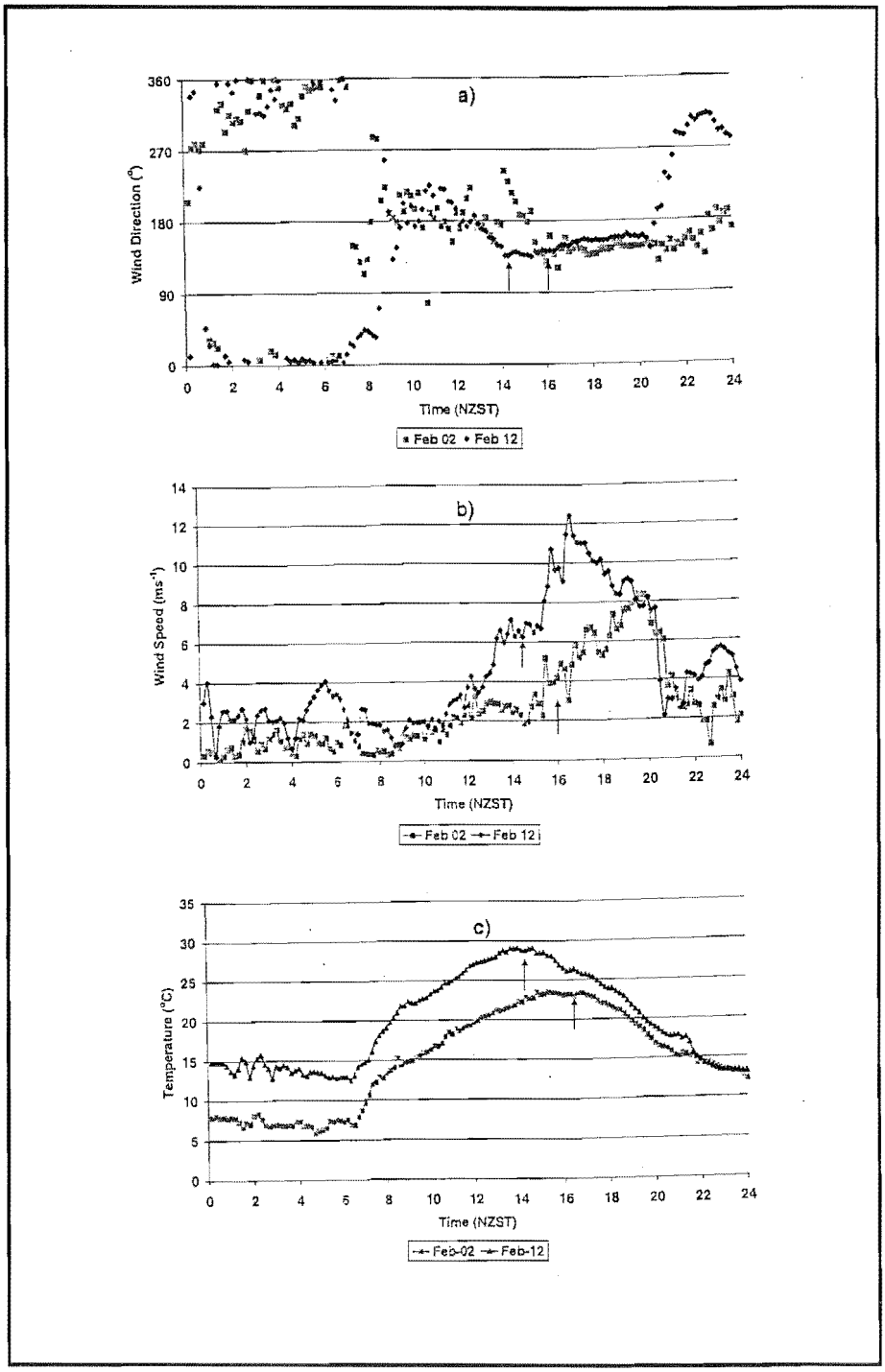

Figure 2.12: Time series of (a) wind direction, (b) wind speed, and (c) temperature measured at the Base site on 2nd and 12th February. Values are ten minute averages and the arrows indicate the onset of the CPB.

c) Boundary Layer Development

In order to observe the effects of the plain-to-basin circulation on atmospheric boundary layer structure in the basin, regular vertical profiles before and after the

intrusion are required. Additionally, to quantitatively determine the nature of the forcing using observational data it would have been desirable to have had vertical profiles available at a site outside MacKenzie Basin over the Canterbury Plains. As explained before, as the importance of such a circulation system for the wind regime of the basin had not been recognized, the opportunity to collect an appropriate dataset was missed. Since 12th February was chosen as a case study simulation day for the numerical experiments, and the early morning vertical profile of thermodynamic variables from the aircraft was used to initialize high resolution model runs in Chapter 6, the observed boundary layer behaviour is described below.

Figure 2.13 presents contour plots of the u and v components of wind derived from the data obtained by the three pilot ballooning stations (see figure 2.3). A strong 600 m deep southeasterly flow was detected by the station at Tekapo airport (Figures 2.13a, b). The head of the current passed this location at about 1400 NZST in agreement with measurements at Base weather station located 4 km to the south, and continued to flow until 1800 NZST. Strong southerly currents also developed at Boundary (A13) and Godley (A2) stations (Figures 2.13c, e), while surface wind maps suggest that this current originated from Tekapo Saddle and then was deflected northwards (Figure 2.10c). This southerly current had a depth of 300 m and hence, was not as deep as the one detected at the airport. The current arrived at Boundary site at 1500 NZST, and continued to flow until 1800 NZST. A 500 m deep southerly up-valley wind was measured in Godley Valley from 1100 to 1500 NZST, and then a strong southerly current with a depth of 600 m passed the pilot balloon station at 1600 NZST (Figure 2.13e). The current maintained its intensity by the time the measurements were stopped at 2000 NZST.

Figure 2.14 shows the temporal evolution of vertical profiles of potential temperature measured by the aircraft above Base and mid-lake locations. A parabolic shaped temperature inversion existed in the morning over the basin, whereas the temperature structure over the lake was more layered. By 0935 NZST, turbulent sensible heat flux had caused the formation of a 300 m mixed layer over the basin, and the profile over the lake still showed the existence of the temperature inversion. The air below 2100 m seemed to have warmed due to advective heating. The third profile over each location shows the presence of a 1500m mixed layer, although the mixed layer over the lake was probably advected from the basin by the southerly valley wind. There is a four and half hour gap between the third and the fourth profiles, hence no vertical temperature profiles exist close to the time when the CPB was detected at the Base

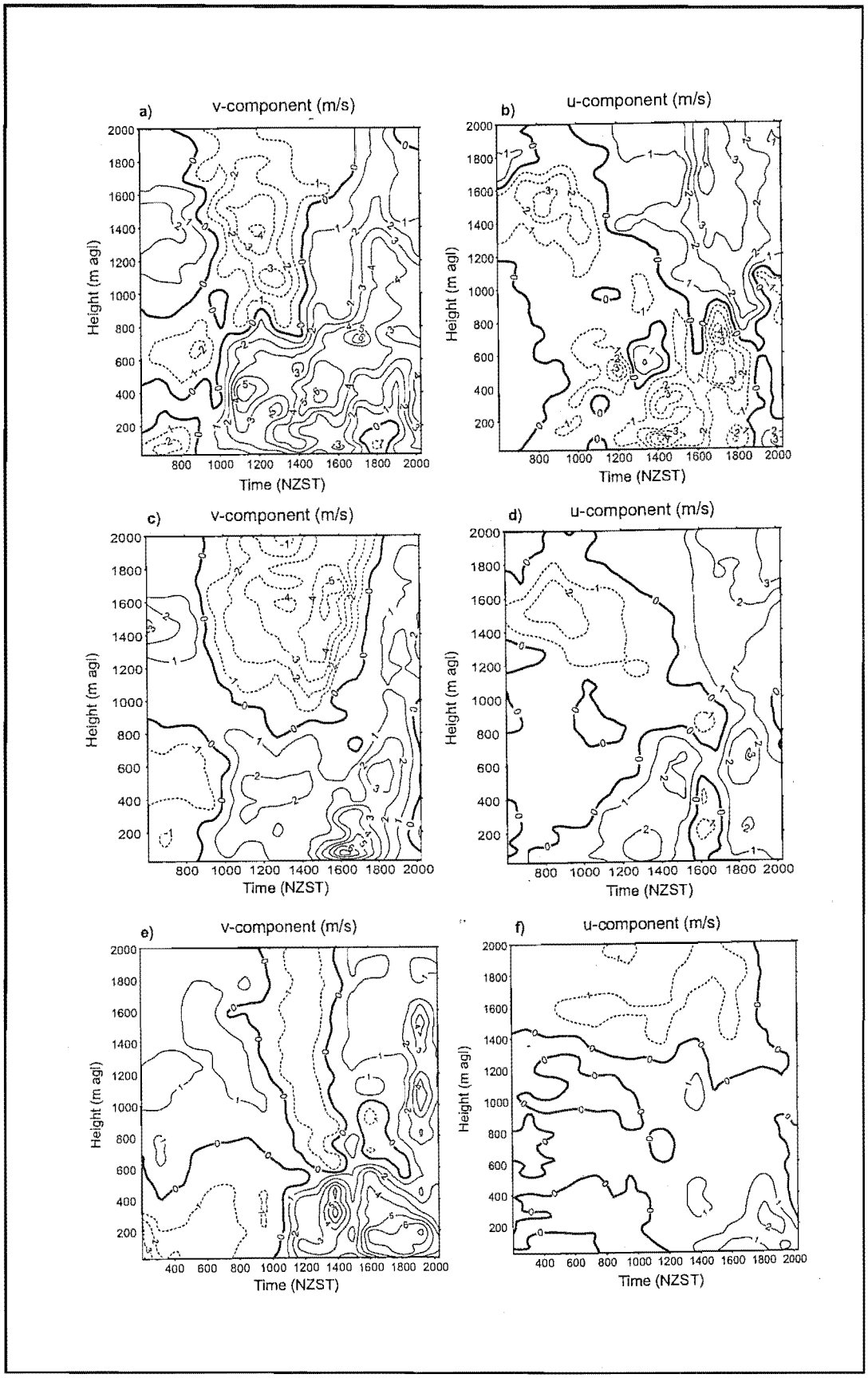

Figure 2.13: Contour plots of *u*- and *v*-components of wind velocity for the (a, b) airport, (c, d) Boundary Stream, and (e, f) Godley Valley pilot balloon stations on 12th February.

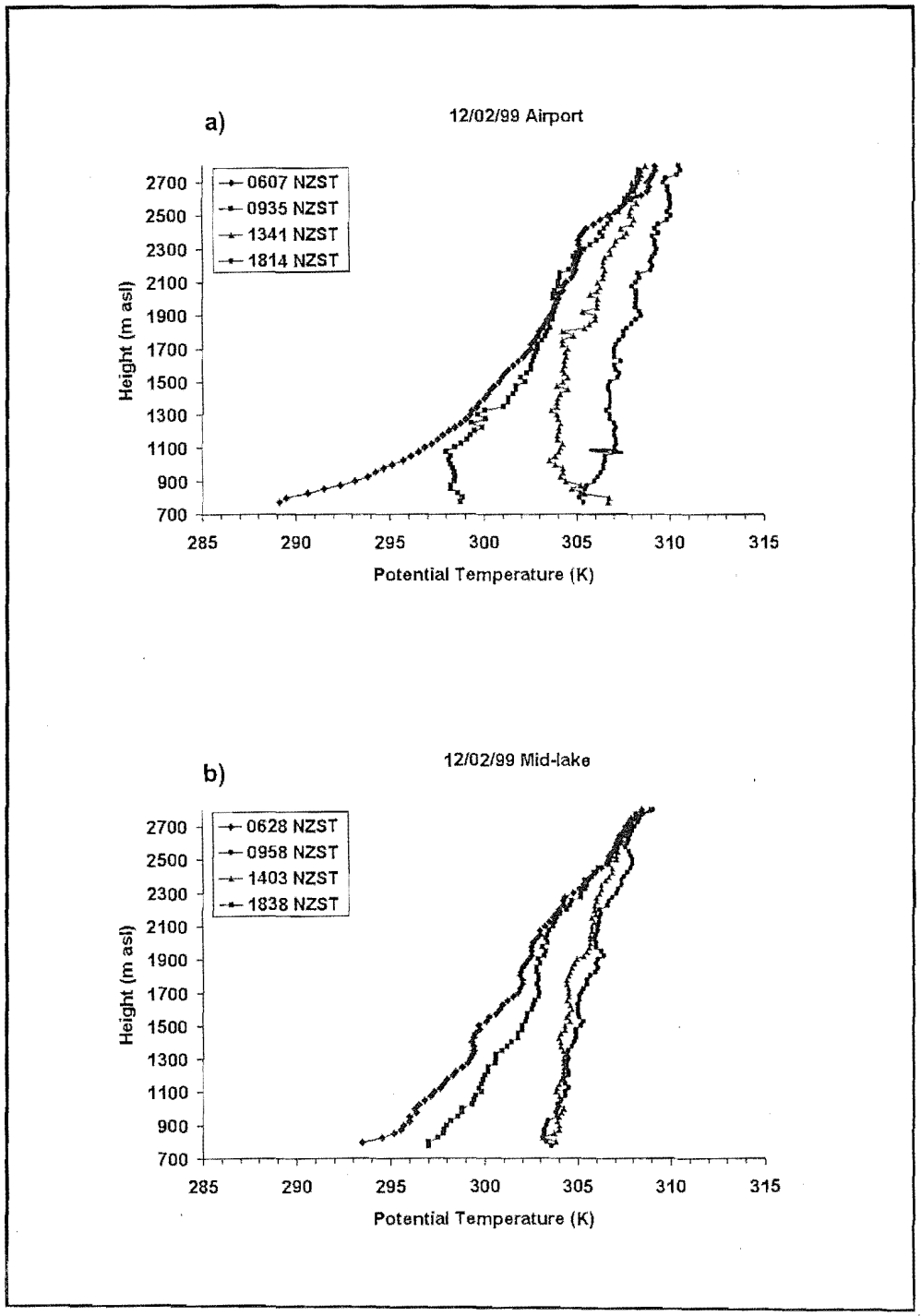

Figure 2.14: Vertical profiles of potential temperature measured by the aircraft over the (a) airport and (b) mid-lake area on 12th February.

surface station. But the fourth profile in the basin suggests that a 300 m layer had been affected by cold air advection. There is no significant difference between the third and the fourth profiles over the lake.

2.6 Summary and Conclusion

Although the monitoring network for LTEX was not ideal for a comprehensive study of a regional scale wind system such as the Canterbury Plain Breeze, available surface data in the basin reveal interesting characteristics of this circulation. On spring and summer days when undisturbed weather dominates the region, the CPB will flow into the basin either through mountain passes and saddles, and/or flow down the slopes as observed on 2nd February. The breeze has the intensity to dominate surface flow throughout the basin, and is associated with cold air advection. Therefore, the Canterbury Plain Breeze is a recurring circulation system during settled weather conditions. Since the air current seems to originate from outside MacKenzie Basin, its horizontal forcing falls into the regional scale category.

Chapter 3

Model Description

The Regional Atmospheric Modeling System (RAMS) was developed at the Colorado State University, where it was formed as a result of merging three different numerical codes (Pielke 1992). The code is almost entirely written in Fortran 77, with the exception of a few subroutines written in C which deal with dynamic memory allocation. RAMS, in its current form is a flexible, general purpose numerical code, capable of simulating a variety of atmospheric flows. It has been used to study flows at several scales, ranging from flow over buildings to hemispheric circulations. The model contains a full set of subgrid, microphysical, radiative, convective and surface-layer parameterizations. Prognostic models for soil and vegetation temperature and moisture are also included. The model's other capability is a telescoping two-way interactive grid nesting, so that it is possible for a single simulation to represent forcings from a multitude of scales.

The model runs are usually configured in a namelist file called RAMSIN. Various peripheral data preparation codes are also provided for formatting input data into RAMS. A description of procedures for setting up a model run is not provided here since it is beyond the scope of this chapter. The version of RAMS used in this thesis is designated as 3a, and this particular code has been tested by scientists at the Pacific Northwest National Laboratories in Richland, Washington State since 1995 (Fast *et al.* 1996; Zhong *et al.* 1996; De Wekker *et al.* 1998; Whiteman *et al.* 2000; Doran and Zhong 2000). The code has been thoroughly tested, and the known bugs have been

fixed. Simulations were carried out on a dual processor (300 MHz each) Ultra-Enterprise Sun Microsystem computer, running the Solaris 2.6 Unix operating system. At compilation time the executable was optimized to level 5 (O5) for maximum efficiency. The real clock-time for the simulations in Chapter 4 was approximately five days, the two-dimensional runs in Chapter 5 took seven hours of computation, and the high resolution runs in Chapter 6 took nearly three weeks to complete.

3.1 Background

The fact that the atmosphere is a hydro-thermodynamic system has been realized for the past 200 years. This realization meant that atmospheric motions could be quantified (analyzed by equations) with the familiar Newtonian mechanics and the laws of thermodynamics (Holton 1979). Subsequently in the 19th century, a basic set of equations governing the movement of air in the atmosphere known as the "primitive equations" was developed. The term *primitive* in no way indicates that the equations are outmoded, rather it highlights their fundamental nature (Wallace and Hobbs 1977). The primitive equations are equations of momentum, continuity, thermodynamics and moisture (Atkinson 1981; Brown 1991). The equations for momentum are sometimes referred to as the Navier-Stokes equations since Navier and Stokes independently derived them. However, the title is also used to include the continuity equation and the thermodynamic equation, therefore nowadays the terms primitive equations and Navier-Stokes equations are used interchangeably. The primitive equations are highly complex and non-linear which makes them impossible to solve by current available analytic techniques. Hence, analytic solutions for them are unknown, except when the equation set is simplified and linearized. Although the simplified forms of the equations give valuable insight into certain types of atmospheric phenomena, their general applicability is limited since non-linear influences are ignored. With the development of high-speed digital computers it has become possible to make extensive use of the primitive equations in their non-linear form using numerical techniques, since these techniques require vast amounts of mathematical calculations. Indeed John von Neuman, one of the pioneers of the development of high-speed digital computers, was the first to recognize that computers could help in forecasting weather (Wallace and Hobbs, 1977).

3.2 Averaging the Primitive Equations

As previously mentioned, because of their non-linearity, analytic solutions for the primitive equations are not available (this is true for almost all physical problems), therefore numerical techniques are used to provide approximate solutions to the equations. Tannehill *et al.* (1997) provided one of the most highly regarded books on numerical methods for fluid mechanics and heat transfer, which provides an exhaustive description of various numerical methods, including the ones used in RAMS.

Holton (1979) provides an in-depth derivation of the *primitive* equations, while Pielke (1984) offers derivation and assumptions used to provide a suitable equation set describing mesoscale flow. In the ensuing section, the set of equations which are solved by RAMS are presented in their volume averaged form, with an explanation for averaging provided next.

The primitive equations contain partial differential operators ($\partial/\partial t$, $\partial/\partial x$, $\partial/\partial y$, $\partial/\partial z$) which in the strictest mathematical sense are only valid in the limit when δt, δx, δy, and δz approach zero (time increment and the three spatial intervals respectively). Physically, this means that in order to solve the equations exactly with numerical techniques the solution has to be computed at molecular level, which is for now and the foreseeable future impossible. To bypass this problem, the conservation equations have to be integrated over specified spatial and temporal scales determined by the available computer capacity and its speed of operation. Therefore, an averaging decomposition (also known as Reynold's decomposition) is performed on the conservation equations:

$$\phi = \overline{\phi} + \phi' \qquad \textbf{(3-1)}$$

where ϕ represents any one of the dependent variables, and $\overline{\phi}$ is the average of ϕ over the finite time increment Δt and space intervals Δx, Δy, and Δz (Figure 3.1). The variable ϕ' is known as the *subgrid scale perturbation* which is the deviation of ϕ from the average, it is this quantity that has to be parameterized in models. $\overline{\phi}$ is formally defined as:

$$\overline{\phi} = \int_{t}^{t+\Delta t} \int_{x}^{x+\Delta x} \int_{y}^{y+\Delta y} \int_{z}^{z+\Delta z} \phi \, dz \, dy \, dx \, dt \; / \; (\Delta t)\,(\Delta x)\,(\Delta y)\,(\Delta z) \qquad \textbf{(3-2)}$$

In numerical models, Δt is known as the time step and Δx, Δy, and Δz are the grid intervals. This averaging operator is applied to the conservation equations, and details of this mathematical procedure are offered by Pielke (1984), while the final form of the equations are presented in the next section.

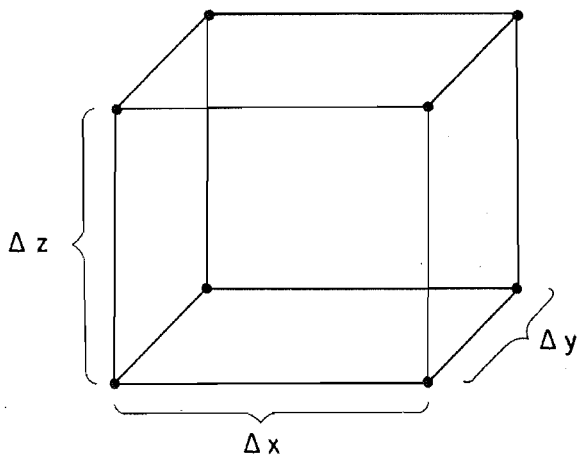

Figure 3.1: Representation of a grid volume. Dependent variables are defined at the corners of the rectangular grid.

3.3 A Brief Technical Description of RAMS

Only a brief technical description of the model is provided in this section. All model integrations for this work use the non-hydrostatic dynamic framework. This framework should be included when the scale of resolved features in the model have aspect ratios near unity, or when the horizontal scale is shorter than the vertical scale. The additional term in the non-hydrostatic dynamics is vertical acceleration that contributes to variations in the vertical pressure gradient, so that the hydrostatic balance is no longer maintained exactly. The general equations for RAMS are described in the following section (overbars indicating averaged quantities are omitted).

3.3.1 General Equations Solved by RAMS

Equations of motion

The horizontal equations of motion are:

$$\frac{\partial u}{\partial t} = -u\frac{\partial u}{\partial x} - v\frac{\partial u}{\partial y} - w\frac{\partial u}{\partial z} - \theta\frac{\partial \pi'}{\partial x} + fv + \frac{\partial(u'u')}{\partial x} + \frac{\partial(u'v')}{\partial y} + \frac{\partial(u'w')}{\partial z} \qquad \textbf{(3-3)}$$

$$\frac{\partial v}{\partial t} = -u\frac{\partial v}{\partial x} - v\frac{\partial v}{\partial y} - w\frac{\partial v}{\partial z} - \theta\frac{\partial \pi'}{\partial y} - fu + \frac{\partial(v'u')}{\partial x} + \frac{\partial(v'v')}{\partial y} + \frac{\partial(v'w')}{\partial z} \qquad \textbf{(3-4)}$$

I **II** **III** **IV** **V**

Term I represents wind acceleration

Term II represents advection

Term III represents the pressure gradient force

Term IV represents coriolis force

Term V represents turbulent diffusion

where u and v are the horizontal velocity components and w is the vertical component. π' is the perturbation Exner function, which arises in these equations as a result of replacing pressure with the total Exner function (π) in the equations before Reynold's averaging is performed on them. In mesoscale models, the pressure gradient term is expressed with the Exner function rather than pressure. The advantages of using the Exner function are that the term involving density perturbation (ρ') is removed from the equation set, and since the vertical gradient of π is much less than pressure, fewer numerical errors occur in its calculation during model integration. Total Exner function is defined as:

$$\pi = C_p \frac{T_v}{\theta} \qquad \textbf{(3-5)}$$

where C_p is specific heat of air at constant pressure, T_v is virtual temperature, and θ is the potential temperature. The vertical momentum equation for the non-hydrostatic case is:

$$\frac{\partial w}{\partial t} = -u\frac{\partial w}{\partial x} - v\frac{\partial w}{\partial y} - w\frac{\partial w}{\partial z} - \theta\frac{\partial \pi'}{\partial z} - \frac{g\theta_v'}{\theta_0} + \frac{\partial(w'u')}{\partial x} + \frac{\partial(w'v')}{\partial y} + \frac{\partial(w'w')}{\partial z} \qquad \textbf{(3-6)}$$

I **II** **III** **IV** **V**

where term IV now represents buoyancy force.

Thermodynamic equation:

The thermodynamic state of the atmosphere is prognosed by:

$$\frac{\partial \theta_{il}}{\partial t} = -u\frac{\partial \theta_{il}}{\partial x} - v\frac{\partial \theta_{il}}{\partial y} - w\frac{\partial \theta_{il}}{\partial z} + \frac{\partial(u'\theta_{il}')}{\partial x} + \frac{\partial(v'\theta_{il}')}{\partial y} + \frac{\partial(w'\theta_{il}')}{\partial z} + \left(\frac{\partial \theta_{il}}{\partial t}\right)_{rad} \qquad \textbf{(3-7)}$$

I **II** **III** **IV**

Term I is total heating rate

Term II represents horizontal advection

Term III represents turbulent flux divergence

Term IV represents radiative flux divergence

θ_{il} is the ice-liquid water potential temperature. Ice-liquid water potential temperature instead of potential temperature is used in RAMS to avoid specification of latent heat tendencies in Equation (3-7). θ_{il} remains unchanged in the presence of all water phase changes as demonstrated by Tripoli and Cotton (1981).

Equation of mass continuity:

In the non-hydrostatic framework, the equation for mass continuity is expressed as:

$$\frac{\partial \pi'}{\partial t} = -\frac{R\pi_0}{C_v \rho_0 \theta_0}\left(\frac{\partial \rho_0 \theta_0 u}{\partial x} + \frac{\partial \rho_0 \theta_0 v}{\partial y} + \frac{\partial \rho_0 \theta_0 w}{\partial z}\right) \qquad \textbf{(3-8)}$$

Where ρ is air density, C_v is specific heat for air at constant volume, and R is the gas constant, and π_0, ρ_0, and θ_0 are synoptic scale reference values of these variables (Pielke 1984).

Equation of continuity for water species mixing ratio:

Tendency for water species mixing ratio (r_n) is calculated by:

$$\frac{\partial r_n}{\partial t} = -u\frac{\partial r_n}{\partial x} - v\frac{\partial r_n}{\partial y} - w\frac{\partial r_n}{\partial z} + \frac{\partial(u'r_n')}{\partial x} + \frac{\partial(v'r_n')}{\partial y} + \frac{\partial(w'r_n')}{\partial z} \qquad \textbf{(3-9)}$$

3.3.2 Grid Stagger

RAMS uses the standard C grid configuration after Mesinger and Arakawa (1976). Thermodynamic and moisture variables are defined at the same points, while the three velocity components u, v, and w are staggered 1/2 Δx, 1/2 Δy, and 1/2 Δz respectively (Figure 3.2). Figure 3.2a illustrates the horizontal cross section of the grid lattice structure with one nested grid. The coarse mesh, which is referred to as GRID 1 is represented by upper case letters denoting variable locations: U for west-east velocity, V for south-north velocity, and T for thermodynamic variables (all variables other than velocity components). GRID 2 is nested within GRID 1 with a finer mesh. The variables defined on GRID 2 are denoted by lower case letters completely analogous to grid 1. Figure 3.2b illustrates a vertical cross section of the grid lattice structure used in RAMS. Grid nesting is analogous to the horizontal cross section, except W and w are vertical velocity components for grids 1 and 2 respectively. Note that vertical grid nesting capability was not used for simulations presented in this thesis.

The map projection for the horizontal grid is a rotated polar-stereographic projection. The pole of the projection is rotated to an area near the centre of the model domain in order to minimize the distortion due to the projection.

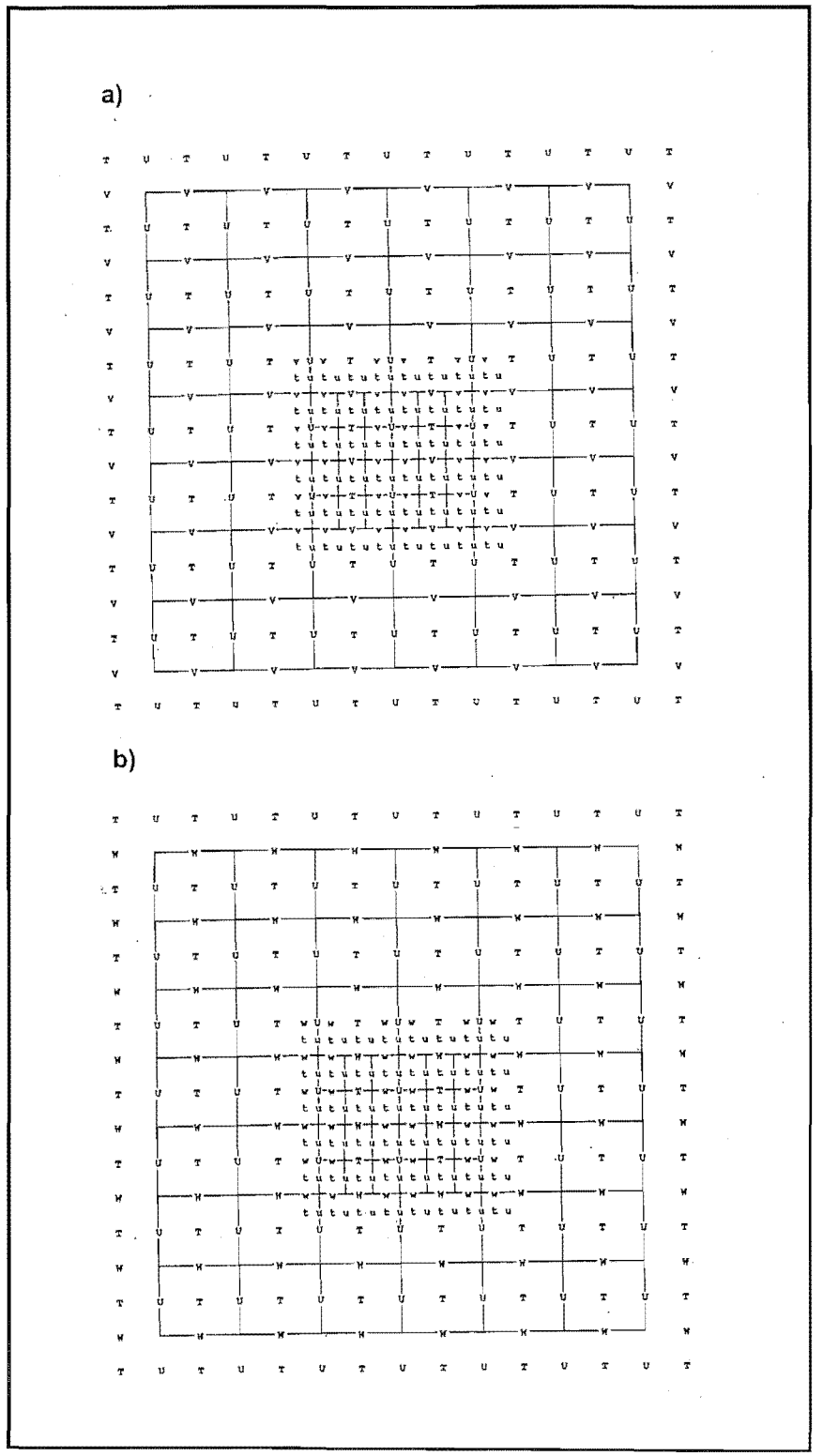

Figure 3.2: Illustration of Arakawa type C stagger, (a) horizontal cross-section of the grid lattice structure (b) vertical cross-section of the grid lattice structure. (Note: an explanation for the lattice structure and the symbols is provided in the text.)

3.3.3 Terrain-Following Coordinate System

In order to represent topography in mesoscale models, vertical terrain following coordinate systems are incorporated in their formulations. RAMS uses the σ_z terrain-following coordinate system (Gal-Chen and Somerville 1975; Clark 1977; Tripoli and Cotton 1982). The top of the model domain is exactly flat and the bottom follows the terrain. The coordinates in such a system are defined as:

$$\begin{aligned} x^* &= x \\ y^* &= y \\ z^* &= H\left(\frac{z - z_g}{H - z_g}\right) \end{aligned} \tag{3-10}$$

where H is the height of the top of the grid and z_g is local topography height which is a function of x and y. Derivative terms can be written in tensor notation according to Clark (1977) as:

$$\begin{aligned} \frac{\partial \phi}{\partial x_i} &= \left(\frac{1}{a}\right)\left(\frac{\partial a b_{ij} \phi}{\partial x_j^*}\right) \\ a(x^*, y^*) &= 1 - \left(\frac{z_g(x^*, y^*)}{H}\right) \end{aligned} \tag{3-11}$$

for i and j = 1,2,3 (three spatial dimensions), and the tensor b_{ij} can be written as:

$$b_{ij} = \begin{bmatrix} 1 & 0 & \frac{1}{a}\frac{\partial z_g}{\partial x}\left(\frac{z^*}{H} - 1\right) \\ 0 & 1 & \frac{1}{a}\frac{\partial z_g}{\partial y}\left(\frac{z^*}{H} - 1\right) \\ 0 & 0 & \frac{1}{a} \end{bmatrix} \tag{3-12}$$

A good explanation for tensor notation is provided by Stull (1988).

3.3.4 Vertical Levels

It is often desirable to have higher vertical resolution close to the ground so that the processes in the boundary layer are better resolved. As a result, in RAMS, the user can specify variable vertical grid spacings. An expansion ratio R_j can be defined as:

$$R_j = \frac{(\Delta Z)_j}{(\Delta Z)_{j-1}} \tag{3-13}$$

where

$$(\Delta Z)_j = Z_{j+1} - Z_j \tag{3-14}$$

large expansion ratios are often avoided (note that Z is the thickness of a vertical layer and should not be confused with z).

3.3.5 Grid Nesting

RAMS employs the grid nesting technique described in Clark and Farley (1984) and Clark and Hall (1991). In selected regions, grids with high spatial resolution can be nested within lower resolution grids. Any number of nested grids can be used, within the limits of available computer memory. Grids can be configured in a telescoping sequence where parent grids themselves are nested within coarser grids. A nested grid need not extend from the ground to the model top, and it can be moved horizontally during the simulation, this feature is useful in modelling thunderstorms or tropical cyclones in order to keep the phenomena within the high resolution grid.

The grid nesting technique carries out a two-way exchange of computed values for all prognostic variables between any nested grid and its parent grid. After each coarse grid timestep, the computed values are updated at the boundaries of the finer grid by interpolation. A nested grid usually runs with a shorter timestep than the parent grid, so that temporal linear interpolation is also performed to update values at the nested grid boundaries. The nested grid goes through several smaller timesteps and once it is updated to the same time as the parent grid, reverse communication is accomplished by averaging the prognostic variables over each set of nested grid cells which occupy a single parent cell, and replacing the parent grid value.

3.3.6 Turbulent Mixing Parameterization

The horizontal and vertical grid spacings of a simulation determine the spatial scales of the prognostic variables that can be explicitly resolved, while contribution from spatial scales smaller than the grid spacing have to be parameterized. Simulations performed for this thesis were set up to use the Mellor and Yamada (1974, 1982) technique for calculating vertical eddy mixing coefficients. Their so-called level 2.5 scheme predicts turbulent kinetic energy (TKE), with modification for the case of growing turbulence (Helfand and Labraga 1988). A local deformation scheme based on Smagorinsky (1963) is used to calculate horizontal diffusion, which is calculated as the product of horizontal deformation rate (horizontal gradients of horizontal velocity) and a length scale squared. A brief description of the vertical diffusion scheme is provided in this section.

The Mellor and Yamada scheme is based on a prognostic equation for the TKE (e) which is solved in the numerical model at each timestep. TKE is defined as:

$$e = \frac{1}{2}\left(\overline{u'^2} + \overline{v'^2} + \overline{w'^2}\right) \qquad \textbf{(3-15)}$$

while the prognostic equation for TKE is:

$$\frac{\partial e}{\partial t} = -u\frac{\partial e}{\partial x} - v\frac{\partial e}{\partial y} - w\frac{\partial e}{\partial z} + \frac{\partial}{\partial x}K_e\frac{\partial e}{\partial x} + \frac{\partial}{\partial y}K_e\frac{\partial e}{\partial y} + \frac{\partial}{\partial z}K_e\frac{\partial e}{\partial z} + P_S + P_b - \varepsilon \qquad \textbf{(3-16)}$$

P_S is the shear production term calculated by

$$P_S = K_m\left[\left(\frac{\partial u}{\partial x}\right)^2 + \left(\frac{\partial v}{\partial y}\right)^2\right] \qquad \textbf{(3-17)}$$

whereas P_b is the buoyancy production term determined from

$$P_b = -\frac{g}{\theta} K_h \frac{\partial \theta_v}{\partial z} \qquad \textbf{(3-18)}$$

and the viscous dissipation term is given by

$$\varepsilon = a_e \frac{e^{3/2}}{l} \qquad \textbf{(3-19)}$$

where l is the master length scale, the calculation of which is covered in Mellor and Yamada (1974). Once TKE is computed, the vertical eddy diffusivities for momentum (K_m), heat (K_h), and TKE itself (K_e) are determined from

$$\begin{aligned} K_m &= S_m l(2e)^{1/2} \\ K_h &= S_h l(2e)^{1/2} \\ K_e &= S_e l(2e)^{1/2} \end{aligned} \qquad \textbf{(3-20)}$$

where Sm, Sh and Se are nondimensional eddy diffusivities for momentum, heat and TKE respectively. Details of their calculation is provided in Mellor and Yamada (1982).

3.3.7 Surface Layer Parameterization

The Monin-Obukhov similarity theory provides the most suitable theoretical framework for the description of fluxes of heat, moisture and momentum in the surface layer. The basic similarity hypothesis for the surface layer was proposed by Monin and Obukhov (1954) for a horizontally homogenous flat terrain, under clear sky conditions. Little is known about the validity of the similarity theory in complex terrain. However, it seems that the similarity theory may be applied in complicated conditions since numerical models have relative success under such conditions. RAMS employs a scheme developed by Louis (1979) to compute the surface layer fluxes of heat, momentum, and water vapor. His scheme provides precomputed approximations of the flux profile functions of Businger *et al.* (1971), which need to be solved iteratively. The scheme determines fluxes between the land surface and the atmosphere for water surfaces, bare soil and vegetated surfaces. After the fluxes are computed, the values are

used as a lower boundary for the subgrid diffusion scheme. The equations for surface layer fluxes are:

$$
\begin{aligned}
u_*^2 &= a^2\, u^2\, F_m\left(\frac{z}{z_0}, Ri_B\right) \\
u_*\theta_* &= \frac{a^2}{R} u\, \Delta\theta\, F_h\left(\frac{z}{z_0}, Ri_B\right) \\
u_* r_* &= \frac{a^2}{R} u\, \Delta r\, F_h\left(\frac{z}{z_0}, Ri_B\right)
\end{aligned}
\qquad \textbf{(3-21)}
$$

where R is a constant representing the ratio of drag coefficients for momentum and heat in the neutral limit, which was estimated to equal 0.74 (Businger *et al.* 1971), z_0 is roughness length, u_* is velocity scale, θ_* is temperature scale, r_* is mixing ratio scale (Arya 1988; Louis 1979).

$$
a^2 = \frac{k^2}{\left(\ln\frac{z}{z_0}\right)^2} \qquad \textbf{(3-22)}
$$

where k is the Von Karman constant. F is evaluated for two conditions, for the unstable case it can be expressed as:

$$
F = 1 - \frac{b\, Ri_B}{1 + c\left|Ri_B\right|^{1/2}} \qquad \textbf{(3-23)}
$$

and for the stable case it can be expressed as:

$$
F = \frac{1}{\left(1 + b'\, Ri_B\right)^2} \qquad \textbf{(3-24)}
$$

Ri_B is the bulk Richardson number defined as:

$$
Ri_B = \left(\frac{g}{T_{zo}}\right)\left[\frac{(\theta - \theta_{zo})z}{U^2}\right] \qquad \textbf{(3-25)}
$$

where g is gravitational acceleration, T_{zo} and θ_{zo} are extrapolated roughness length values for temperature and potential temperature, and U is wind speed. The empirical constants b and b' are set to 9.4 and 4.7 respectively for both F_m and F_h (Louis 1979). The constant c is determined by the expression:

$$c = C^* a^2 b \left(\frac{z}{z_0} \right)^{1/2} \qquad \textbf{(3-26)}$$

where C^* is equals to 7.4 for F_m and 5.3 for F_h (Louis 1979).

3.3.8 Spatial Boundary Conditions

Most frequently, mesoscale models are configured to simulate atmospheric motion in a limited area (they are not designed to be global models), therefore the model domain has to be artificially enclosed with sides. Hence, it is necessary to assign values for the dependent variables at the perimeter of the model domain. These values are referred to as boundary conditions and have to be integrated in time similar to the interior regions of the domain. In mesoscale models, treatment of each boundary is different and they are referred to as the bottom, top, or lateral boundary.

a) Lateral Boundary Conditions

It is generally desirable to have the lateral boundary as far away from the region of interest as possible. Mesoscale models generally employ two types of lateral boundary conditions:

1) *open* lateral boundary, where mesoscale perturbations can pass into and out of the model domain
2) *closed* lateral boundary, where mesoscale perturbations are not permitted to enter or exit.

The general form of the lateral boundary condition used on the C-grid stagger of RAMS is the *radiative* condition. The radiative condition minimizes reflection of outward propagating perturbations within the flow, back into the interior of the model domain. For the east-west boundary, the specification at the lateral boundary is:

$$\frac{\partial u}{\partial t} = -(u+c)\frac{\partial u}{\partial x} \qquad \textbf{(3-27)}$$

where u is the wind component normal to the boundary, and c is the phase velocity. In RAMS, the phase velocity can be specified with several options. The option used for simulations in this thesis was proposed by Klemp and Wilhelmson (1978a, b) where c is a constant equal to the model domain height divided by the Brunt-Väisälä frequency multiplied by π. The Brunt-Väisälä frequency (N_{BV}) is defined by:

$$N_{BV} = \sqrt{\frac{g}{\theta}\frac{\partial \theta}{\partial z}} \qquad \textbf{(3-28)}$$

which is a measure of the static stability of the atmosphere.

For all other variables besides the normal velocity component a scheme called the zero-gradient condition was chosen. In this scheme, the value of each variable at the boundary is set to the value immediately adjacent to it in the interior (hence zero-gradient). This option gave the most desirable outcome for the simulations where the initial conditions were horizontally homogeneous.

RAMS provides the modeller with several different options for the treatment of the lateral boundary, the most suitable option is usually determined by performing numerical experiments. For the coarse grid of model simulations used in this thesis, the Klemp and Wilhelmson condition was activated. With this condition, the normal velocity component specified at the lateral boundary is effectively advected from the interior.

The two-dimensional simulations in Chapter 5 used the *cyclic* lateral boundary condition for the north-south direction. A *cyclic* boundary condition makes the model periodic in the y-direction, effectively eliminating the north-south lateral boundaries from the solution. This is achieved by forcing the values of dependent variables at one boundary to be identical to the value at the other end (Pielke 1984).

b) Top Boundary Conditions

For the non-hydrostatic equation set, two options for the treatment of the top boundary are offered in RAMS. A simple wall option is used for the simulations in this thesis.

With this option, the vertical velocity component is set to zero at the model top (w=0), which is recommended for simulations which are horizontally homogeneously initialized. For this case, a Rayleigh friction layer has to be applied to the top boundary to prevent the reflection of gravity waves from the model top. In the friction layer, an extra term is added to the basic prognostic equations so that the prognostic variables are *relaxed* (*nudged*) towards the horizontally homogenous reference state, by defining:

$$\frac{\partial \phi}{\partial t} = -\frac{(\phi - \phi_0)}{\tau} \qquad \textbf{(3-29)}$$

where ϕ represents the prognostic variables u, v, w, and θ, ϕ_0 is the initial value of these variables, and τ is a timescale. τ is a linear function of height and it's value can be set by the modeller. Usually a value between 60 and 300 seconds is chosen for the very top layer which has the strongest effect in damping the waves.

3.3.9 Soil and Vegetation Parameterization

The surface layer parameterization described above requires surface temperature and moisture values to calculate fluxes. In RAMS, the surface is divided into three different classes: water, bare soil and vegetated surface. For water surfaces, the code only allows for spatial variations in temperature, and since most simulations last a few days or less, no temporal variation is accommodated for in the code. In contrast, prognostic temperature and moisture models are used to provide predicted values for the land surfaces. For bare soil, RAMS uses the multi-layer soil model of Tremback and Kessler (1985), while for vegetated surfaces the model described by Avissar and Pielke (1989) is used.

Chapter 4

Three-Dimensional Numerical Modelling of the Regional-Scale Flow

4.1 Introduction

In Chapter 2, observational data showed the development of a strong easterly wind in MacKenzie Basin and Lake Tekapo region early in the afternoon during settled anticyclonic conditions in summer. It was concluded that, when the synoptic scale pressure gradients over the region are small, the daytime wind field in the basin is dominated by thermal forcings at two scales. Locally induced upslope and up-valley winds (which are the focus of numerical simulations in Chapter 6) are a common feature of surface flow until early in the afternoon, followed by a regionally induced, strong easterly current that penetrates the basin atmosphere through mountain passes and saddles in the foothills. As this wind seems to originate from the region east of the foothills (over the Canterbury Plains) it was named the Canterbury Plains Breeze (CPB). The exact nature of this circulation cannot be determined due to paucity of observational data inside and outside the basin.

Therefore, it is the aim of this chapter to conduct a preliminary investigation into the physical mechanisms responsible for this regional-scale circulation by performing three-dimensional numerical experiments with RAMS. In the following chapter, results from high resolution two-dimensional sensitivity experiments are presented in order to provide additional insight into the causes and nature of the CPB circulation. The objectives of this chapter are the following:

- to determine if RAMS is able to simulate the CPB circulation for the case study day
- to determine if this circulation can evolve in MacKenzie Basin exclusively from terrain heating
- to determine the extent to which the CPB intrusion into MacKenzie Basin is affected by sea breeze forcing.

To achieve these objectives, three-dimensional simulations using a realistic topographic configuration are performed, providing an additional analysis tool for improved understanding of the CPB circulation. The approach used is to successively remove forcing parameters from the simulations (from complex to simple) in order to investigate the nature of the regional scale flow. Therefore, the first simulation (designated as REG-ECM) includes the effects of evolving synoptic scale winds and land-sea contrasts on thermally driven circulations in the region. The second simulation (designated as REG-NOW) examines circulations developed solely in response to heating of the surface by removing large scale winds. The third simulation removes another forcing parameter by replacing the ocean around New Zealand with land, therefore eliminating the influence of sea-breeze circulations. Table 4.1 provides a summary of the three-dimensional simulations.

Table 4.1: Summary of 3-D simulations conducted.

Name	Description	Purpose
REG-ECM	ECMWF nudged	Regional-scale circulation response to synoptic forcings
REG-NOW	No synoptic-scale pressure gradient	Response to surface heating alone
REG-NOS	Same as above, plus no ocean	To examine the role of the sea breeze

4.2 Numerical Experiments

The case study day chosen for the numerical simulations is February 12, 1999. Details on synoptic scale conditions and local observations for this day are provided in Chapter 2. Simulations are initialized on the evening of February 11 to let the model cycle through a nocturnal phase before the onset of surface heating the next day. This allows the model to have some "spin-up" time in adjusting the flow fields to the complex topography of New Zealand, and to allow simulated radiative cooling to produce more realistic low level stratification over the complex terrain.

The horizontal spatial resolution and grid structure of the simulations are chosen to simulate forcings at meso-β scale (20 – 200 km), with the main features of MacKenzie Basin topography (and hence the underlying thermal forcing) well represented. Two different methods are utilized for initializing the model, as described below. REG-ECM includes effects of variable winds from the evolving synoptic-scale circulation (Table 4.1). REG-NOW (no initial wind field) run is initialized with the atmosphere at rest, and only a single vertical profile for temperature and humidity is specified for the whole domain (horizontally homogeneous initialization). The flow fields generated by this run should evolve due to terrain cooling/heating alone. The ocean surrounding New Zealand is removed from the REG-NOS (no sea) domain to further eliminate circulations produced by land-sea contrasts. The initialization of this third run is similar to REG-NOW.

4.2.1 Three-Dimensional Simulation Development

a) Grid Structure

Horizontal grid-nesting capability of the model is used for the three-dimensional simulations. Grid nesting allows focusing of higher spatial resolution on the desired regions within the domain for greater computational efficiency (for details refer to Chapter 3). Table 4.2 provides a summary of the settings for each nested grid. Simulations in this chapter use three grids: the coarse grid covering New Zealand has a 36 km horizontal resolution, the first nested grid (grid 2) has a horizontal resolution of 12 km covering the

South Island, and the second nested grid (grid 3) has a horizontal resolution of 4 km covering the middle third of the South Island (Figure 4.1). Grid 1 is centered at 171°W and 42°S, while grids 2 and 3 are both centered at 171.4°W and 44°S. The three grids consist of 52, 62, and 50 zonal and meridional grid cells, respectively (Table 4.2).

Vertical grid-nesting capability of RAMS was not employed for these simulations, therefore each grid has 32 vertical layers, with a 50 m vertical grid spacing in the lowest layer (Table 4.2). The thickness increases geometrically by the ratio of 1.12 over the first 27 model layers to about 7 km AGL and remains at a constant thickness of 1 km over the final 5 layers until the top of the model domain is reached at 12 km AGL. The Rayleigh friction damping scheme is applied to the four vertical layers below the upper boundary to suppress vertically propagating gravity waves for REG-NOW and REG-NOS experiments. Since REG-ECM is initialized inhomogeneously with ECMWF data, top boundary nudging (which also damps gravity waves) was applied to the vertical layers above 7 km AGL.

Table 4.2: Characteristics of the grids used for the three-dimensional model runs.

	Grid 1	Grid 2	Grid 3
Number of east-west nodes	52	62	50
Number of north-south nodes	52	62	50
Number of vertical nodes	32	32	32
Δx, Δy (km)	36	12	4
East-west width (km)	1836	732	196
North-south width (km)	1836	732	196
Δz at first level (m)	50	50	50
Vertical stretch ratio	1.12	1.12	1.12
Grid top (km)	12	12	12
Δt (s)	20	6.7	2.2

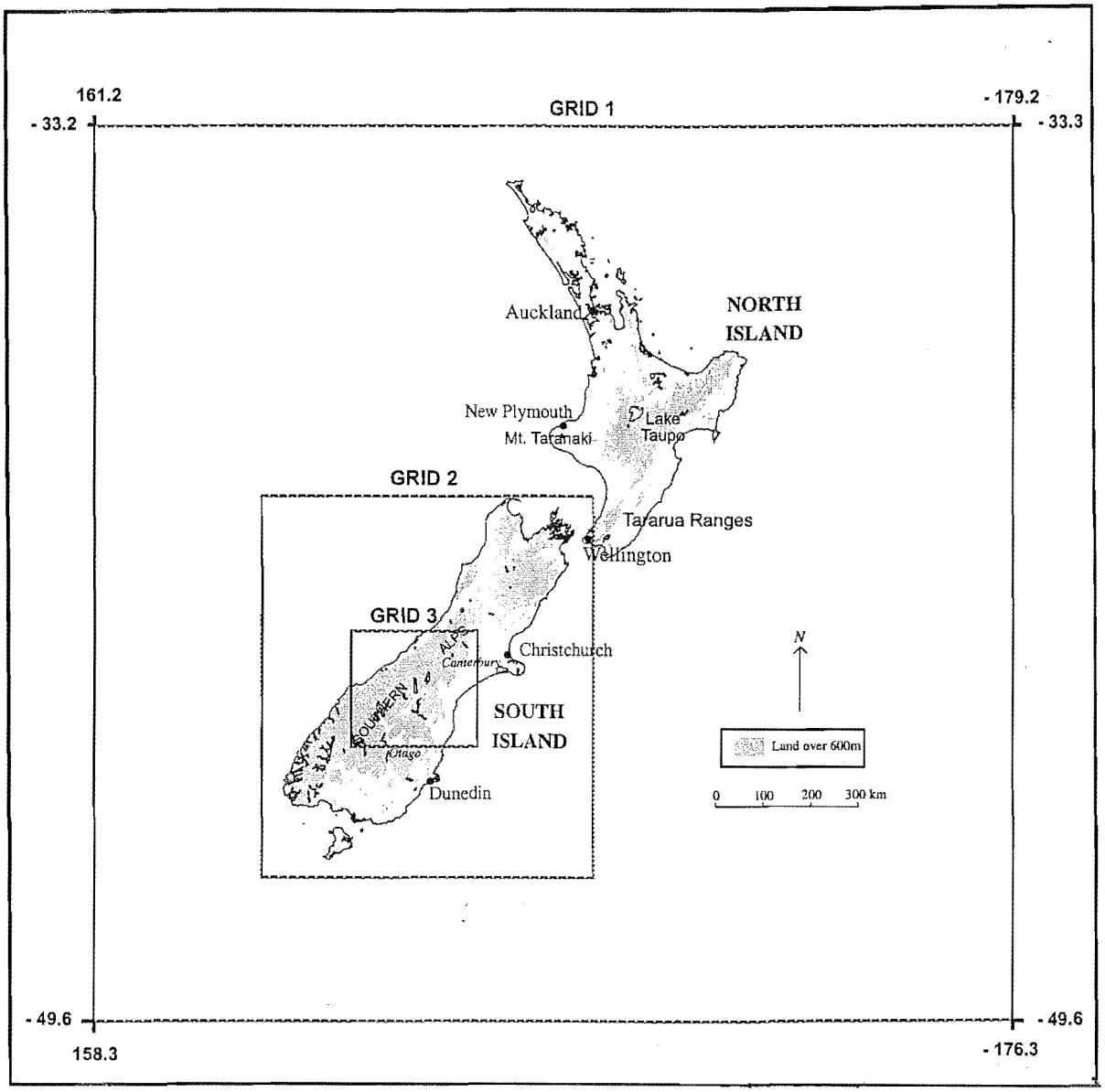

Figure 4.1: Geographic locations of grids 1, 2, and 3 for the three-dimensional simulations.

Topography for all grids is derived from the 30-second (about 1 km) terrain dataset from the U.S. Geological survey (USGS) and smoothed with a silhouette-averaging scheme that preserves realistic topographic heights. The averaging scheme and the horizontal grid spacing for grid 3 resolves the dominant terrain features of MacKenzie Basin and the surrounding regions, including coastal regions on both sides of the main divide (as shown in Figures 4.2, 4.3). Since the horizontal spatial resolution for this grid is 4 km, finer topographic features like the Godley and Macaulay Valleys are not well resolved. Therefore, the model is not able to produce thermally induced flows forced by these features (meso-γ scale circulations). As the main objective of this chapter is simulating regional-scale (meso-β) forcings, it is only important to have the

basin and the surrounding region well represented. The finer resolution effects are dealt with in Chapter 6.

b) Model Setup

Table 4.3 provides a summary of the model setup. Since the main focus of this investigation is on circulations induced by heating of orography alone, the surface characteristics (for land) are specified homogeneously for the entire domain. This prevents development of non-classical thermally induced flows. Non-classical flows result from variation in surface characteristics such as soil moisture and vegetation cover, which can complicate surface flow field further. Hence, when a numerical modeller is interested in studying flows due to orography alone, a common practice is the homogenous specification for surface characteristics. Soil type was specified as sandy loam, and soil moisture was set at a relatively dry 30% of saturation over the entire model domain. Desert parameterization (no vegetation effects) was used for all grids.

Table 4.3: Summary of model setup.

Soil type	Sandy loam
Vegetation type	Desert (no vegetation)
Soil moisture (% of saturation)	30
Sea surface Temperature	16°C
Roughness length	10 cm
Coriolis force	Activated
Time differencing	Hybrid
Radiation scheme	Longwave and shortwave (Chen and Cotton 1983)

4.3 REG-ECM Simulation

4.3.1 Initialization

The REG-ECM simulation was started at 1800 NZST 11 February 1999 (0600 UTC 11 February 1999) and run continuously for a period of 30 hours until 2400 NZST 12 February 1999 (1200 UTC 12 February 1999). The run is initialized with the European

Centre for Medium Range Weather Forecasts (ECMWF) 1° gridded pressure level data at 1800 NZST 11 February 1999 (0600 UTC 11 February 1999). These data are interpolated onto an isentropic grid at specified levels, using a scheme developed by Tremback (1990). The gridded isentropic data are then interpolated onto the coarse model grid, after which the nested grids are initialized by interpolation from the coarse grid. Similar fields are prepared for the subsequent four periods when the ECMWF data are available (spaced at 6 hourly intervals) and are used to nudge only the lateral regions of grid 1. No nudging is done on the interior of grid 1 or any part of grid 2 or 3. Therefore, information on large-scale atmospheric conditions are continuously updated in the lateral regions of the coarse domain, and the model constantly adjusts to the evolving synoptic-scale fields. Simultaneously, model solutions at smaller scales are determined by mesoscale circulations driven by topography and surface heating/cooling within the boundary layer.

4.3.2 Simulation Results

Figure 4.2 illustrates the interaction between synoptic scale winds and the thermally driven circulations. This figure shows the predicted near surface wind at 25 m AGL after 12 and 20 hours of integration (0600, 1400 NZST respectively). The influence of synoptic scale winds (anticyclonic circulation) is apparent around the periphery of the domain for the two time periods shown (Chapter 2 provides a description of the synoptic-scale circulation at this time). Drainage winds due to overnight radiative cooling of the land are the dominating feature around the Southern Alps at 0600 NZST (Figure 4.2a). As the solar insolation heats up the South Island land mass, a converging wind field is produced by the heat low as shown in the 1400 NZST map (Figure 4.2b). Thermally driven circulations consist of sea breezes at the coast and upslope (mountain-induced) winds further inland. The formation of the Canterbury north-easterly circulation is evident north of Banks Peninsula. South of the peninsula, the sea breeze and mountain-induced winds are responsible for the south-easterly flow.

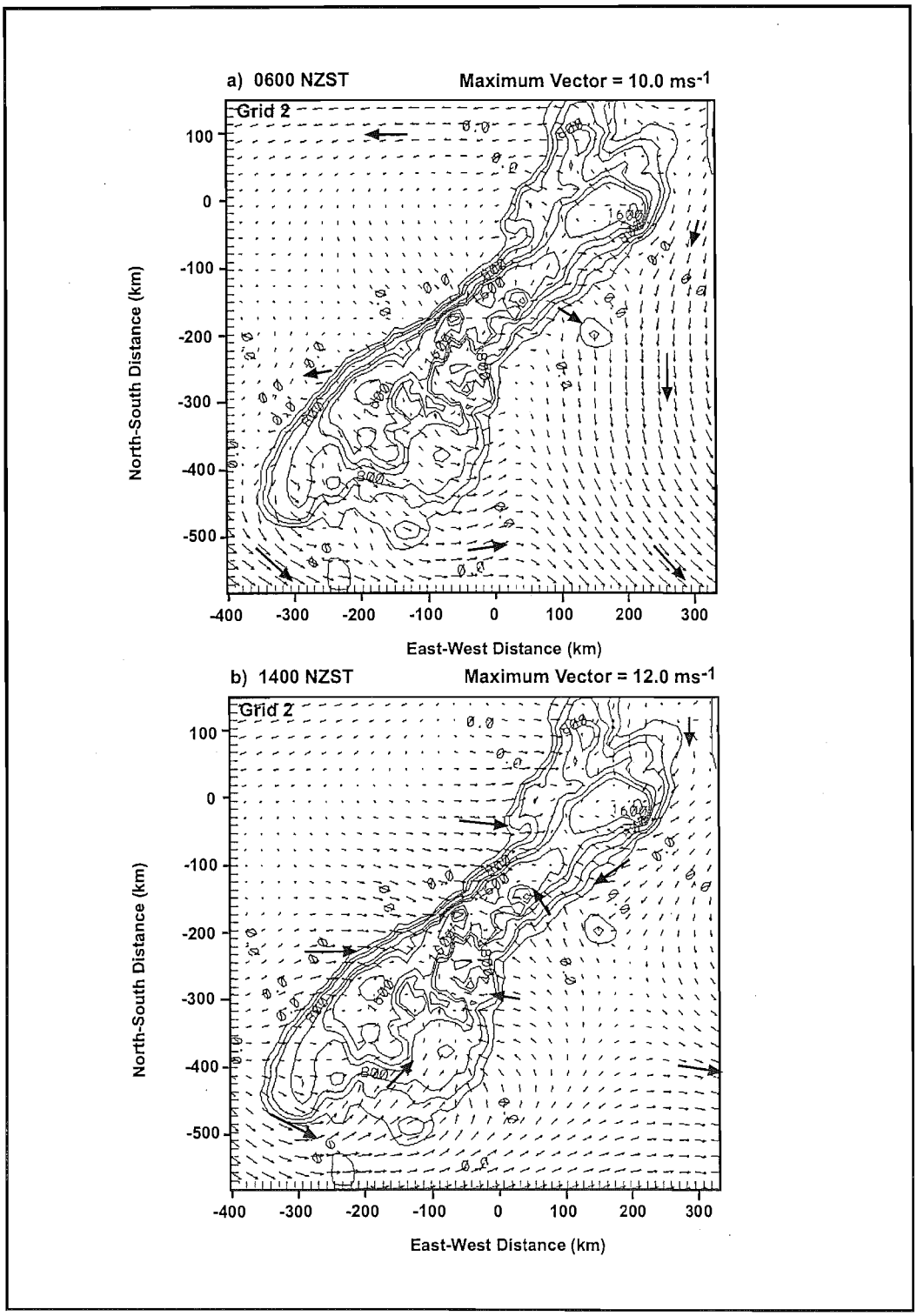

Figure 4.2: Topography (200 m contour interval) and wind vectors on grid 2 at 24 m AGL for (a) 0600 NZST, and (b) 1400 NZST for the REG-ECM simulation.

Predicted near surface wind fields for the third grid after 17, 20, 22, 24 hours of integration (1100, 1400, 1600, 1800 NZST respectively) are presented in Figures 4.3 and 4.4. Model solutions for this grid provide more detailed predicted wind fields for the MacKenzie Basin region. Heating of the surface has resulted in several types of thermally induced flows by 1100 NZST (Figure 4.3a). On the west coast, a coupled sea breeze and upslope wind has generated a circulation perpendicular to the coastline and the main divide. Similar to the west coast, heating of the slopes and the land on the eastern side has set up flows perpendicular to the topographic gradient and the coast on the Canterbury Plains. In MacKenzie basin, a divergent flow has been generated by local upslope wind system (Figure 4.3a). These upslope wind circulations are widespread around the basin periphery.

Later in the afternoon at 1400 NZST, the coupled sea breeze and upslope wind system is still apparent east of the foothills. An easterly flow has begun to intrude into the basin over the foothills (Two Thumb Range) and through Burke Pass (Figure 4.3b). Two hours later at 1600 NZST, the easterly intrusion has totally dominated the flow in MacKenzie Basin, overwhelming the locally generated thermally driven wind systems (Figure 4.4a). A major convergence line exists along the main divide. The easterly current has maintained its intensity at 1800 NZST, even though the circulation systems on the foothills have started to weaken since surface heating is not as strong at this time of day (Figure 4.4b).

To demonstrate the ability of the model to simulate observed regional scale conditions within MacKenzie Basin, a comparison is made of measured and modelled wind speed and direction (Figure 4.5). Data from the lowest level of the nested grid (~25 m AGL) are compared with the Base station located just south of Tekapo village. Data from the model were simply taken from a grid point closest to the geographical location of the Base station (Figure 2.3). It has to be pointed out that the model outputs are volume averages on a horizontal 4 km by 4 km grid, whereas the observations that they are compared to are point values that may in reality differ significantly from the averages due to local topographic effects.

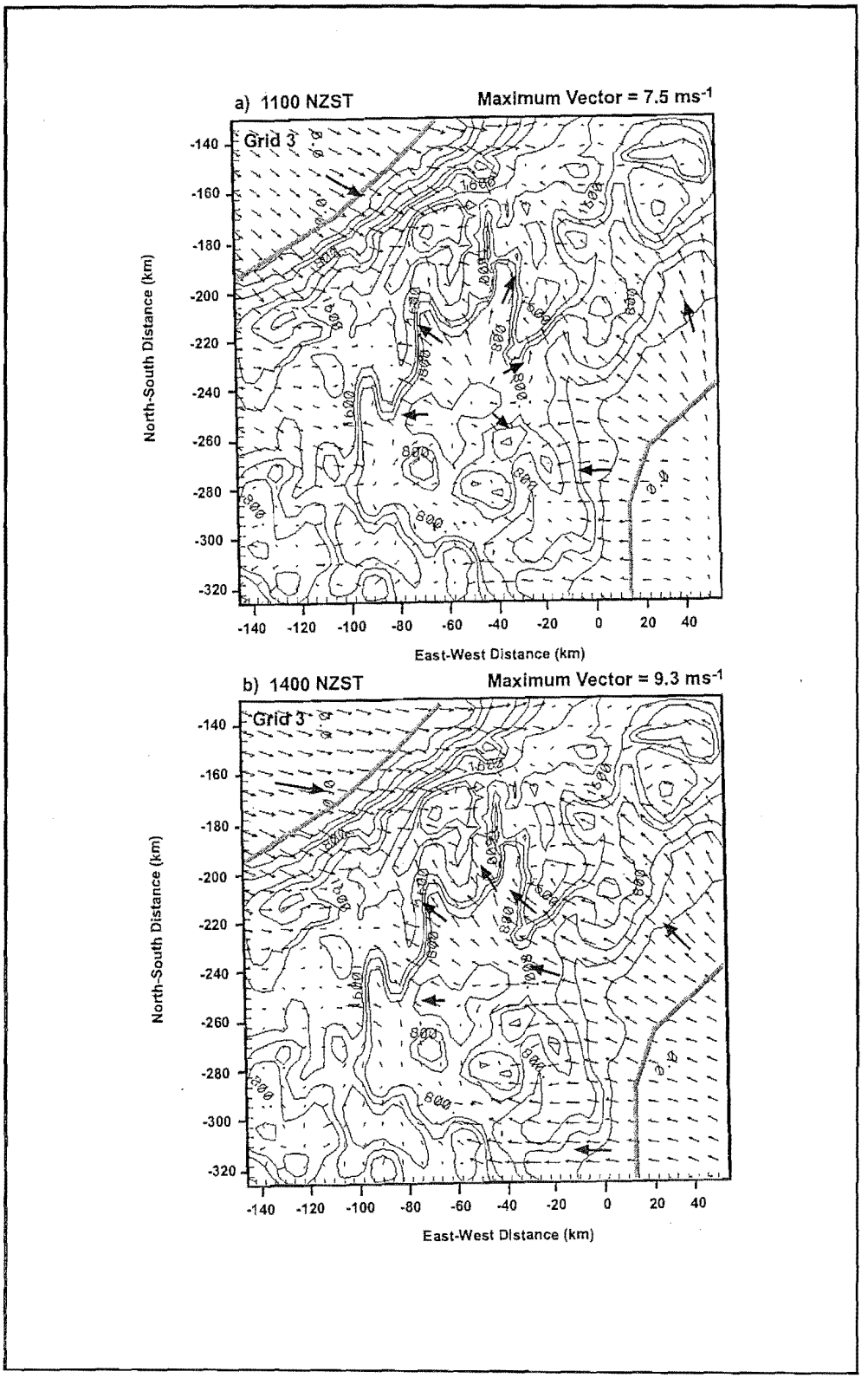

Figure 4.3: Topography (200 m contour interval) and wind vectors on grid 3 at 24 m AGL for (a) 1100 NZST, and (b) 1400 NZST for the REG-ECM simulation.

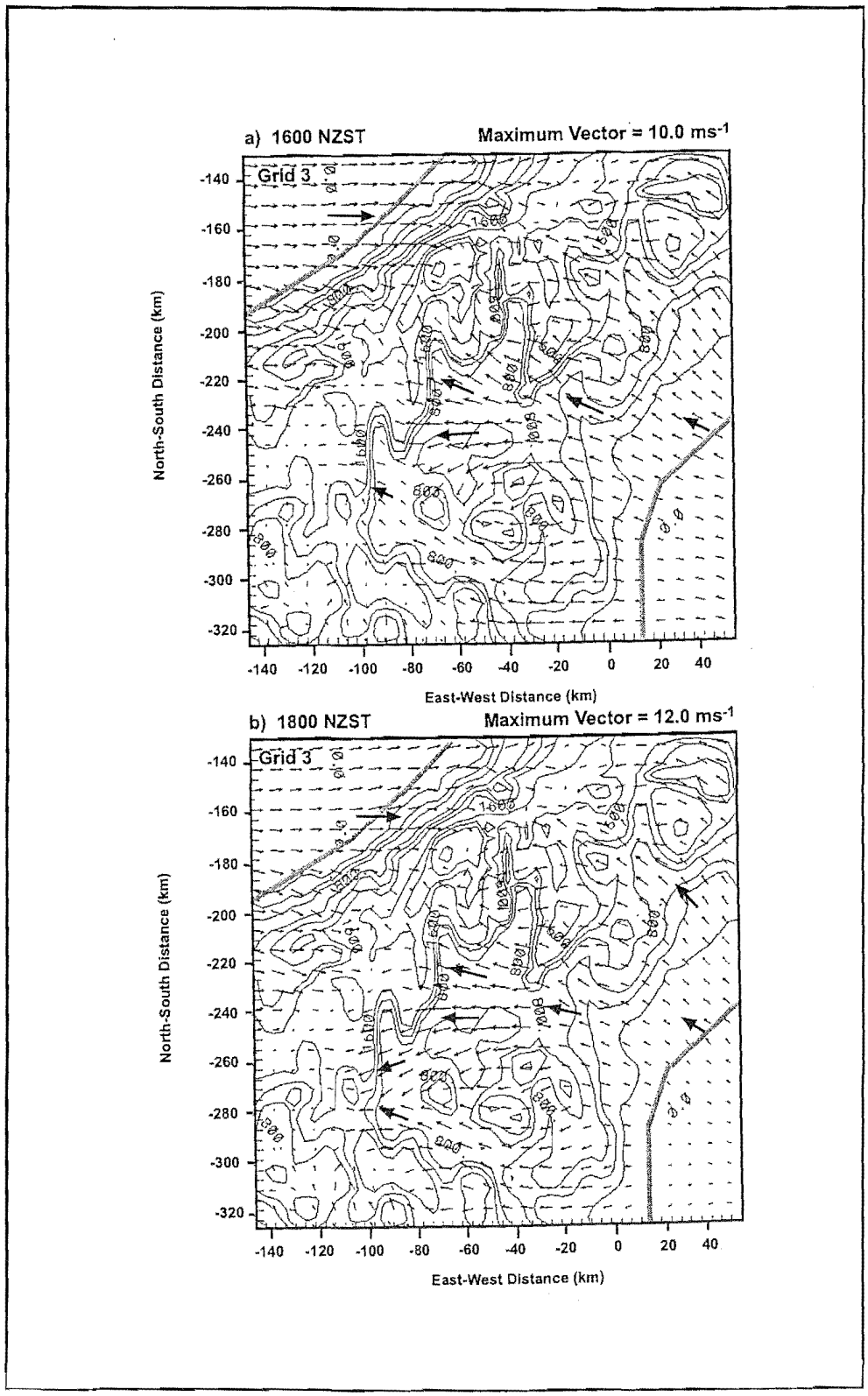

Figure 4.4: Topography (200 m contour interval) and wind vectors on grid 3 at 24 m AGL for (a) 1600 NZST, and (b) 1800 NZST for the REG-ECM simulation.

Since the finer topographic features of the basin are not resolved in this grid, the model does a poor job of predicting wind direction from 0600 to 1400 NZST (Figure 4.5a). Over this period, air-flow in MacKenzie Basin is dominated by locally generated thermal circulations, so that the spatial horizontal resolution is insufficient to resolve these flows (modelling results for the local scale are presented in Chapter 6). However, the onset of the regional scale circulation at this location is well predicted by the model, so that at 1400 NZST both the model and the station show the onset of a south-easterly current with a wind speed of 8 – 12 ms^{-1} (Figure 4.5b). The modelled and observed wind directions veer slightly till 2000 NZST, when there is a sudden decrease in wind speed and shift in wind direction of the observed wind which the model does not predict (Figure 4.5). The idealized simulations presented in the next section have more success in predicting the cessation time of the easterly current. The failure of REG-ECM to predict the cessation is due to interpolation of coarse ECMWF data, resulting in the atmosphere outside the basin being cooler than the idealized runs (figures not provided here). Hence, the horizontal temperature gradient that forces the easterly exists for much longer in the simulation. The results could be improved by assimilation of vertical profiles of temperature outside the basin if data were available. However, in summary, REG-ECM manages to simulate the regional mesoscale circulations adequately and demonstrates the ability of RAMS to model the main features of the CPB.

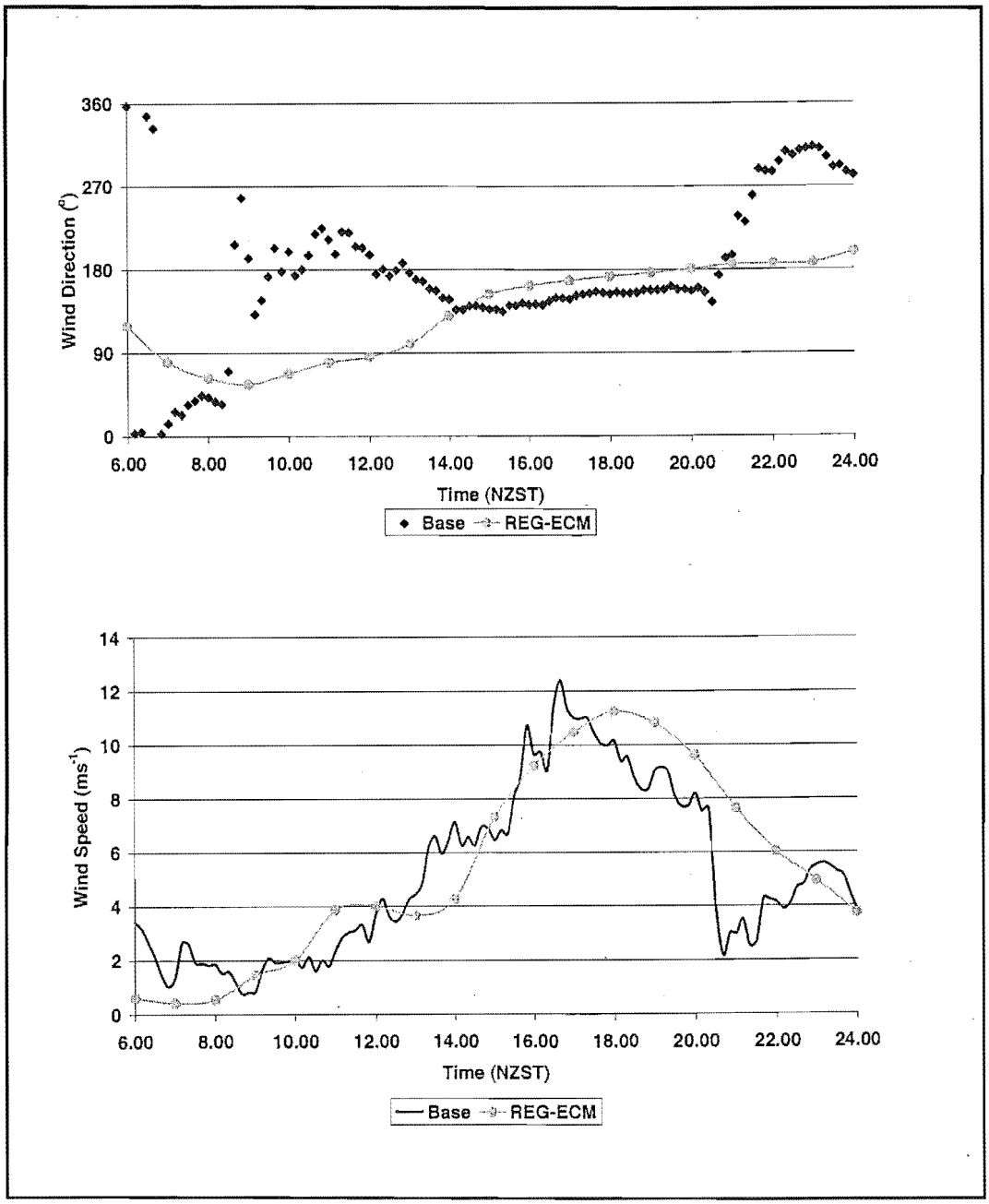

Figure 4.5: Time series of (a) wind direction, and (b) wind speed for 12th February at the Base site compared with prediction by REG-ECM simulation. Note that the measured data are ten minute averages, and the modelled data are instantaneous values.

4.4 Idealized Regional-Scale Simulations

Results from the REG-ECM simulation were encouraging, with RAMS performing a reasonably realistic simulation of the regional scale inflow into MacKenzie Basin. In this section, results from two idealized simulations are presented without additional

complications from external forcing parameters such as variable synoptic scale winds. The experiment designated as REG-NOW (regional scale, no wind) is designed to simulate regional scale winds in response to terrain heating alone. The ocean surface is removed from the REG-NOS (regional-scale, no sea) simulation in order to remove sea breeze effects in this run and to test the hypothesis that the CPB is a sea breeze intrusion into MacKenzie Basin. This is examined in more detail in Chapter 5.

4.4.1 Initialization

Both of the runs are initialized horizontally homogeneously using the same vertical temperature and humidity data constructed by blending the 1900 NZST 11 February 1999 profile measured by the aircraft in the basin (Chapter 2), and the 0000 NZST 12 February 1999 Invercargill rawinsonde profile (Figure 4.6). As no vertical temperature data were available below the basin elevation (660m), the mixed layer profile in the basin was simply extrapolated to sea level. To isolate thermal forcings, the integration started with the atmosphere at rest (no initial wind field imposed).

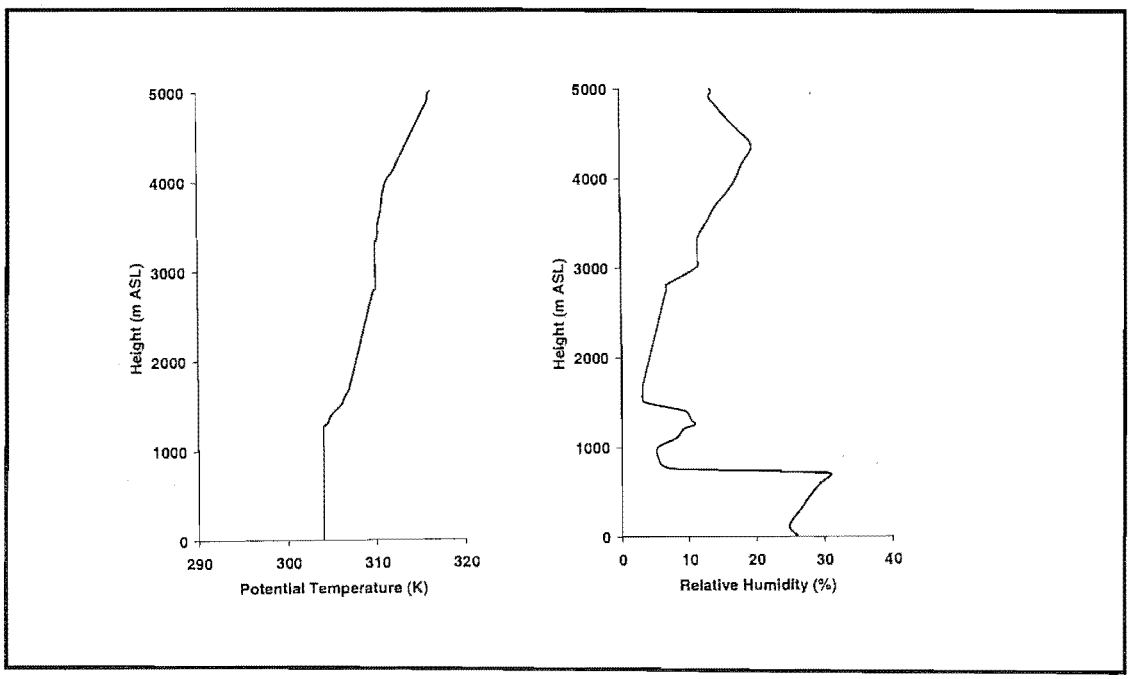

Figure 4.6: Vertical profiles of potential temperature and relative humidity at 1900 NZST on 11th February used to initialize the idealized three-dimensional simulations.

4.4.2 Simulation Results

As the model cycles through a nocturnal period first, it would be instructive to examine low level temperature stratification in the morning. Figure 4.7 presents simulated vertical potential temperature profiles over a grid point in MacKenzie Basin and the Canterbury Plains at 0600 NZST. Surface radiative cooling overnight has resulted in temperature inversions at both sites. The atmosphere inside the basin has a more stable profile due to cold air advection from the side walls leading to the formation of a cold air pool. Pooling of cold air occurs in basins that are topographically enclosed and the enhanced stability has been simulated and investigated by Fast *et. al* (1996) for Sinbad Basin in the United States. Figure 4.7 shows that the air within the basin is significantly cooler than at the same altitude over the coastal plain.

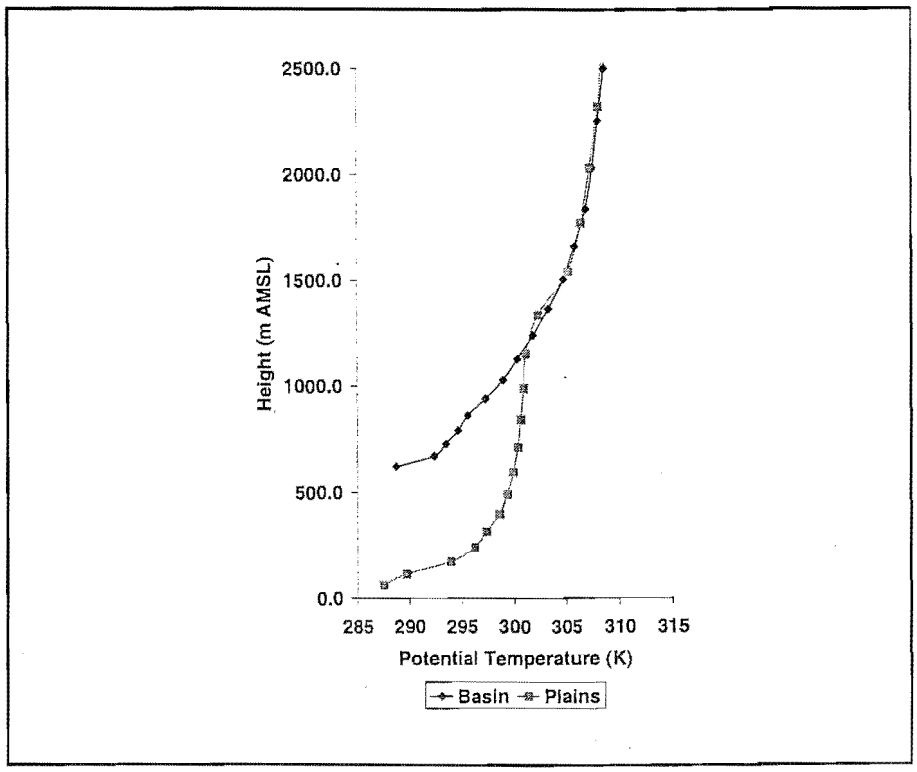

Figure 4.7: Simulated vertical profiles of potential temperature at 0600 NZST on 12th February over a grid point inside the basin and over the Canterbury Plains extracted from REG-NOW model run.

Simulated surface winds, and cross-sections of potential temperature and wind vector at 1200, 1600 and 2000 NZST are presented in Figures 4.8, 4.9 and 4.10 for the REG-NOW simulation. Similar to REG-ECM, at 1200 NZST (18 hours into the simulation) mountain-induced flows are evident on the Canterbury Plains and the west coast (Figure 4.8a). Since the basin atmosphere had a stronger static stability in the morning due to the cold air pool, the mixed layer inside the basin is much shallower than the mixed layer just east of the foothills at this time (Figure 4.8b). This suppression of mixed layer growth has been observed by Kondo *et al.* (1989) in basins and valleys in Japan. By 1600 NZST, the easterly is dominating the surface flow regime in MacKenzie Basin (Figure 4.9a), and the sea breeze and upslope circulations outside the basin have intensified. Cold air advection by the sea breeze has inhibited mixed layer growth close to the coast (Figure 4.9b). However, the mixed layer grows deeper further inland, although at this stage, the CPB is advecting cooler coastal air into the basin. By 2000 NZST, the day time thermally generated circulations outside the basin have ceased due to the change of sign of surface sensible heat flux, but the easterly current is still evident in MacKenzie Basin (Figure 4.10a). A horizontal temperature differential between the air in the basin and the air at the same elevation over the plains still exists at this time, so the forcing for the CPB is still in place.

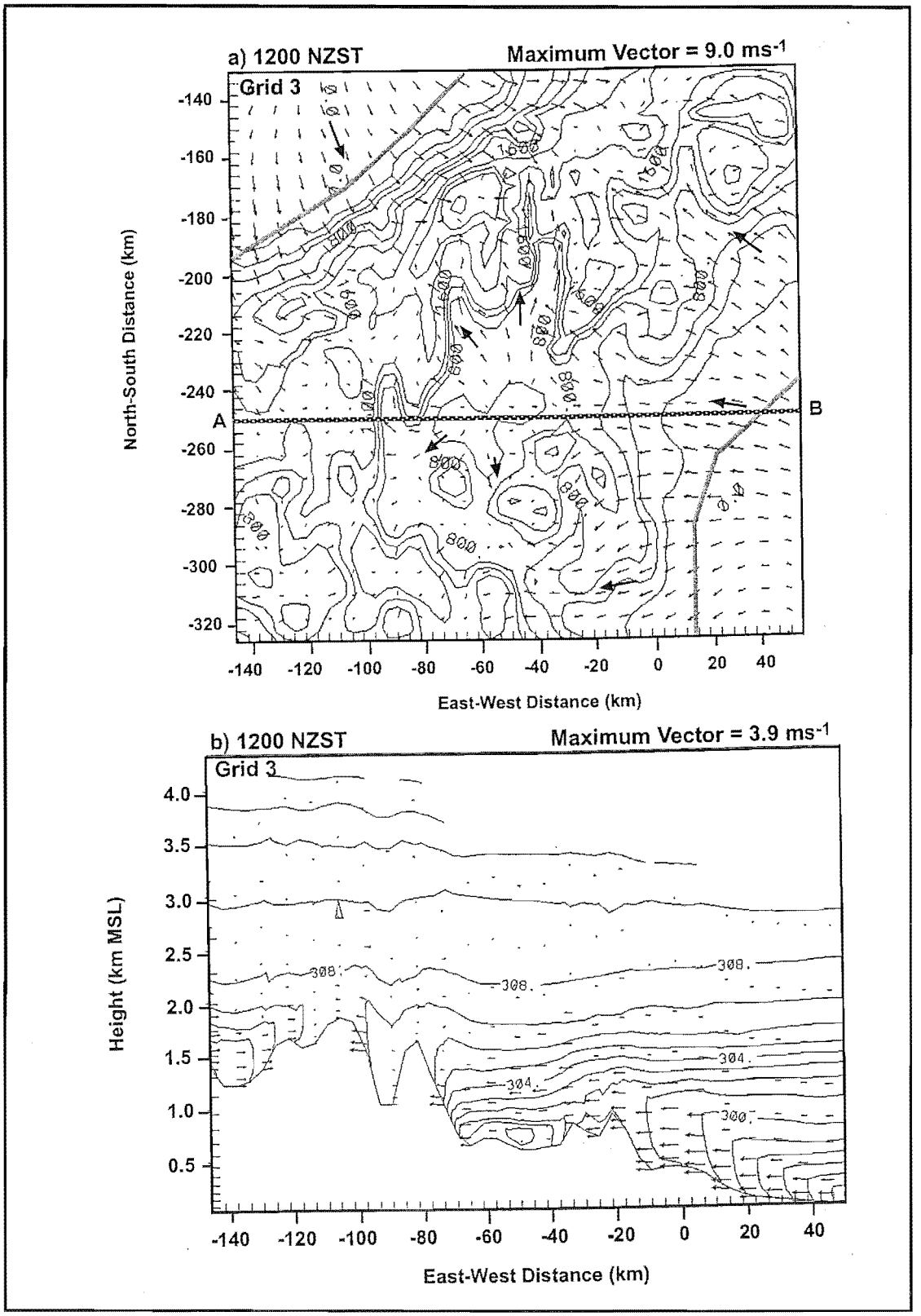

Figure 4.8: REG-NOW prediction at 1200 NZST for (a) wind vectors at 24 m AGL, and (b) vertical potential temperature field and wind vectors (through line A-B). Topography contour interval is 200m and potential temperature contour interval is 1K.

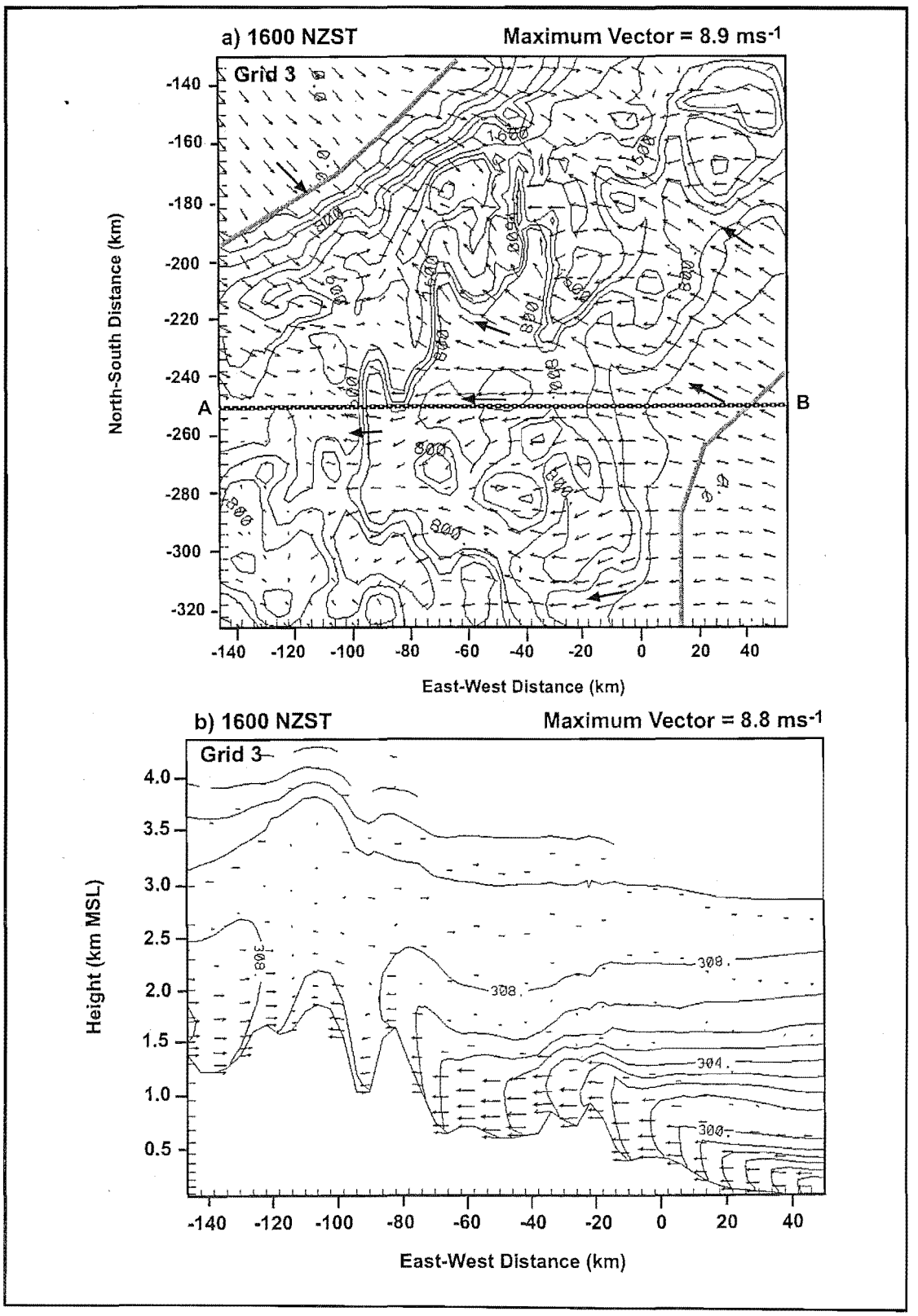

Figure 4.9: REG-NOW prediction at 1600 NZST for (a) wind vectors at 24 m AGL, and (b) vertical potential temperature field and wind vectors (through line A-B). Topography contour interval is 200m and potential temperature contour interval is 1K.

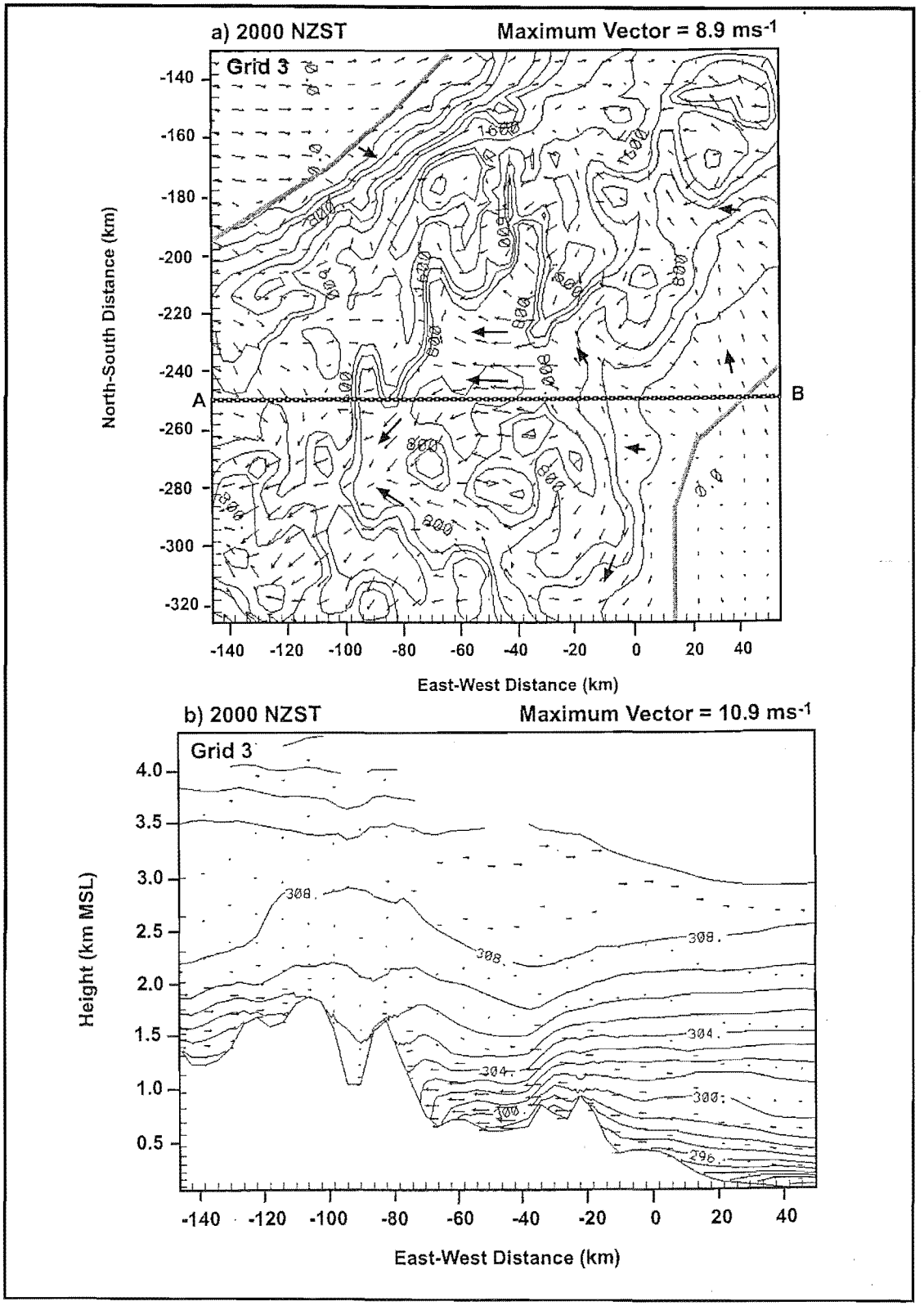

Figure 4.10: REG-NOW prediction at 2000 NZST for (a) wind vectors at 24 m AGL, and (b) vertical potential temperature field and wind vectors (through line A-B). Topography contour interval is 200m and potential temperature contour interval is 1K.

Figures 4.11, 4.12 and 4.13 present simulated surface wind field and cross-sections of potential temperature and wind vectors for the same time period as above, but for the REG-NOS. The onshore surface wind outside the basin on both sides of the main divide is weaker due to the absence of the ocean, and hence the lack of a sea-breeze component. The difference is just noticeable over the Canterbury Plains at 1600 NZST (Figures 4.9a and 4.12a). However, the mixed layer has grown to a depth of 1000 m over the plains, compared to a few hundred meters in the REG-NOW run (Figures 4.9b, 4.12b). A mountain-induced converging circulation with weaker return flows aloft had developed by this time (Figure 4.12b). The Canterbury Plains Breeze is dominating the surface flow structure in the basin as before, even though the sea breeze is absent (Figure 4.12a). With the decline of surface heating, the thermally induced circulations outside the basin have ceased by 2000 NZST, but similar to REG-NOW, the CBP current is still evident in the basin (Figure 4.13).

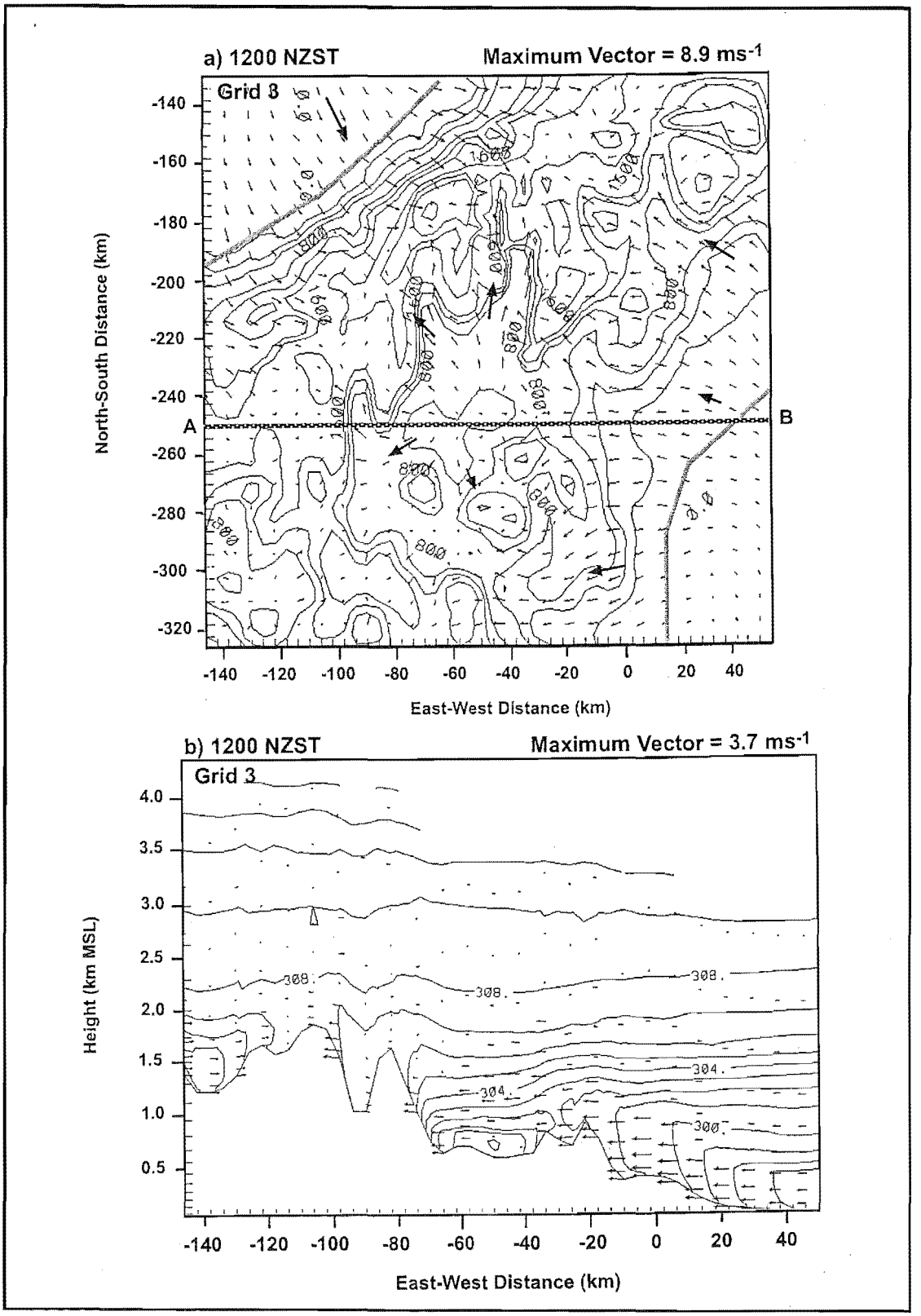

Figure 4.11: REG-NOS prediction at 1200 NZST for (a) wind vectors at 24 m AGL, and (b) vertical potential temperature field and wind vectors (through line A-B). Topography contour interval is 200m and potential temperature contour interval is 1K.

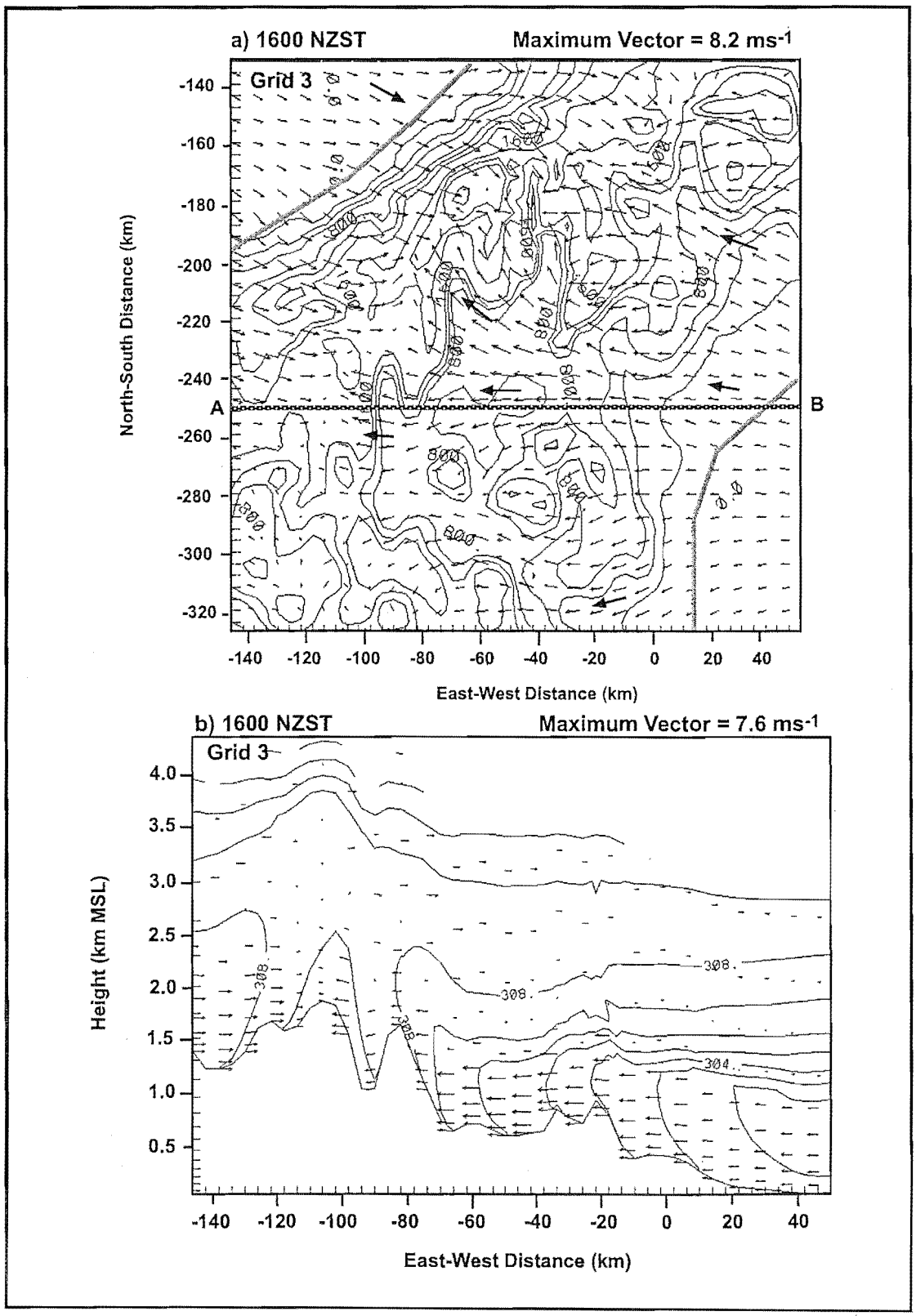

Figure 4.12: REG-NOS prediction at 1600 NZST for (a) wind vectors at 24 m AGL, and (b) vertical potential temperature field and wind vectors (through line A-B). Topography contour interval is 200m and potential temperature contour interval is 1K.

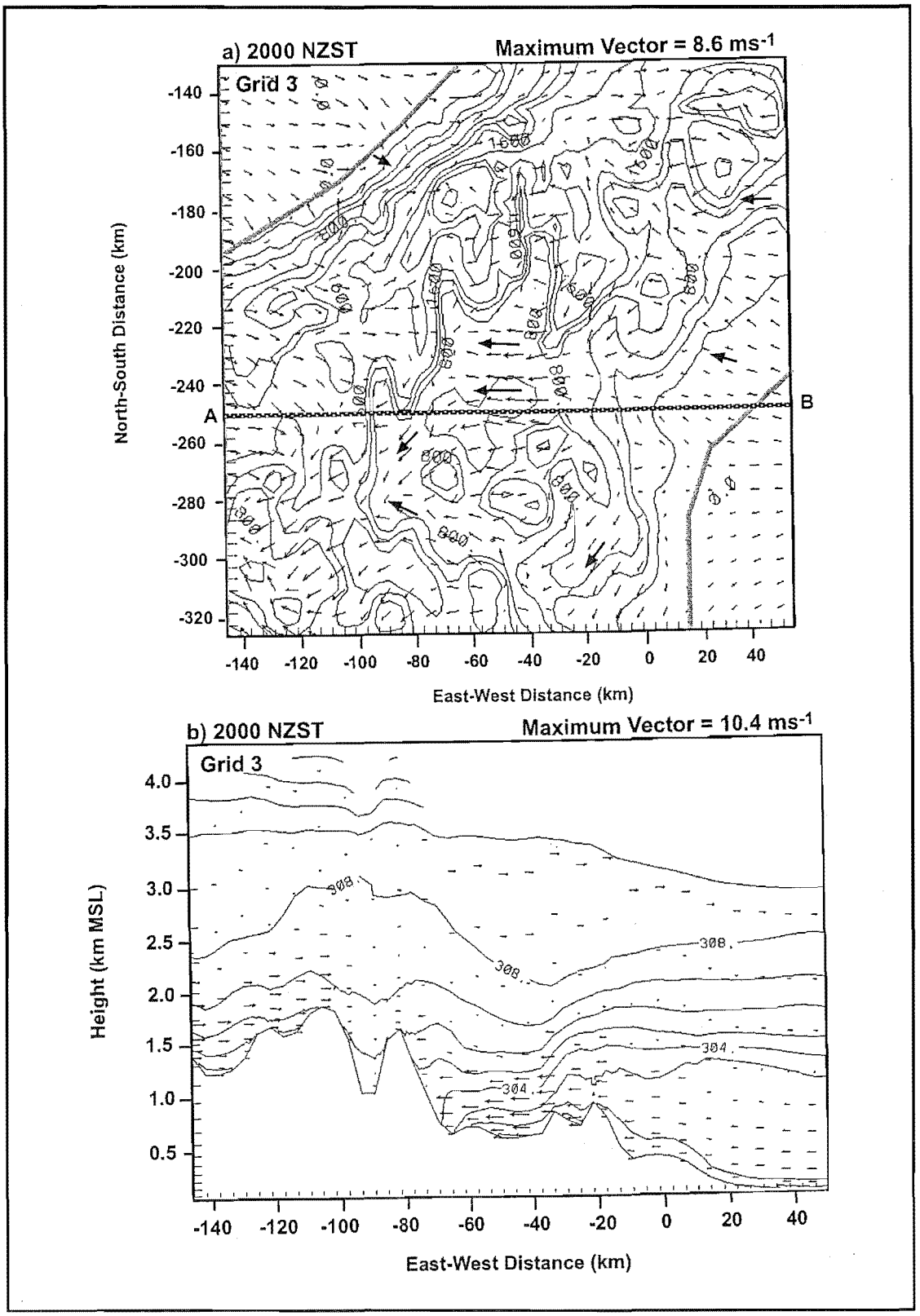

Figure 4.13: REG-NOS prediction at 2000 NZST for (a) wind vectors at 24 m AGL, and (b) vertical potential temperature field and wind vectors (through line A-B). Topography contour interval is 200m and potential temperature contour interval is 1K.

4.5 Discussion of Results

Like the REG-ECM analysis from the previous section, comparison of simulated data with observational data from the Base station is presented in Figure 4.14. RAMS performed a satisfactory prediction of onset and cessation time of CPB at this location when compared to data for 12th February 1999 (Figure 4.14a). At 1700 NZST, when the current reaches its maximum intensity, there is a difference of 1 ms^{-1} (11 %) between the two idealized runs (Figure 4.14b). Thereby showing that the CPB is not influenced significantly by the absence of land-ocean contrasts outside the basin. This slight reduction in intensity might be due to changes in the horizontal temperature gradients between the air inside and outside the basin for the two idealized runs. Several sensitivity experiments are performed in Chapter 5 to investigate this aspect further.

An additional comparison between observational data and model results is made for the Timaru weather station (Figure 2.1 in Chapter 2) to test the model's performance in predicting the wind field outside the basin. This station is about 6 km from the coast and is situated roughly 20 km from the foothills. Therefore, the wind on fair weather days is expected to be controlled by thermal influences from both orography and the land-sea contrast. Figure 4.15 presents a comparison of hourly instantaneous wind speed and direction obtained from the numerical experiments and the Timaru weather station. The REG-NOW run does a credible job of predicting wind speed, although there is about 45° difference between predicted and observed wind direction which is probably due to the coarse horizontal resolution of the run. The absence of ocean in the REG-NOS experiment has negligible influence on wind direction (between 0800 – 1900 NZST), but it reduces wind speed by up to 33% (~2 ms^{-1}). The negligible difference in wind direction between the two runs suggests that the local orography has a major influence on the wind at this station on fair weather days, with the sea breeze enhancing the intensity of wind. This is likely to be the case for other coastal areas around the South Island.

In the next chapter, a series of idealized two-dimensional experiments are performed in order to determine the physical mechanisms responsible for the formation of the CPB.

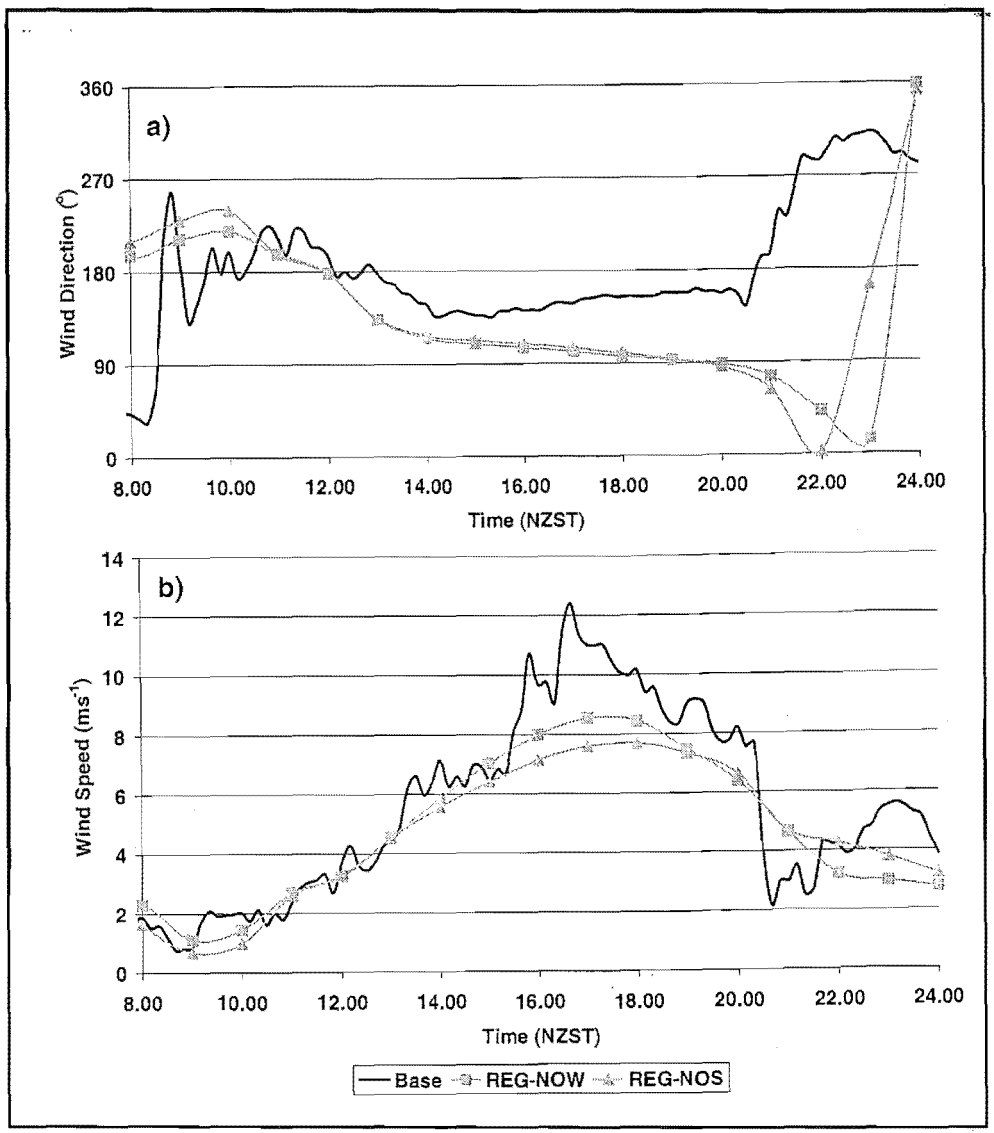

Figure 4.14: Time series of (a) wind direction, and (b) wind speed for 12th February at the Base site compared with prediction by REG-NOW and REG-NOS simulations. Note that the measured data are ten minute averages, and the modelled data are instantaneous values.

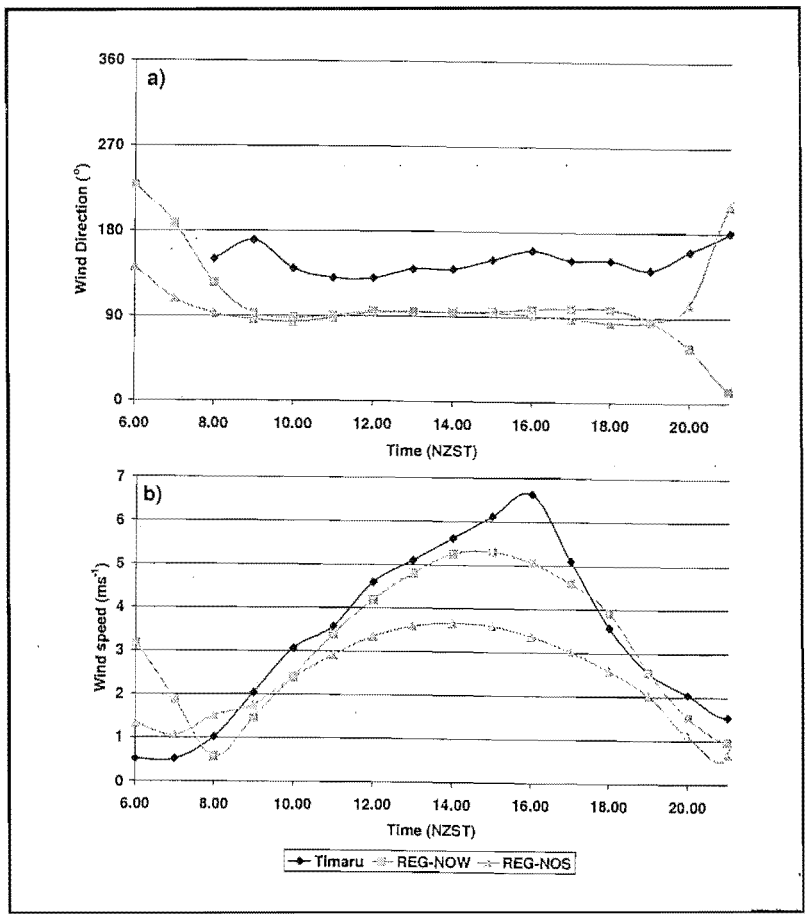

Figure 4.15: Time series of (a) wind direction, and (b) wind speed for 12th February at Timaru compared with prediction by REG-NOW and REG-NOS simulations. Note that the measured data are ten minute averages, and the modelled data are instantaneous values.

4.6 Conclusion

Results from three-dimensional simulations designed to simulate thermal forcings at the regional scale were presented in this chapter. The influence of the large scale wind field associated with synoptic weather systems and the sea breeze circulation were successively removed in each experiment. It can be concluded that the Canterbury Plains Breeze which usually dominates the surface flow in MacKenzie Basin during settled anticyclonic conditions, is a thermally induced circulation system. The horizontal scale of the thermal forcing seems to be larger than the basin, and appears to be of a regional scale. The sea breeze circulation on the Canterbury Plains does not seem to have a direct influence on the CPB, although it does change the thermal structure of the atmosphere outside the basin leading to a slight increase in the intensity of the CPB.

Chapter 5

Regional-Scale Flows: Simplified Two-Dimensional Numerical Experiments

5.1 Introduction

The objective of this chapter is to investigate the physical forcings that modify the Canterbury Plains Breeze (CPB) by performing a series of idealized two-dimensional numerical experiments with the 2-D version of RAMS. Analysis of surface data collected by several weather stations in the MacKenzie Basin and Lake Tekapo area (Chapter 2) revealed that the CPB is a recurring flow phenomenon. This circulation dominates the wind regime in the region during clear-sky, settled anticyclonic conditions in mid-afternoon in summer. Thereafter, three-dimensional numerical simulations with RAMS were conducted (Chapter 4) to provide details of the horizontal and vertical structure, and the forcing mechanisms for the CPB. Based on the numerical experiments, the conclusion was reached that the CPB (from hereinafter also referred to as a density current) is neither an intrusion of the sea breeze which develops over the Canterbury Plains, nor the topographically channelled Canterbury north-easterly. When the ocean surface was removed from the domain of the idealized three-dimensional simulation, a 1 ms^{-1} (12%) reduction in the maximum intensity of wind speed occurred inside the basin. The three-

dimensional simulations suggest the horizontal scale of the forcing to be of regional scale (> ~100 km).

In the following sections, results from twelve two-dimensional numerical experiments are presented, in which, the model is configured to simulate forcings at regional scale. The approach used is to build three simplified topography models in 2-D configuration (roughly representing an east-west cross section of the South Island through MacKenzie Basin) and analyze the thermally driven flow that is generated. This way, several forcing mechanisms are investigated for their ability to promote and influence the regional scale flow at this locality. The physical forcings investigated are due to spatial variations in:

a) landscape (land-sea contrast), resulting in sea breeze circulations
b) variation in rainfall (and hence soil moisture), resulting in inhomogeneous boundary layer development between the plains and the basin.

Two-dimensional models have been used extensively by the scientific community to study thermally and dynamically forced circulations. The models are computationally inexpensive and allow numerous sensitivity studies to be conducted in a relatively short period of time. Datasets generated by a particular run are relatively small and require less effort to analyse. Several investigators have used the two-dimensional framework to investigate thermally induced flows in complex terrain at a variety of scales. Mannouji (1982) used a hydrostatic, anelastic equation system to study the characteristic features of mountain and valley winds. As mentioned in Chapter 1, he concluded that two wind systems are produced by thermal forcings in complex terrain. A slope wind system produced by the gradient in the local topography, and a larger scale plain-plateau wind produced by regional-scale horizontal gradients in temperature, but these are also the result of gradients in topography, except at a much larger scale. His findings were corroborated by Bossert and Cotton (1994b), who used the two-dimensional configuration of RAMS to study regional-scale flows over the Colorado mountain barrier. They supported the scale separation conclusion reached by Mannouji (1982). Kimura and Kuwagata (1993) and De Wekker *et al.* (1998) performed numerical experiments to study plain-to-basin winds. An important conclusion reached by De Wekker *et al.* (1998) is the need for a horizontal temperature gradient to exist at the mountain height for

development of plain-to-basin wind systems, without the need for the mixed-layer to grow higher than the ridge. Their findings are also in agreement with Mannouji (1982).

5.2 Numerical Experiments

In a two-dimensional model framework, variations in one of the horizontal directions (most commonly the north-south) is ignored. Therefore in Equations 3 to 9 (in Chapter 3) all the terms that include $(\partial / \partial y)$ are identically equal to zero, thereby reducing the number of terms that have to be calculated, resulting in considerable reduction in computation time.

Table 5.1 provides a summary of the twelve experiments conducted for the MacKenzie Basin cross-section. A description of the topographic configurations is provided in the next section. There are three topographic configurations and four different sets of surface characteristics/forcings. For all three sets of topographic experiments, the effect of land-water contrasts generating a sea-breeze and the effect of having dryer soil on the elevated plateau (basin) are tested. From hereon, PLT, MTN and BAS designated simulations are referred to as dry runs, and the rest of the simulations are referred to as wet runs.

Table 5.1: Summary of the 2-D experiments

Name	Description	Purpose
PLT MTN BAS	Symmetric plateau Mountain and plateau Basin topography	Examine response to surface heating alone
PLTO MTNO BASO	Surrounded by ocean	Examine the influence of the ocean
PLT-M MTN-M BAS-M	Higher soil moisture on the plains	Examine the effect of variable ground wetness
PLTO-M MTNO-M BASO-M	Higher soil moisture on the plains and ocean	Examine the combined effect of the above two influences

5.2.1 Two-Dimensional Simulation Development

a) Topographic Configurations

The three topographic configurations used are illustrated in Figure 5.1. The experiments designated as PLT are the simplest representation of topography for an east-west cross section of South Island (Figure 5.1a). The plateau and the sloping terrain (~ 1.1° gradient) in the east of the domain represent MacKenzie Basin and the Canterbury Plains respectively. The "plateau" topography is symmetric, the elevated surface is 95 km wide and has a constant elevation of 760 m ASL. The "mountain" runs (MTN) add a degree of complexity to the topography by the addition of a 2000 m high mountain (Figure 5.1b) to the west of the plateau, a rough representation of the main divide (backbone of the Southern Alps). Consequently, the length of the plateau has decreased to 44 km, which is approximately the radius of MacKenzie Basin.The mountain has a half-width of 40 km and an average slope of ~ 4°. Finally, the basin characteristics are introduced to the topographic configuration by the addition of a 1200m mountain to the east of the plateau representing an approximation to the Two Thumb Range (Figure 5.1c).

Four scenarios are tested for each of the topographic configurations:

1) The PLT, MTN and BAS designated experiments (dry runs) have a soil moisture content of 15% specified for the whole land surface (this value represents percentage of total water capacity which the soil holds). The objective of these simulations is to study the effect of topography on the regional-scale circulation without the added complexity introduced by variations in boundary layer development.

2) The PLTO, MTNO, and BASO designated experiments are initialized with the same soil moisture content as in 1), except ocean surface characteristics are added to the outer domain to represent the ocean around the South Island (Figure 5.1). The sea surface temperature is specified at 16° C, and the coast is placed at 40 km

from the plateau (approximately the distance between MacKenzie Basin and the east coast of the South Island). The objective here is to investigate how the ocean around the South Island affects the development of the CPB.

3) The PLT-M, MTN-M, and BAS-M designated experiments have no ocean characteristics, but the soil moisture content has been increased to 35% outside the plateau (Figure 5.1). The purpose of these simulations is to isolate the effect of regional-scale variations in precipitation, and hence soil moisture, on the thermally induced circulation system. As previously mentioned, the climate of MacKenzie Basin is typical of inner montane basins of the South Island where the rain-shadow effects of the surrounding ridges result in annual precipitation rates of only 600 mm. Therefore the soil moisture content in the basin is usually lower than the surrounding plains.

4) The runs designated as PLTO-M, MTNO-M, and BASO-M will examine the combined effects of the presence of the ocean and the variability in soil moisture on the regional-scale circulation.

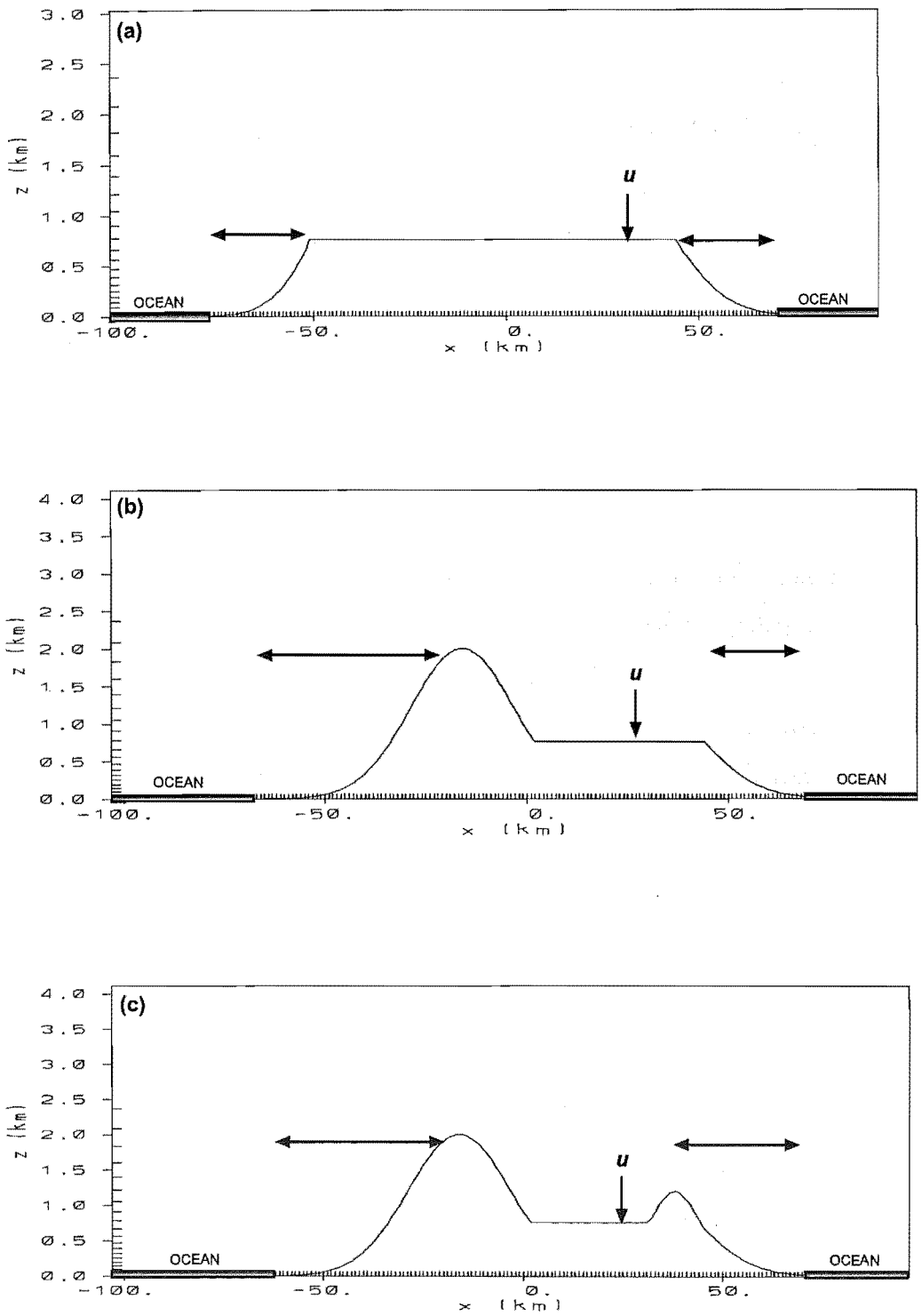

Figure 5.1: Topographic configurations used to represent the MacKenzie Basin cross-section: a) a simple plateau b) mountain plus plateau c) basin between main divide and foothills. The arrowheads indicate where wet soil was placed in the wet runs. U-component of wind velocity was extracted from position indicated with *u* over the elevated plateau.

The whole domain uses the desert parameterization as a surface characteristic (which does not take into account influences from vegetation). Results of tests (not shown in this chapter), indicate that the main features of the CBP are not affected by using different land surface characteristics (i.e. grass or irrigated crop) outside the elevated plateau. The three-dimensional simulations in the previous chapter also used the desert surface option for the whole domain.

b) Model Setup

A summary of the model setup is given in Table 5.2. Grid nesting was not used for the two-dimensional experiments. A grid spacing of 1 km was chosen for the horizontal direction, the vertical grid spacing starts at 35 m at the surface increasing with a ratio of 1.12 to 1000 m near the model top which is situated 19 km ASL. Therefore, the lowest model computational level is at about 25 m AGL, so that with this vertical resolution, 10 grid points are located within 500 m from the ground. The upper boundary is a rigid lid, and the eastern and western lateral boundaries employ the radiative condition following Klemp and Wilhelmson (1978a, b), and the northern and southern lateral boundaries use the cyclic boundary condition (as explained in Chapter 3). The cyclic boundary condition combined with the 5 north-south grid nodes effectively makes the model runs two-dimensional (Table 5.2). A damping scheme is applied to the top ten vertical layers where the amplitudes of vertically propagating gravity waves and other disturbances are gradually suppressed to reduce wave reflection from the rigid lid. Application of the damping scheme is necessary when the domain contains topography with significant variation in elevation.

Table 5.2: Summary of model setup

Number of east-west nodes	465
Number of north-south nodes	5
Number of vertical nodes	42
Δx, Δy (m)	1000
Δz (m)	35m at bottom, 1000m at top
Vertical stretch ratio	1.12
Model top (km)	19
Δt (s)	10
Soil type	Sandy loam
Vegetation type	Desert (no vegetation)
Soil moisture percentage of dry soil	15
Soil moisture percentage of wet soil	35
Coriolis force	Activated
Time differencing	Leapfrog
Radiation scheme	Longwave and shortwave (Chen and Cotton 1983)

5.2.2 Initialization

For this set of experiments, the model was initialized at 1900 NZST 11 February 1999 (0700 UTC 11 February 1999) and run continuously for a 30 hour period. The integration starts with the atmosphere at rest (initial wind field is set to zero), so that the resulting wind field is a response to terrain cooling and heating alone. The initial vertical profiles of temperature and humidity are the same as the 3-D simulations in Chapter 4. The initial soil temperature is set to 20°C for all 11 soil levels, with the deepest layer situated at 0.5m.

5.3 Simulation Results

Early Morning Profiles

Variation in topography between the three sets of experiments, results in a different thermal structure for the runs at 0600 NZST, before the surface heating takes place. The vertical temperature profiles (Figure 5.2) over the elevated terrain and the plains show that during the night an inversion layer has formed close to the surface. Surface based inversions are common features of the early morning boundary layer thermal structure during settled anticyclonic conditions. A significant difference in profiles exists between the basin experiment and the others over the elevated plateau, as the temperature profile below 1100m is cooler by about 3° over a 300m deep layer. Advective cooling is the dominant factor, as was shown by Fast *et al.* (1996). The cold air generated over the basin slopes fills the basin and is not effectively drained, as drainage only occurs when the pool height exceeds the lower ridge. With the PLT and MTN set of simulations, cold air generated by the elevated terrain and the mountain slopes can effectively drain towards lower elevations. However, over the plains, the vertical potential temperature structure for the dry runs are not significantly different. Since less cold air is drained onto the plains, the basin experiment has a slightly higher temperature for the first two vertical levels over the coastal plains (Figure 5.2). It will be shown that this difference in the thermal structure of the atmosphere before the surface heating takes place does not significantly alter the characteristics of the regional-scale circulation with the three sets of topographic configurations.

In the following sections, the daytime boundary layer development and its effect on the development of the CPB is discussed. The potential temperature and the *u*-component wind fields are presented after 17, 19 and 21 hours of integration only for the eastern half of the domain (1200, 1400, 1600 NZST respectively).

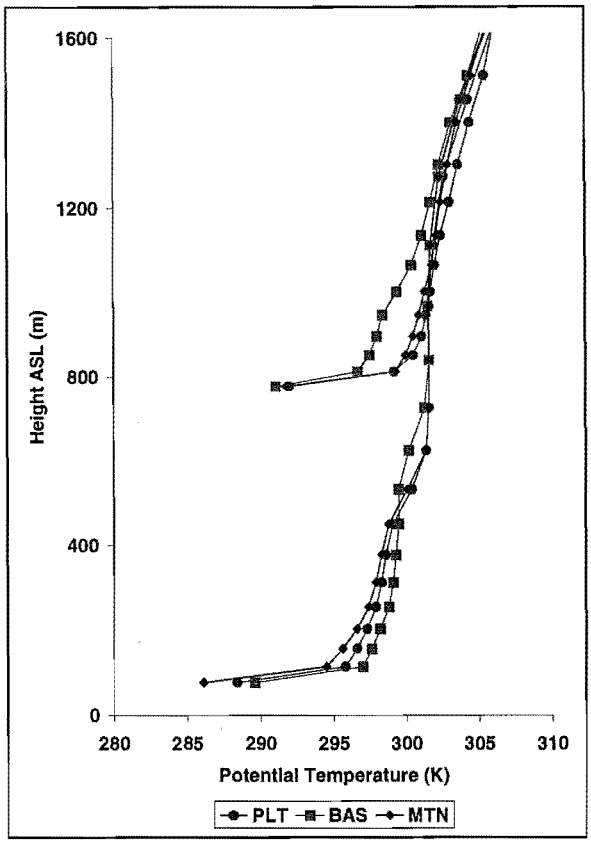

Figure 5.2: Early morning profiles (0600 NZST) after 11 hours of integration for the plateau (PLT), mountain (MTN) and basin (BAS) experiments. The profiles over the higher terrain are taken from a point in the middle of the plateau, and the profiles on the plains are taken from a point 20 km east of the eastern edge of the plateau (basin).

5.3.1 Plateau Simulations

Turbulent transfer of sensible heat from the surface caused the boundary layer to grow to a depth of approximately 700m throughout the domain by 1200 NZST (Figure 5.3a). Heating of the slope has generated an upslope circulation, and a weak easterly wind (~ 2 ms^{-1}) has developed over the plateau's edge. A baroclinic zone has formed between the air over the plateau and the air at the same elevation over the plain with a horizontal potential temperature gradient of ~2 K. The reason for this thermal contrast is that air over the elevated plateau gets heated much more quickly than air at the same elevation over the plains due to its proximity to the ground. By 1400 NZST, the boundary layer depth has increased to 1200m (Figure 5.3b), the weak easterly has encroached onto

the plateau from the eastern slope, and the gradient of potential temperature is now ~2.5 K across the baroclinic zone. The easterly continues to propagate westward at 1600 LST and has penetrated 19 km into the plateau (Figure 5.3c). As the boundary layer depth is higher than the elevation of the plateau, the differential horizontal temperature gradient across the baroclinic zone remains close to 2.5 K. This plateau circulation is similar to that simulated by Bossert and Cotton (1994b) over a plateau 3000 m high and is induced by the asymmetry of the topography at the plateau's edge. Mannouji (1982) also describes the numerical development of a similar circulation system over his 2000 m high plateau, which he termed a plain-plateau breeze.

The forcing mechanism for the development of the density current in the PLT run is analogous to sea breeze and along-valley circulations. The relatively warmer air mass over the plateau leads to a hydrostatically lower pressure over the plateau, creating a pressure gradient force directed towards the plateau, which leads to drawing relatively colder air from the atmosphere above the plains (cold air advection). The hydrostatic approximation can be written as:

$$\Delta P = g \int_{z_1}^{z_2} (\rho_2 - \rho_1)\, dz \qquad \textbf{(5-1)}$$

where ΔP is the difference between surface pressure over the plateau and pressure at the same elevation over the plains, z_1 is plateau floor height, z_2 is the height where horizontal temperature gradients diminish, ρ is the air density, and g is the gravitational acceleration. The cold air advection by the plain-to-plateau circulation results in depression of the mixed layer height over the plateau. This depression of mixed layer height due to cold air advection becomes more pronounced in the subsequent runs.

Therefore, the primary forcing for the density current generated by the PLT run seems to be the regional-scale differential heating of air due to proximity to the ground.

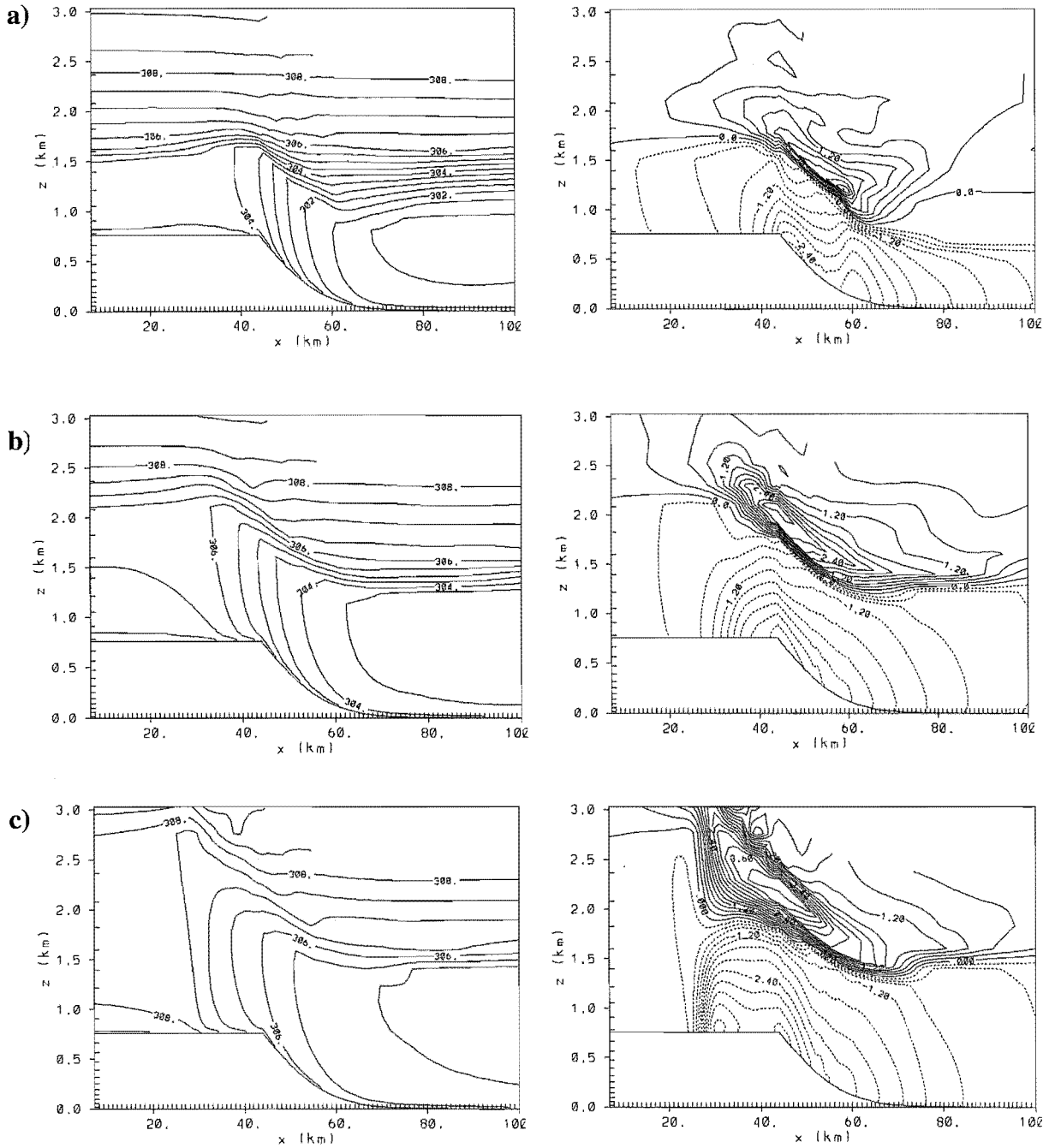

Figure 5.3: Simulated *u*-component wind isopleths (ms^{-1}) on the right and the potential temperature field (K) on the left for the plateau experiment (PLT) at a) 1200, b) 1400, c) 1600 NZST. Dashed isopleths indicate negative *u*-component (winds blowing from right to left). Contour interval is 0.5 K for the potential temperature fields, and 0.3 ms^{-1} for the isopleths.

The addition of ocean surface to the domain has a significant impact on the development of the density current for the PLTO experiment. At 1200 NZST there is a difference in boundary layer development over the Canterbury Plains (Figure 5.4a) due to a westward propagating sea breeze circulation that has been generated. Behind the sea-breeze front, the propagating marine air has caused the formation of the coastal mixed layer. The cold air advection and the subsidence induced by the return flow result in a decrease of the mixed-layer depth towards the coast. This depression of the mixed-layer height was also noted by Anthes (1978) and Lu and Turco (1994) with their two-dimensional experiments. The boundary layer temperature structure close to the plateau is not affected by the sea breeze at this time, so that the CPB still has the same characteristics as the PLT run. It is apparent that the sea breeze and the CPB are two different circulation systems, generated by different physical forcings. This fact is highlighted at 1400 NZST (Figure 5.4b), when the sea breeze front is about 18 km from the plateau's edge (propagating westward at a speed of 6.4 ms^{-1}), while at the same time, a plain-to-plateau circulation with a wind speed of about 3.2 ms^{-1} is blowing over the plateau. The front of the current has penetrated 10 km into the plateau. The mixed-layer depth has increased to 1200m over the plateau (similar to the PLT run), and the development of the boundary layer over the plains still remains restricted due to the cold air advection associated with the sea breeze. As a result, the horizontal temperature gradient across the baroclinic zone is ~4.5 K. The 1600 NZST (Figure 5.4c) fields show evidence of a well developed CPB current with an intensity of 6.0 ms^{-1} over the plateau which has propagated about 26 km to the west, while the horizontal temperature gradient has increased to ~5.5 K. This experiment suggests that sea-breeze formation on the Canterbury coast due to land-sea temperature contrasts has an indirect impact on the CPB over the plateau. By depressing the boundary layer height over the plains, the sea-breeze increases the horizontal temperature gradient at the regional-scale, intensifying the CPB as a result.

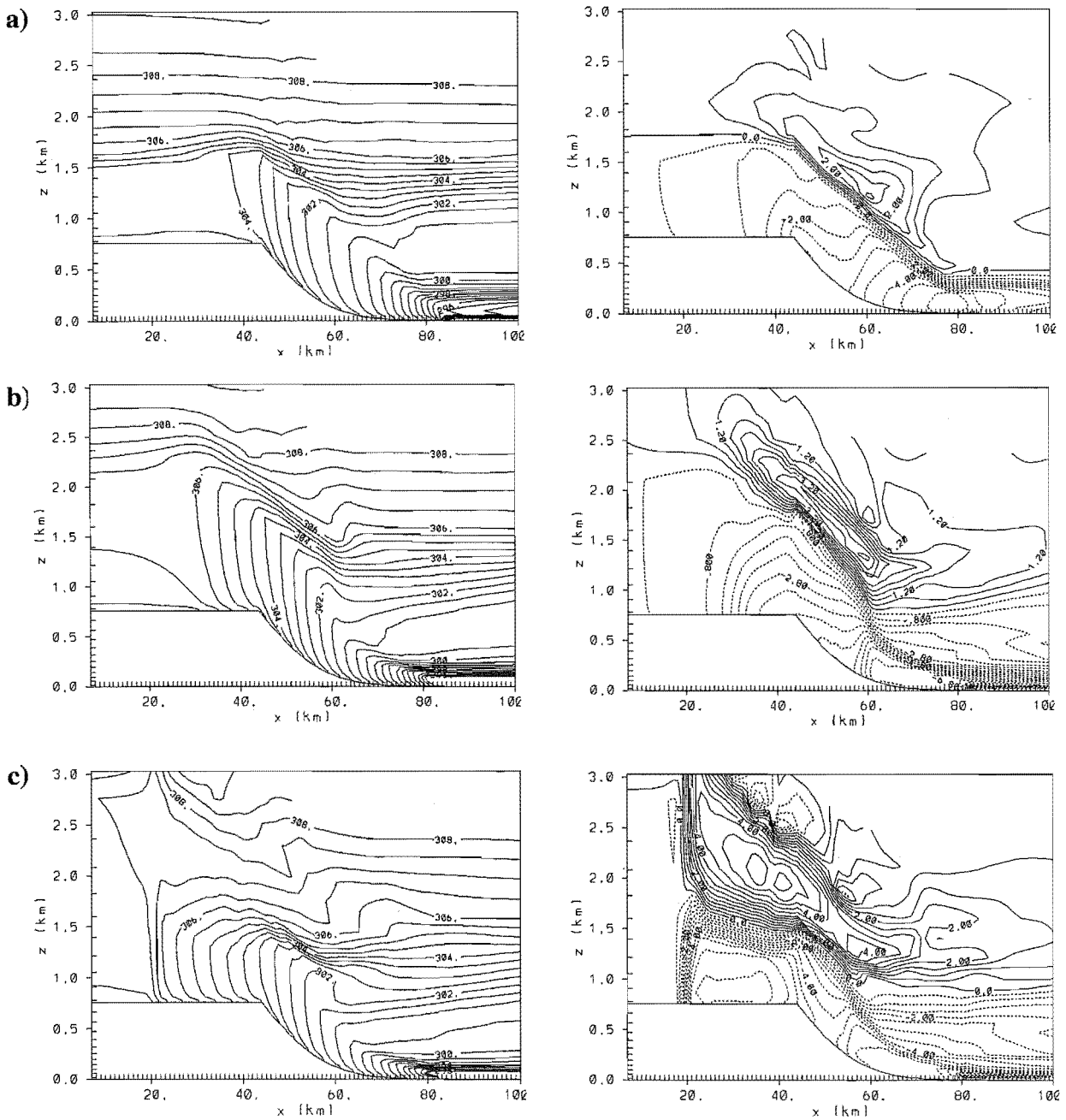

Figure 5.4: Simulated *u*-component wind isopleths (ms^{-1}) on the right and the potential temperature field (K) on the left for the plateau with the ocean experiment (PLTO) at a) 1200, b) 1400, c) 1600 NZST. Dashed isopleths indicate negative *u*-component (winds blowing from right to left). Contour interval is 0.5 K for the potential temperature fields, and 0.5 ms^{-1} for the isopleths.

Variation in soil moisture content also has a dramatic impact on the development of the CPB (PLT-M experiments). At 1200 NZST (Figure 5.5a), mixed-layer over the plains has only grown to a depth of 400 m compared with the depth of 800m over the plateau. Already, a differential horizontal temperature gradient of ~3 K exists across the baroclinic zone. An understanding of soil moisture effects on boundary layer growth can be gained by examining the surface energy balance equation which controls the turbulent transfer of heat from the surface. In simple form it can be written as:

$$Q^* = Q_E + Q_H + Q_G \tag{5-2}$$

where Q^* is the net radiation, Q_H the sensible heat flux, Q_E the latent heat flux, and Q_G the heat flux into/out of the soil. The sensible (Q_H) and latent (Q_E) heat flux terms can be expanded into:

$$\begin{aligned} Q_H &= \rho\ C_P\ C_d\ u\ (T_s - T_a) \\ Q_E &= \rho\ \ L\ \ C_d\ u\ (q_s - q_a) \end{aligned} \tag{5-3}$$

where ρ is the air density, C_p is the heat capacity of air at constant pressure, C_d is the drag coefficient, u is the wind speed close to surface, T_s is surface temperature, T_a is air temperature close to the surface, L is the latent heat of vaporization, q_s is the surface mixing ratio, and q_a is the mixing ratio of air close to the surface. When the soil contains more moisture, q_s will be greatly increased leading to partitioning of more of the net radiation into latent heat. The reduction of sensible heat flux results in a cooler and hence more shallow boundary layer over the more moist plains.

Similar to the PLT run, the mixed-layer depth over the plateau has grown to a depth of 1200 m by 1400NZST (Figure 5.5b), whereas it has only grown to a depth of about 500 m over the plains. With the increase of the horizontal temperature gradient to ~ 6 K, the CPB has intensified to 4 ms^{-1}, and has penetrated 20 km into the plateau. At 1600 NZST (Figures 5.5c), the mixed layer has grown to a height of 1 km over the plains, although it is 4 K colder than the mixed layer simulated by the PLT run. Cold air advection due to CPB has depressed the mixed layer development over the plateau, while the easterly wind is blowing with an intensity of 6 ms^{-1}. The current has penetrated 30 km into the plateau, which is 5 km further than the PLTO run.

The characteristic features of the CPB are the same for the PLTO-M sets of experiments (Figure 5.6). Since the higher soil moisture over the plains has resulted in a reduced sensible heat flux near the coast, the sea-breeze circulation is not as vigorous as the PLTO run (Figure 5.6a, b, c). The combined effect of a reduced sensible heat flux due to higher soil moisture and the cold air advection by the sea breeze, lead to a very shallow boundary layer height over the coastal plain slopes for this run.

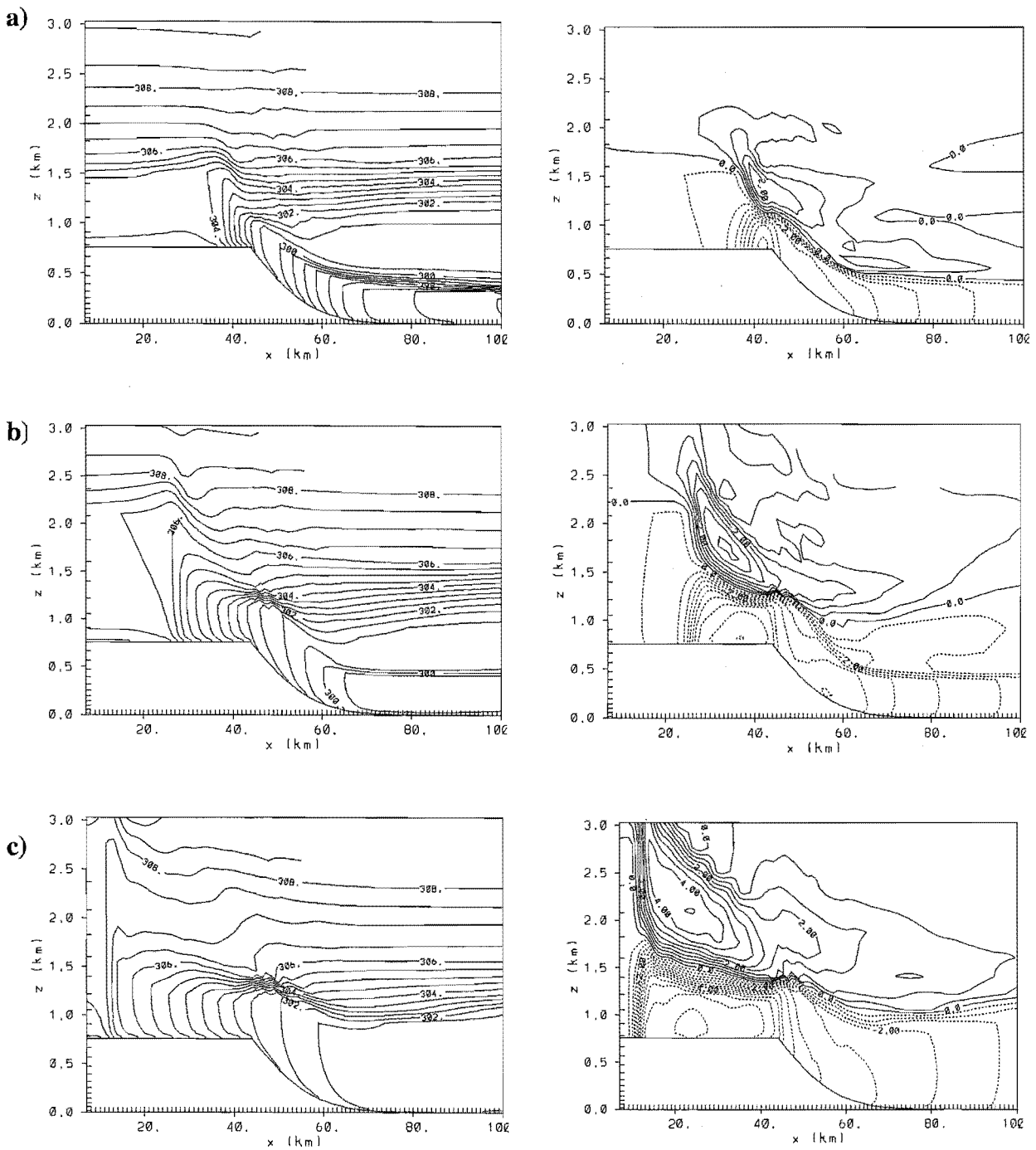

Figure 5.5: As in Fig. 5.3 but for PLT-M experiment.

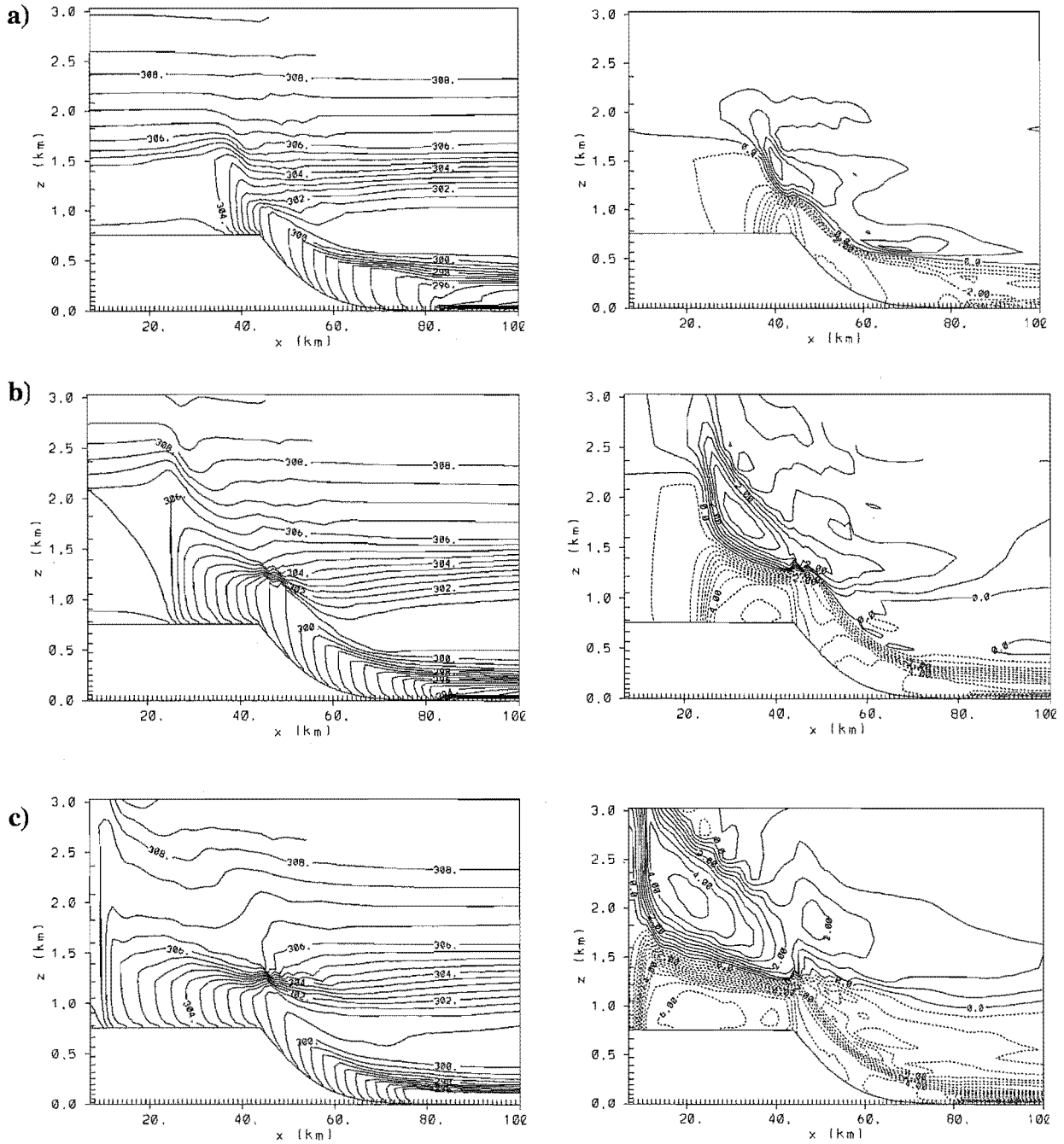

Figure 5.6: As in Fig. 5.3 but for PLTO-M.

5.3.2 Mountain Simulations

In this section, the interaction of the CPB with the plain-to-mountain wind (Whiteman 2000) is investigated. The interaction of mountain flows and sea breezes were first studied numerically by Mahrer and Pielke (1977). They represent the closest situation to that observed in MacKenzie Basin. Mahrer and Pielke (1977) found that the circulations combined to produce more intense flows during the day. Lu and Turco (1994), found that the coupling of flows is a function of:

a) the mountain height influencing the sea breeze
b) the distance of the land-sea discontinuity from the mountain
c) the vertical temperature profile of the atmosphere.

It is therefore of interest to find out if the Southern Alps have a similar influence on the development of the CPB.

At 1200 NZST, the boundary layer thermal structure over the plains generated by this run is very similar to that of the PLT simulation (Figure 5.7a). Heating of the slopes has generated a symmetric upslope circulation on both sides of the 2000 m mountain (Figures 5.7a, only the eastern slopes shown). This upslope circulation is similar to the simulation made by Mahrer and Pielke (1977) over a 900 m mountain. Due to the horizontal pressure gradient caused by the mountain, a weak easterly flow has already been generated over the plateau (Figure 5.7a), while an easterly flow is also evident at the plateau's edge similar to the PLT run. The density current is well developed by 1400 NZST with an intensity of 3.2 ms^{-1}, and has propagated about 20 km into the plateau (Figure 5.7b). In this experiment, the mountain wind and the CPB circulations are not coupled, suggesting the forcings that induce each flow are quite distinct. By 1600 NZST (Figure 5.7c), the whole plateau is dominated by an easterly flow with an intensity of ~3.5 ms^{-1}. Therefore for this dry run, the characteristic features of the CPB circulation were unaffected, except that the flow is intruding into a weak dominant easterly flow setup by the presence of the mountain.

Results for the MTNO, MTN-M, and MTNO-M are illustrated in Figures 5.8, 5.9, and 5.10 respectively. The characteristics of the boundary layer development over the plains remains the same as the plateau simulations, and the characteristic features of the CPB are also unaffected by the presence of the mountain. This suggests that for the terrain configuration of the two-dimensional experiments, the mountain is so far from the plateau's edge (the source region for the CPB) that it does not significantly interfere with its development. The reduction in mixed layer growth and thermal structure over the plains due to cold air advection by the sea breeze, and the high soil moisture content still have the most influence on the strength of the CPB.

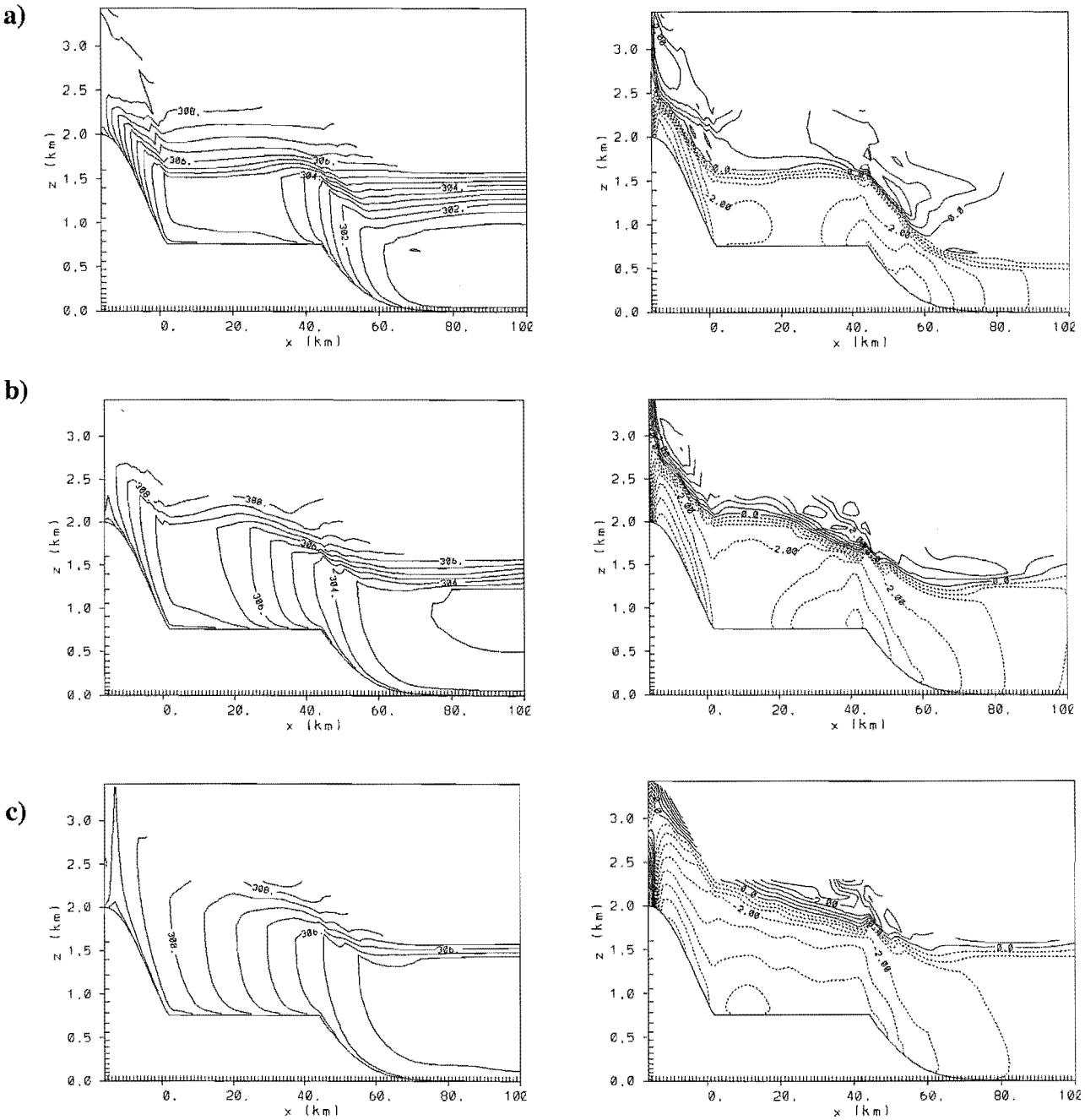

Figure 5.7: Simulated *u*-component wind isopleths (ms^{-1}) on the right and the potential temperature field (K) on the left for the mountain experiment (MTN) at a) 1200, b) 1400, c) 1600 NZST. Dashed isopleths indicate negative *u*-component (winds blowing from right to left). Contour interval is 0.5 K for the potential temperature fields, and 0.5 ms^{-1} for the isopleths.

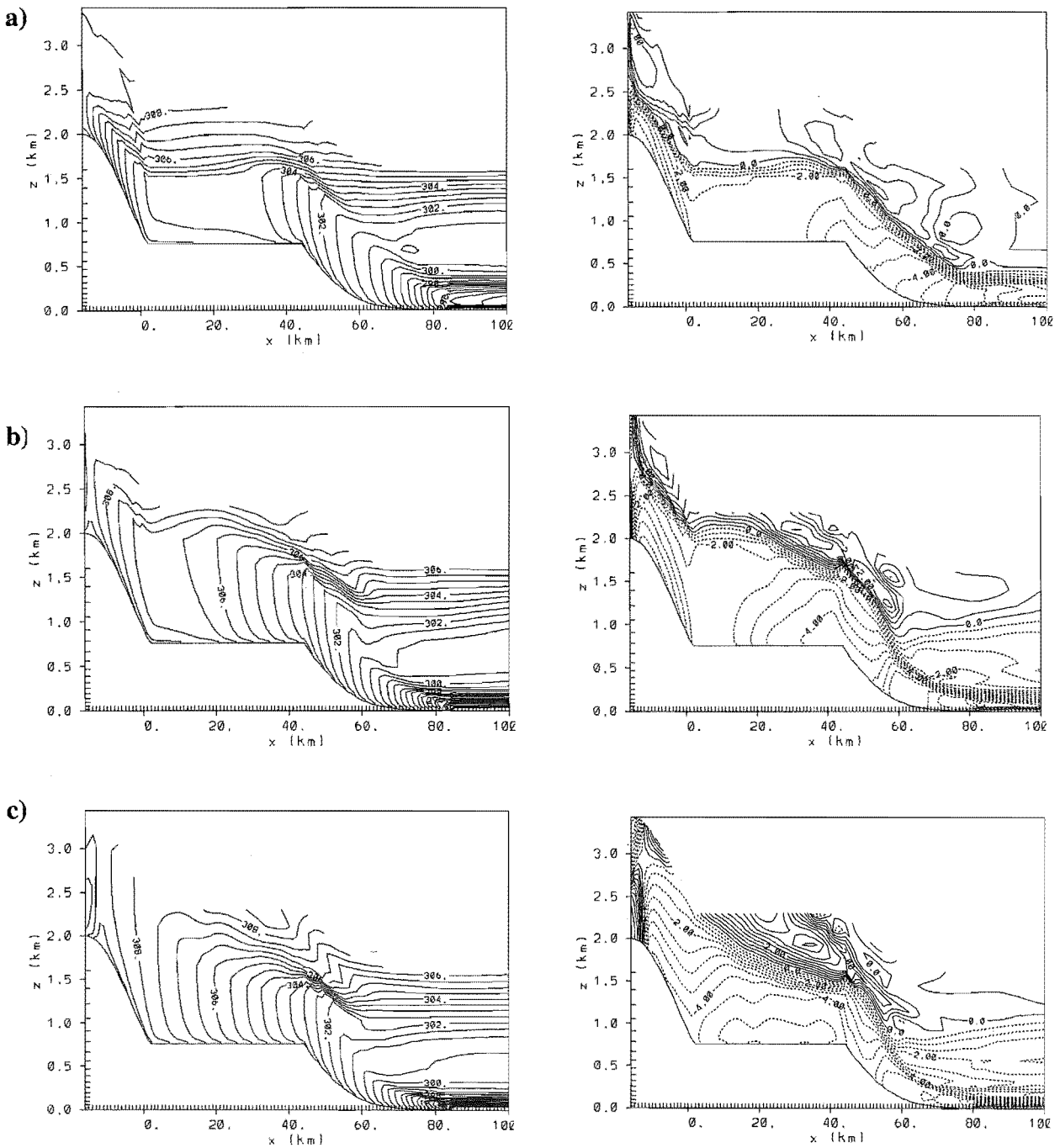

Figure 5.8: As in Fig. 5.7 but for MTNO.

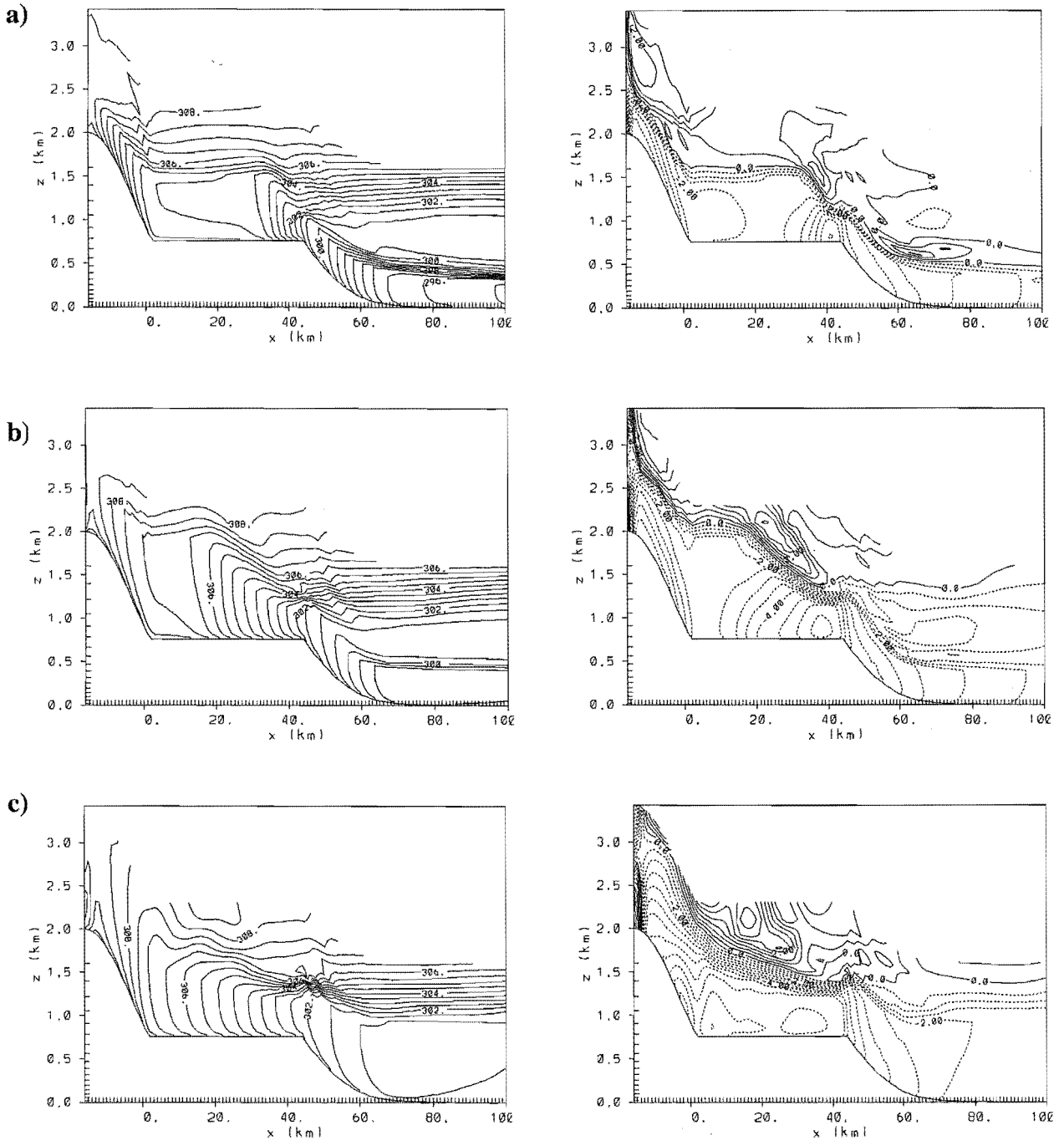

Figure 5.9: As in Fig. 5.7 but for MTN-M.

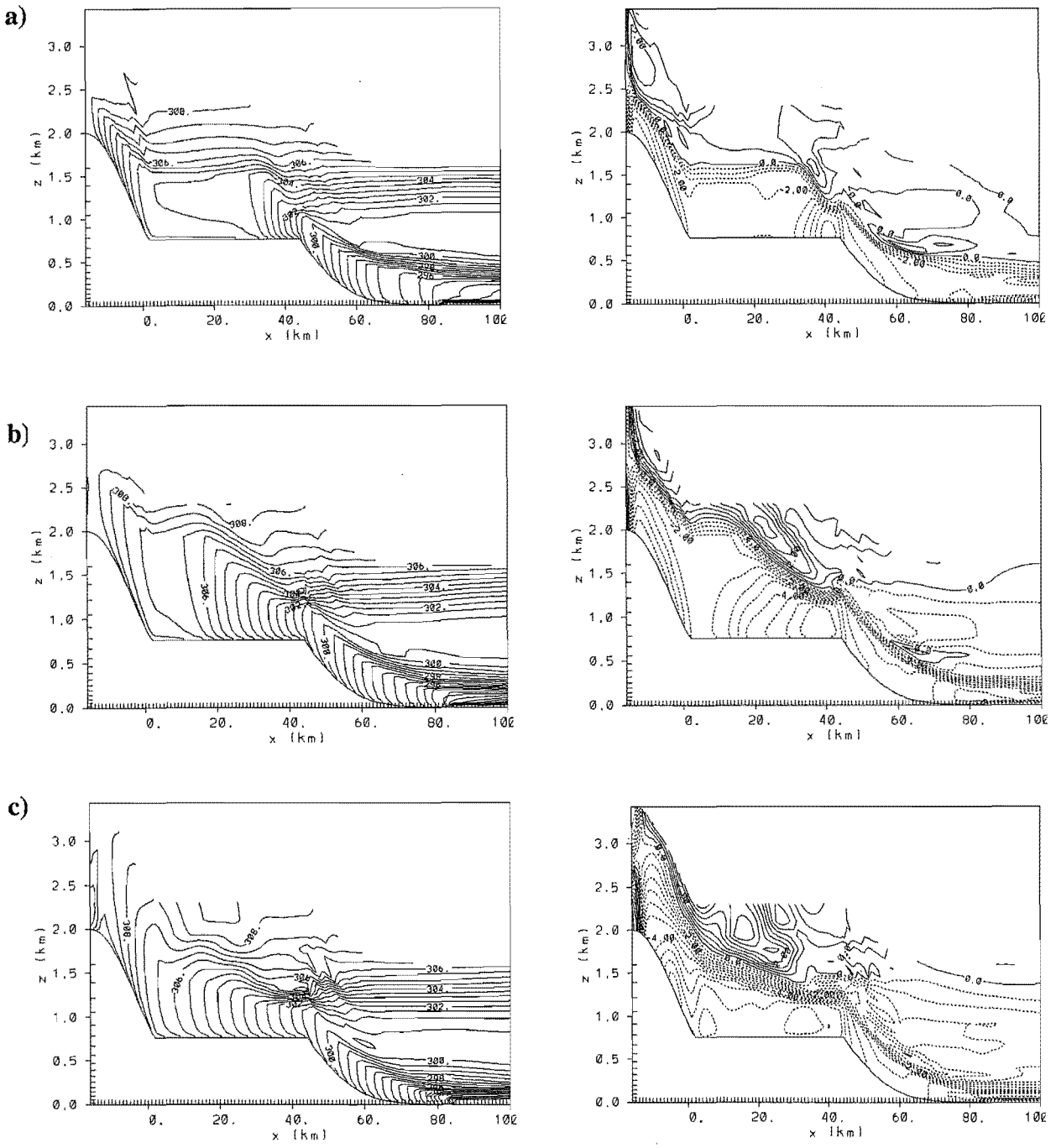

Figure 5.10: As in Fig. 5.7 but for MTNO-M

5.3.3 Basin Simulations

Thermally induced flows that transport air into basins have been called plain-to-basin winds. De Wekker *et al.* (1998) performed a series of two-dimensional experiments with the same version of RAMS used here, to numerically study the characteristics of this particular circulation. Several important differences exist between their simulations and the ones presented in this section. Although they used a variety of topographic configurations, their basin were always symmetrical (both ridges always had the same elevation). They also did not investigate the influences of inhomogeneous soil properties, or the coastal influences on the plain-to-basin circulation. De Wekker *et al.* (1998) concluded that the plain-to-basin wind:

a) intrudes into the basin after the cessation of upslope winds on the basin side slope, when the surface sensible heat flux changes sign

b) the intrusion time does not significantly vary in response to changes in the basin configuration.

In this study, it was found that in the "basin" experiment (designated as BAS), the boundary layer thermal structure develops the same way as the previous set of dry runs (Figure 5.11). Heating of the slopes of the 1200 m mountain on the eastern side of the basin has generated upslope winds on both sides of the ridge (Figure 5.11a). However, because of the horizontal temperature gradients across the ridge, the easterly upslope flow is beginning to overwhelm the westerly flow generated by the shorter western slope at this stage. As a comparison, since the horizontal thermal structure remains roughly symmetric around the 2000 m ridge, the upslope flows on both sides of the ridge converge at the top (Figures 5.7a, b, c). By 1400 NZST, the density current has overwhelmed the upslope flow on the basin side and is propagating down the slope with a wind speed of 3.2 ms^{-1}. The intrusion is occurring three hours before the surface sensible heat flux changes sign. Hence, it seems the asymmetric basin topography (unequal ridge heights) has a significant impact on the intrusion time of the CPB (plain-to-basin wind).

Figure 5.12 shows the results from the introduction of ocean to the domain (BASO). As before, sea breeze front is evident over the plains by 1400 NZST (Figure

5.12b). Similar to the basin run, there is a slight intrusion of the density current onto the basin side slope, with an intensity of 2 ms^{-1}. By 1600 NZST (Figure 5.12c), the CPB has propagated westward 5 km further than the dry run, since there is a slight increase of 1 ms^{-1} in its wind speed (Figure 5.12c).

Figures 5.13 and 5.14 show the results from BAS-M and BASO-M simulations respectively. There is no significant difference between the thermal structure of the boundary layer over the plains above the plateau height between these two experiments. This leads to the development of a similar plain-to-basin circulation system in these two runs. As before, the existing inversion layer above plateau height in not eroded because of the prevention of mixed layer growth due to cold air advection by the sea breeze and/or decrease in sensible heat flux from the surface due to high moisture content of the soil.

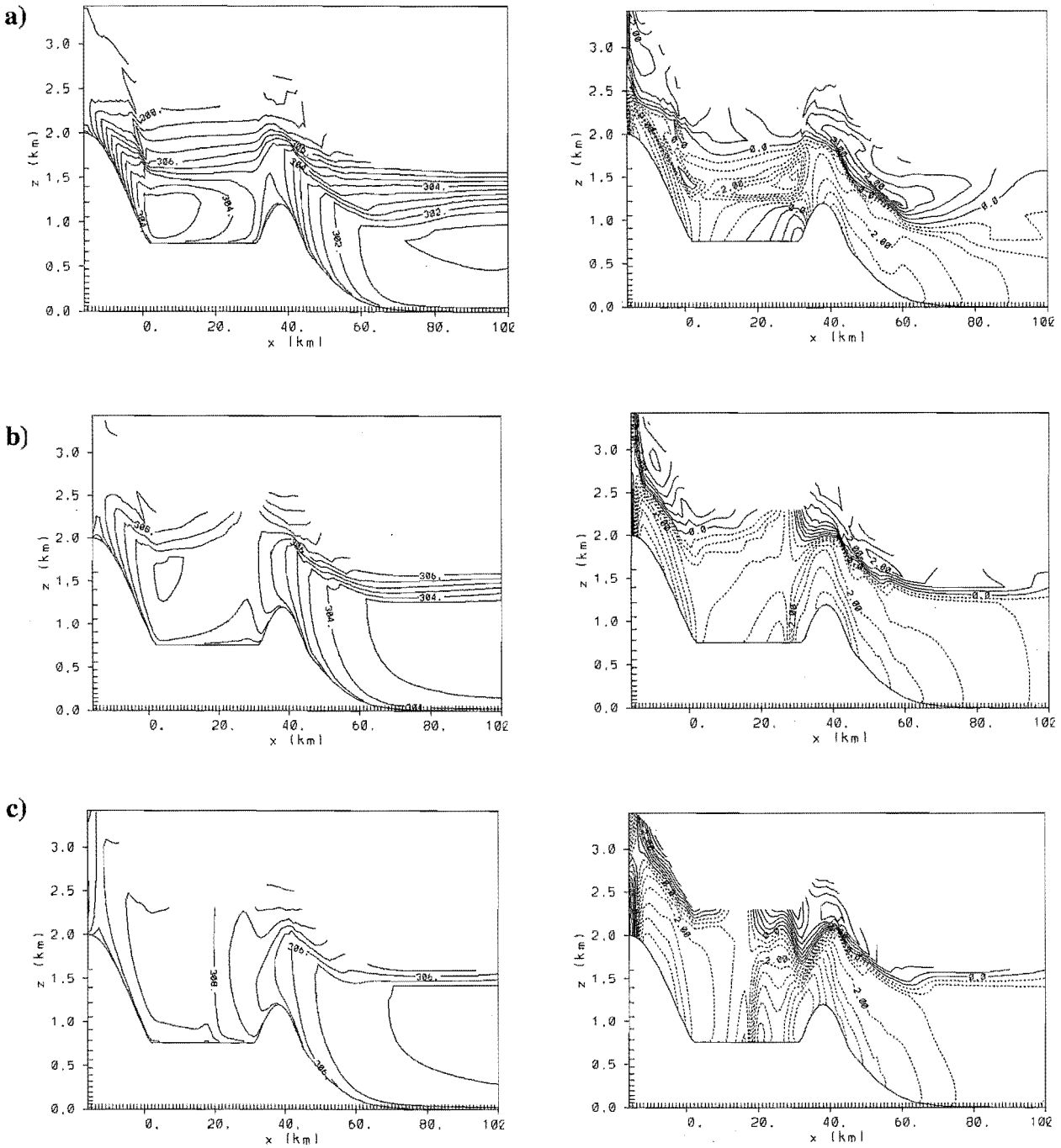

Figure 5.11: Simulated *u*-component wind isopleths (ms^{-1}) on the right and the potential temperature field (K) on the left for the basin experiment (BAS) at a) 1200, b) 1400, c) 1600 NZST. Dashed isopleths indicate negative *u*-component (winds blowing from right to left). Contour interval is 0.5 K for the potential temperature fields, and 0.5 ms^{-1} for the isopleths.

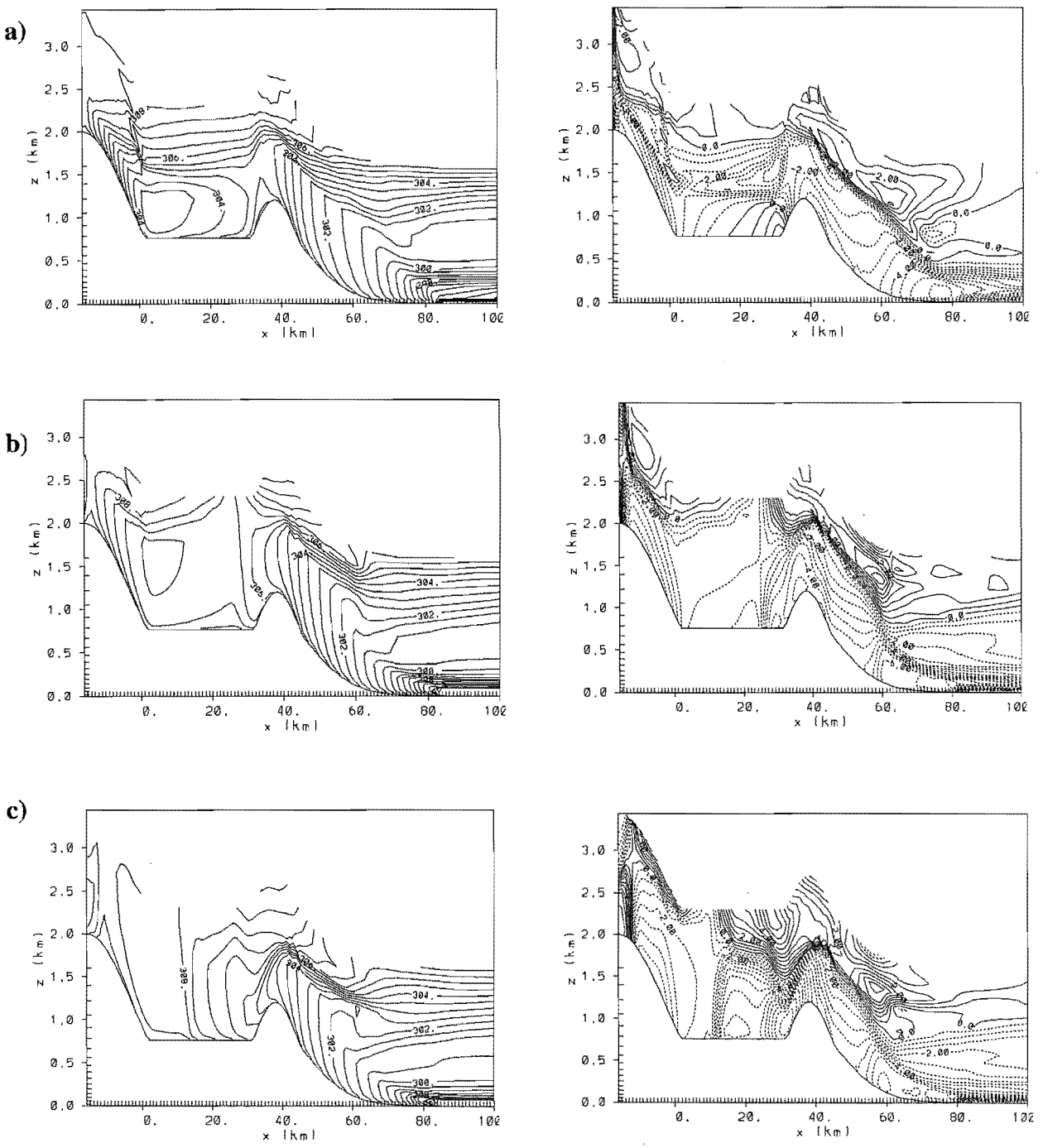

Figure 5.12: As in Fig.5.11 but for BASO.

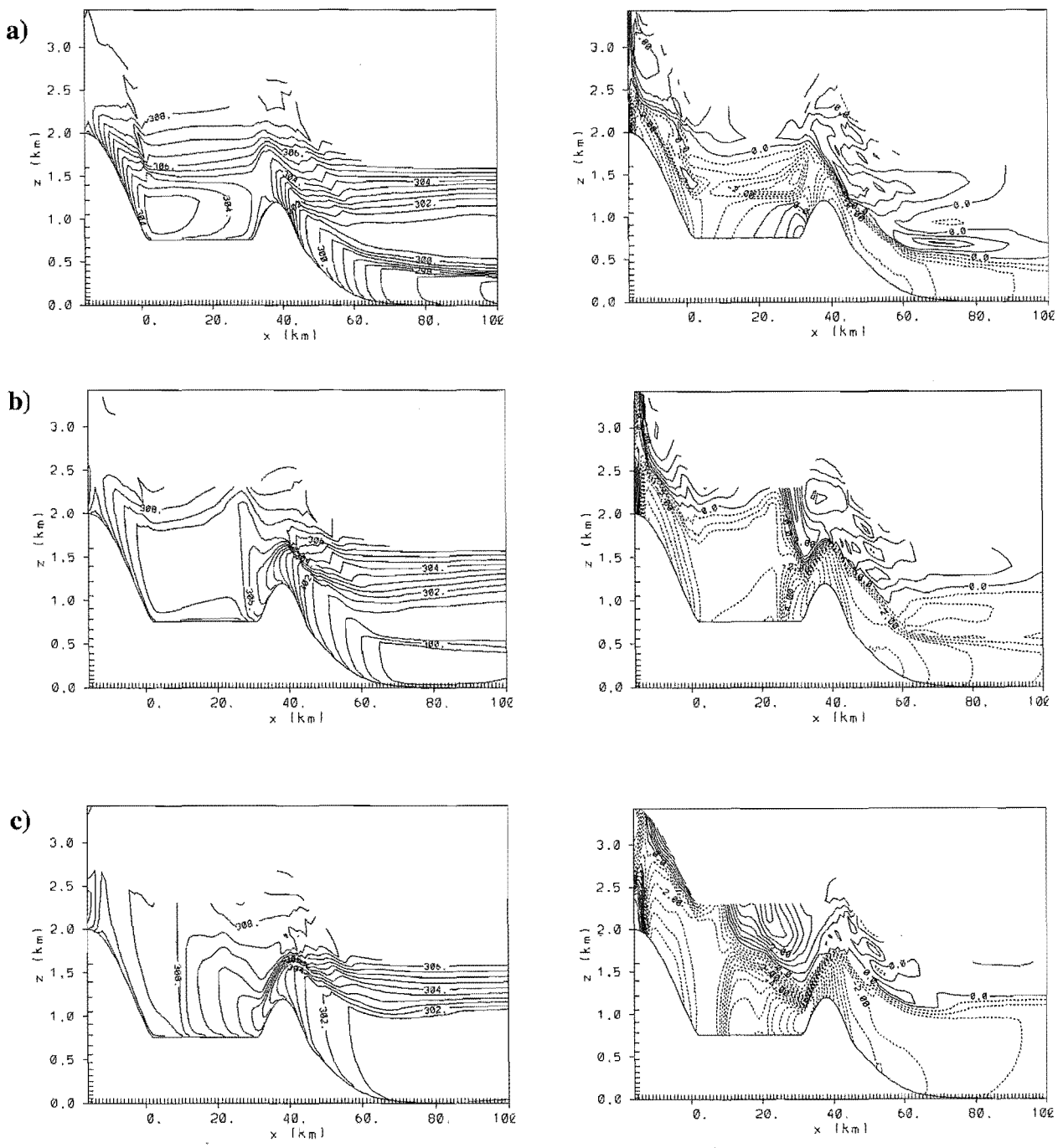

Figure 5.13: As in Fig. 5.11 but for BAS-M.

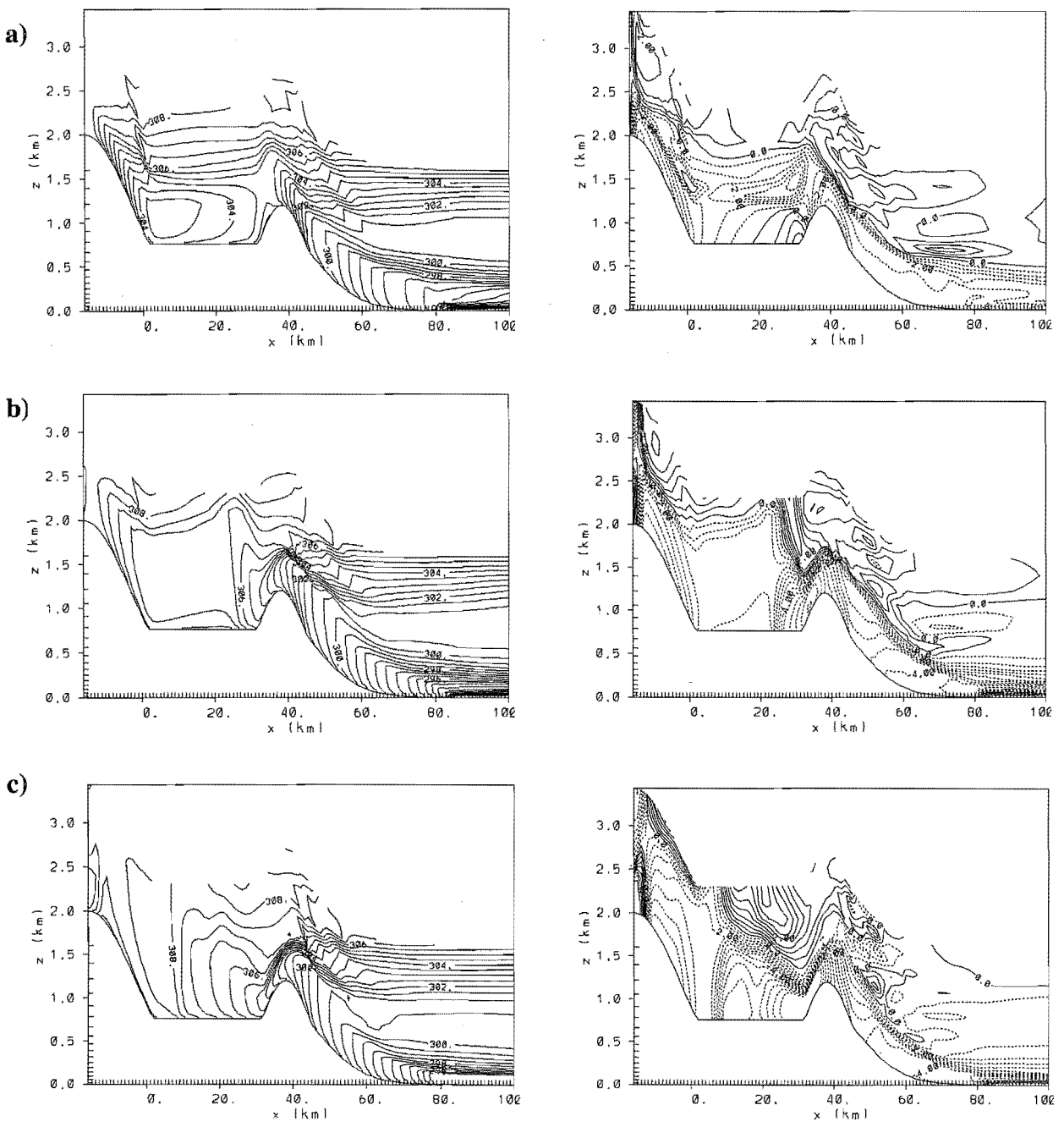

Figure 5.14: As in Fig. 5.11 but for BASO-M.

5.4 Discussion of Results

In the previous sections, results from the two-dimensional experiments were presented. It was shown that the CPB is primarily forced by the horizontal temperature gradient between the air over the elevated plateau (representing MacKenzie Basin) and the air at the same elevation over the plains (representing the Canterbury Plains). However, forcings that increase this temperature gradient (such as cold air advection by the sea breeze or higher soil moisture over the plains) can influence the intensity of the CPB by about 2 ms^{-1}.

Time series for the *u*-component of wind from a grid point on the plateau (indicated by an arrow in Figure 5.1) extracted from the lowest computational level (25 m AGL) is presented in Figure 5.15 for all twelve experiments. This grid point is chosen to be representative for the location for the base station AWS mentioned in Chapter 2. For the plateau experiments, while the maximum intensity of wind increases by 2 ms^{-1} between the dry and the wet runs (Figure 5.15a), the difference between the wet runs is negligible. However, there is a significant difference in the onset of the breeze at this location between the runs. When a higher soil moisture content over the plains is specified (PLTM experiment), the CPB was detected at this location 3 hours earlier than the dry run. For this topographic configuration, the difference in soil moisture (and hence the boundary layer development over the plains) seems to have the strongest influence on the intensity of the circulation.

Since the mountain range had already set up an easterly current over the plateau, the intrusion of the CPB into the elevated plateau was not as well defined with the MTN experiments (Figure 5.15b). There is negligible difference in the maximum intensity of the wind between this series of runs and the PLT experiments, suggesting that the Alps do not modify forcing of the CPB at this range.

The CPB is detected at about 1400 NZST at this location for all scenarios for the basin experiments (Figure 5.15c). The difference being that the horizontal temperature gradients have to be strong enough across the eastern ridge, so that the density current can overwhelm the upslope flows opposing it from the basin side before propagating

westward. The difference in maximum intensity of the wind between the dry and wet runs is about 2 ms^{-1} (the same as other two sets of runs), although there is little difference between the BAS-M and BASO-M. This reinforces the conclusion that the ocean has an insignificant forcing affect on the CPB.

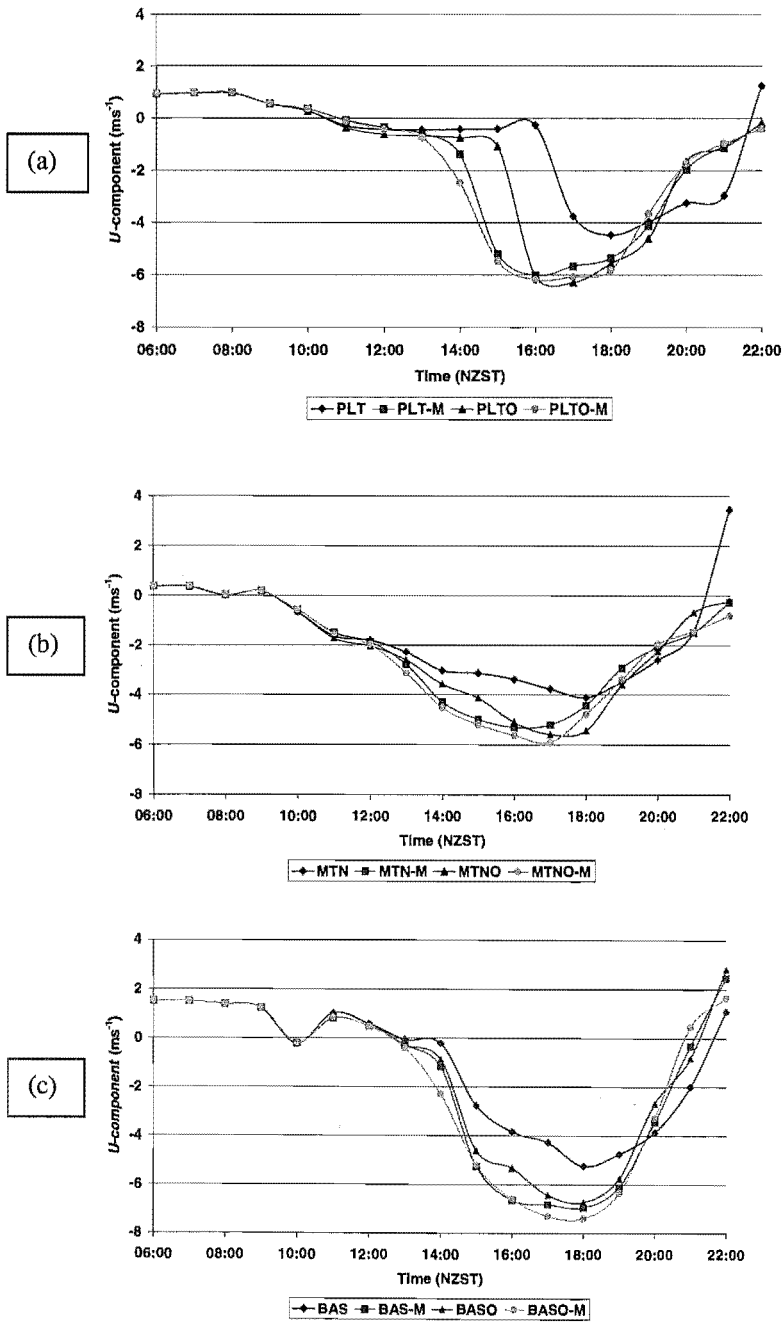

Figure 5.15: Time series of surface *u*-component wind at grid point over the plateau for the a) plateau, b) mountain, and c) basin simulations.

5.5 Conclusion

Twelve two-dimensional numerical experiments were performed to confirm the results from the previous chapter which suggested that the Canterbury Plains Breeze (CPB) is a regional-scale circulation generated by the horizontal temperature gradient between the air over the basin and the air at the same level over the Canterbury Plains. The numerical simulations show that the CPB is greatly modified by the basin topography and the difference in land surface characteristics between the basin and the plains. Variation of land surface characteristics influences the intensity of this density current by up to 2 ms^{-1}. With the three-dimensional runs, this difference was ~ 1 ms^{-1}. It has to be pointed out that the two-dimensional runs cannot simulate the venturi effect that the mountain passes, such as Burke Pass, have on the CPB. These were simulated quite clearly by the three-dimensional runs described in Chapter 4.

Chapter 6

Numerical Simulations of Local and Regional Scale Flows in the Lake Tekapo Region

6.1 Introduction

In the previous two Chapters, results from a series of two- and three- dimensional numerical experiments were presented in order to investigate the forcing mechanisms for the Canterbury Plains Breeze. This regionally induced thermal circulation is the dominant wind system in the MacKenzie Basin and Lake Tekapo region early in the afternoon on fair weather days. However, before the intrusion of the CPB into the region, locally generated thermal flows such as the lake breeze and daytime mountain winds (upslope and up-valley winds) are observed. These features were not simulated in the previous chapters due to the rather coarse horizontal resolution of the model runs. For the simulations in this chapter, RAMS was configured to represent forcings at smaller scales in order to investigate the interaction between regionally and locally induced thermal circulations in the vicinity of Lake Tekapo.

The objectives of this chapter are:

- to investigate the effect of Lake Tekapo on the simulated surface flow pattern
- to investigate the interaction between the CPB and locally generated flow systems

Table 6.1: Summary of 3-D simulations conducted to examine the influence of Lake Tekapo on local and regional winds.

Name	Description
LOC-LAKE	Lake Tekapo present
LOC-LAND	Lake Tekapo absent

6.2 Numerical Experiments

Similar to the regional scale simulations of Chapter 4, the case study day chosen for numerical experiments was 12 February, 1999. Two numerical experiments were conducted, the model run designated as LOC-LAKE had a representation of Lake Tekapo in its domain, while in the LOC-LAND run, the lake was removed (Table 6.1).

6.2.1 Three-Dimensional Simulation Development

a) Grid Structure

Like the model runs in Chapter 4, grid-nesting capability of RAMS is used for the horizontal direction only. Table 6.2 provides a summary for each nested grid. Numerical experiments in this chapter use four grids: the coarse grid covering the South Island has a 9.6 km horizontal resolution, the first nested grid (grid 2) has a horizontal resolution of 2.4 km covering the middle third of the South Island (Figure 6.1). The second nested grid (grid 3) has a horizontal resolution of 800 m, covering a rectangular shaped domain including the Lake Tekapo catchment area to the north and Burke Pass to the south (Figure 6.2). The third nested grid (grid 4) has a horizontal resolution of 267 m covering Lake Tekapo, and the Godley and Macaulay valleys. Grids 1 and 2 are centered at 170.4 ° W and 44°S, while grids 3 and 4 are centered at 170.6 ° W and 43.8°S. The four grids consist of 65, 62, 59 and 83 zonal, and 65, 62, 110 and 152 meridional grid cells respectively (Table 6.2). Vertical grid structure is the same as the three-dimensional model runs of Chapter 4.

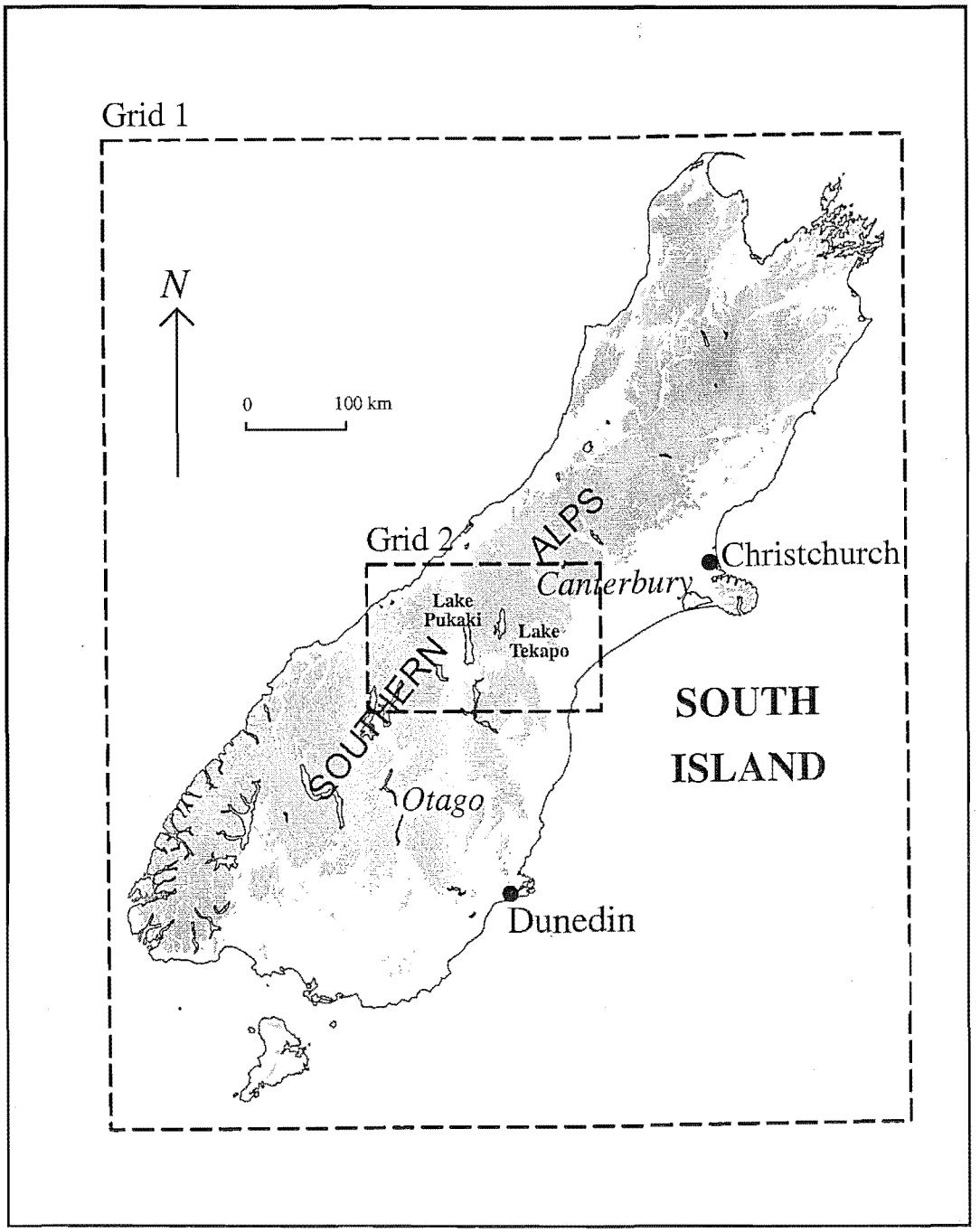

Figure 6.1: Geographic locations of grids 1 and 2 in the LOC-LAKE and LOC-LAND simulations.

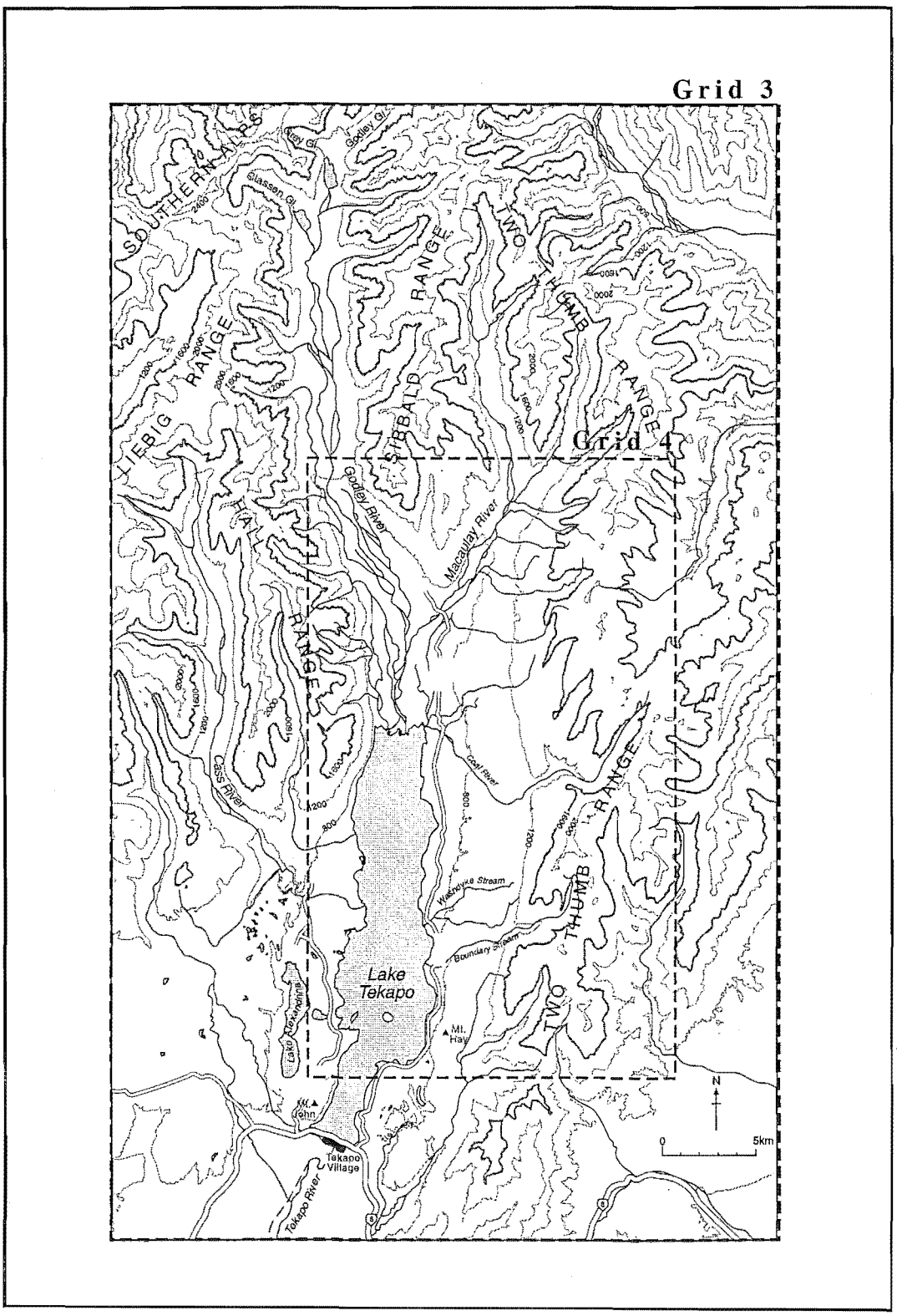

Figure 6.2: Geographic locations of grids 3 and 4 in the LOC-LAKE and LOC-LAND simulations.

Due to the high spatial resolution of the numerical experiments and the complexity of the terrain, a great deal of consideration had to be given to the selection of each

parameter. A nesting ratio of 1:4 was selected only between grids 1 and 2, with 1:3 selected between grids 2 and 3, and grids 3 and 4. Ratios higher than this were not numerically stable. In addition, nesting ratios higher than 3 are not recommended in areas with complex terrain, since features of larger-scale flow may not be represented on the finer grid properly (Doran and Skyllingstad 1992).

Table 6.2: Characteristics of the grids

	Grid 1	Grid 2	Grid 3	Grid 4
Number of east-west nodes	65	62	59	83
Number of north-south nodes	65	62	110	152
Number of vertical nodes	32	32	32	32
Δx, Δy (km)	9.6	2.4	0.8	0.267
East-west width (km)	614.4	146.4	46.4	21.9
North-south width (km)	614.4	146.4	87.2	40.3
Δz at first level (m)	50	50	50	50
Vertical stretch ratio	1.12	1.12	1.12	1.12
Grid top (km)	12	12	12	12
Δt (s)	30	10	3.3	0.83

Topography for all grids is derived from the 30-second (about 1 km) United States Geological Survey (USGS) terrain dataset. Visual examination of interpolated grids 3 and 4 topography indicate that the major features of the landscape are satisfactorily represented on these high resolution grids. Approximately 17 horizontal nodes span the width of Lake Tekapo, so that the lake is well resolved and the model should be able to produce thermally induced circulations resulting from lake-land contrasts.

b) Model Setup

A summary of model setup is provided in Table 6.3. Similar to the regional scale simulations in Chapter 4, surface characteristics are specified homogeneously for the entire domain. However, since the main focus of this chapter is in representing forcings in the MacKenzie Basin and Lake Tekapo region, a lower soil moisture content of 15% (which is representative of the Base site only) is specified (Oliphant 2000). Because of the high horizontal resolution of grid 4, Lake Tekapo is resolved adequately, so that its surface temperature is set to 11°C as indicated by field measurements.

Table 6.3: Summary of model setup

Soil type	Sandy loam
Vegetation type	Desert (no vegetation)
Soil moisture (% of saturation)	15
Sea Surface Temperature (°C)	16
Lake surface temperature (°C)	11
Roughness length (m)	0.05
Coriolis force	Activated
Time differencing	Hybrid
Radiation scheme	Longwave and shortwave (Chen and Cotton 1983)

6.2.2 Initialization

Temperature and humidity profiles measured by the aircraft early on the morning of 12th February 1999 were used to initialize these runs (Figure 2.8). Above 3000 m AGL where aircraft data were not available, data from the 0000 NZST Invercargill rawinsonde were blended in. Simulations were initialized on the morning of 12th February (at 0600 NZST), so that no nocturnal phase is simulated before the onset of surface heating. The reasons for the choice of initialization time were that:

a) RAMS was not numerically stable during the nocturnal simulation with the chosen parameters and grid configuration. Experimentation with different settings is possible but is exceedingly time consuming.

b) The combination of having a high number of nodes for grids 3 and 4, and the small time-steps required for numerical stability at high resolutions, meant that these runs were computationally very expensive. It took over 1 day of computation to simulate one hour on the available computer platform. The simulations presented in this chapter took over 17 days to complete, and if the nocturnal phase was included the simulations would have taken more than 25 days.

Therefore, even if a numerically stable configuration for simulating a nocturnal phase was found, it would have been highly impractical to run the model for more than 12 hours of simulation time.

To avoid initializing at 0600 NZST, experiments were made with other techniques such as Four Dimensional Data Assimilation (FDDA). For example, the model was initialized on 11th February with only 3 grids so that the model run would progress faster, and then the simulation was stopped at 0400 NZST on the 12th. At this stage, grid 4 was "spawned" on the simulation, and then the model was restarted with FDDA subroutines activated. RAMS allows addition of new grid(s) to a particular simulation after it has started, so that a finer mesh grid can be added to a run whenever it is required to save on computation time. The model was forced (relaxed) towards measured vertical profiles of thermodynamic variables obtained by the aircraft at 0600 NZST. The radius of influence for the assimilated data included only the basin, so that the atmosphere outside the basin used just the model physics. Details on FDDA and relaxation techniques are provided in Fast (1995). Unfortunately, this technique produced unsatisfactory results after the FDDA forcing was stopped at 0600 NZST, and was not pursued further.

A drawback with an early morning initialization is that as the atmospheric static stability is the same inside and outside the basin in the morning (the initialization is horizontally homogenous), characteristic features of the CPB change slightly. To investigate the effect of initialization in the morning, a two-dimensional experiment with the same initial conditions as the three-dimensional runs in this chapter was conducted (results are presented in Appendix A). The two-dimensional simulation indicates that the CPB intrusion into the basin occurs almost two hours earlier, but there is negligible difference in its maximum intensity and cessation time.

6.3 Simulation Results

6.3.1 Influence of Regional Scale on Local Scale Flow

Predicted near surface wind fields for a section of grid 3 after 4, 7 and 10 hours of integration (1000, 1300, 1600 NZST respectively) for LOC-LAKE simulation are presented in Figures 6.3a, b and c. Since the atmosphere was at rest at initialization and no synoptic scale forcings were imposed, the resulting flow fields at 1000 NZST are due to surface heating alone (Figure 6.3a). The winds in the middle of the basin are calm at this time (southwest corner of the domain), as a result of diverging flow set up by the upslope and

up-valley winds around the basin's periphery. This fact was previously illustrated by the regional scale simulations in Chapter 4. Combined upslope and up-valley winds dominate the surface flow field around Lake Tekapo, and up-valley winds are also established in Godley and Macaulay valleys. A weak thermally induced gap wind is evident near Burke Pass, although unfortunately surface wind data are not available to confirm the onset time of the gap wind at this location. At 1300 NZST, the surface flow became more complicated, with the CPB now blowing through Burke Pass and Tekapo Saddle (Figure 6.3b). The flow field south of Tekapo Village is dominated by the gap wind through Burke Pass, while north of the village a gap wind through Tekapo Saddle is pushing away the upslope, up-valley flows. Three hours later at 1600 NZST, easterlies become well established over the bottom half of the domain, and an intrusion is now also evident through the Stoneleigh Saddle (Figure 6.3c). A stagnation zone is created between the passes due to the convergence of the intruding air currents. It is apparent that the surface flow field can be very complicated around Lake Tekapo, and the model is able to capture some of this complexity.

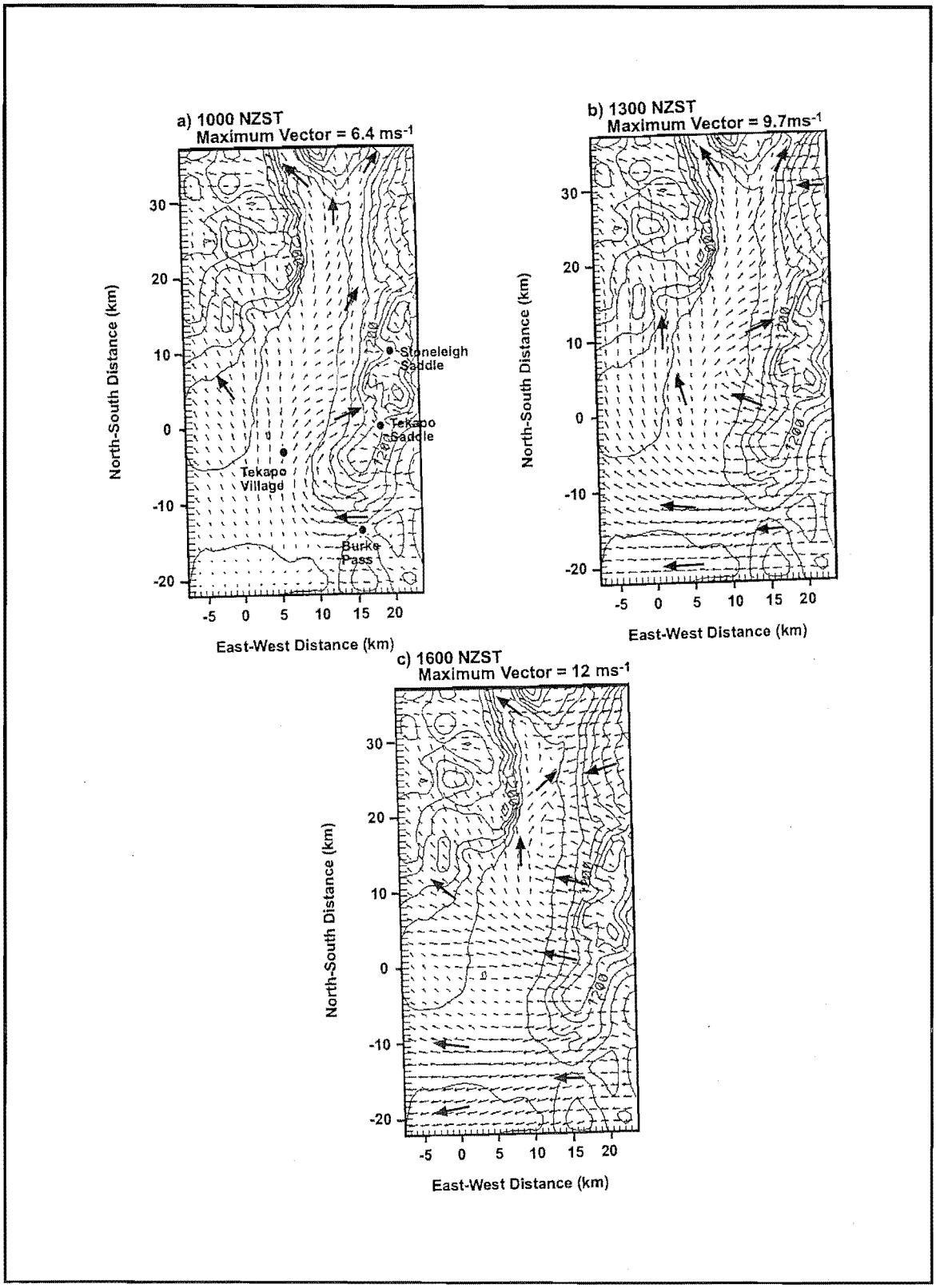

Figure 6.3: Topography (200 m contour interval) and wind vectors on grid 3 at 24 m AGL for (a) 1000 NZST, (b) 1300 NZST, and (c) 1600 NZST for the LOC-LAKE simulation.

6.3.2 Influence of Lake Tekapo

In this section, a comparison between the two high-resolution simulations is made in order to assess the influence of Lake Tekapo on the surface wind field in the region. Therefore, a closer examination of grid 4 model solutions is made in order to observe the resulting differences. According to observational evidence, Lake Tekapo exerts some influence on the surface wind field by generating lake breezes (McGowan *et al.* 1995). The fourth grid in this series of experiments has a high enough resolution to be able to generate thermally driven flows due to the lake, hence making possible a qualitative comparison with observations.

The predicted near surface wind field for the same times as above are presented for both runs in Figure 6.4. At 1000 NZST, the LOC-LAKE run produces a more divergent flow field over the lake than the LOC-LAND run (Figure 6.4a, b). The effect of a lake breeze component is more evident at the south-east corner of the lake. At 1300 NZST, the CPB is dominating the surface wind field at the south-east corner of the domain (Figure 6.4c, d). This is the gap wind which is blowing through Tekapo Saddle (Figure 6.3a), and its front has advanced a little further up the valley in the LOC-LAND run. The most interesting feature of the lake's influence on the surface wind field is evident at 1600 NZST (Figures 6.5a, b). When the lake is not present, the easterly intrusion through the saddles has totally dominated the surface flow field in the valley, with stagnation zones clearly evident on this grid (Figure 6.5b). However, the LOC-LAKE simulation does not show such total dominance of the CPB at this time (Figure 6.5a), since a southerly wind still exists at the northern end of the lake.

To investigate the mechanism responsible for the difference in characteristics of the easterly intrusion at the northern end of the lake, an examination of the cross-valley temperature structure was performed. Simulated potential temperature and wind vector profiles at 1500 and 1600 NZST for both numerical experiments, through a cross-section of grid 4 (line A-B in Figures 6.5a, b) are shown in Figure 6.6 and 6.7. At 1500 NZST, both simulations predict the same intensity and thermal structure (and also the same depth) for the CPB. The CPB at this time has propagated slightly down the slope into the valley for

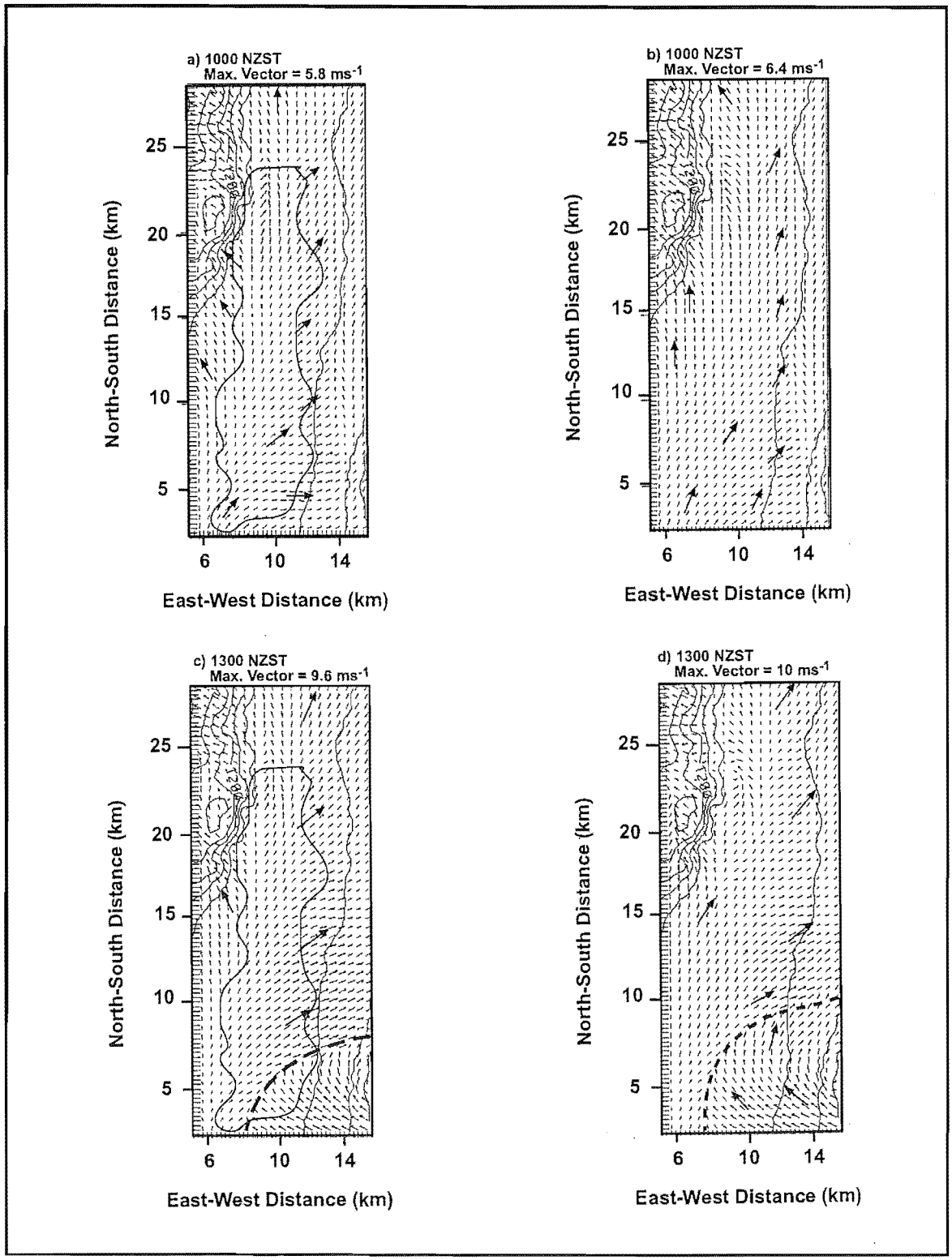

Figure 6.4: Topography (200 m contour interval) and wind vectors on grid 4 at 24 m AGL for (a & b) 1000 NZST, and (c & d) 1300 NZST for LOC-LAKE and LOC-LAND simulations respectively. The solid lines in (a) and (c) indicate the lake's boundary.

both cases. A convergence zone between the upslope flow and the CPB is also apparent in both simulations. However, the presence of the lake has resulted in a colder atmosphere inside the valley in the LOC-LAKE run, and the lake surface has produced a stable layer close to the ground (Figure 6.6a). The formation of this cold air pool at the bottom of the valley in the LOC-LAKE run has some implications for the grounding of the regional scale flow. Figure 6.7a shows that at 1600 NZST, the CPB is overriding the denser air mass in the LOC-LAKE simulation, while at the same time, the current simulated by the LAKE-LAND run is dominating the surface flow field (Figure 6.7b). One hour later (figures not shown), the cold air pool is eroded in the simulation and the easterly in the LOC-LAKE run is grounded.

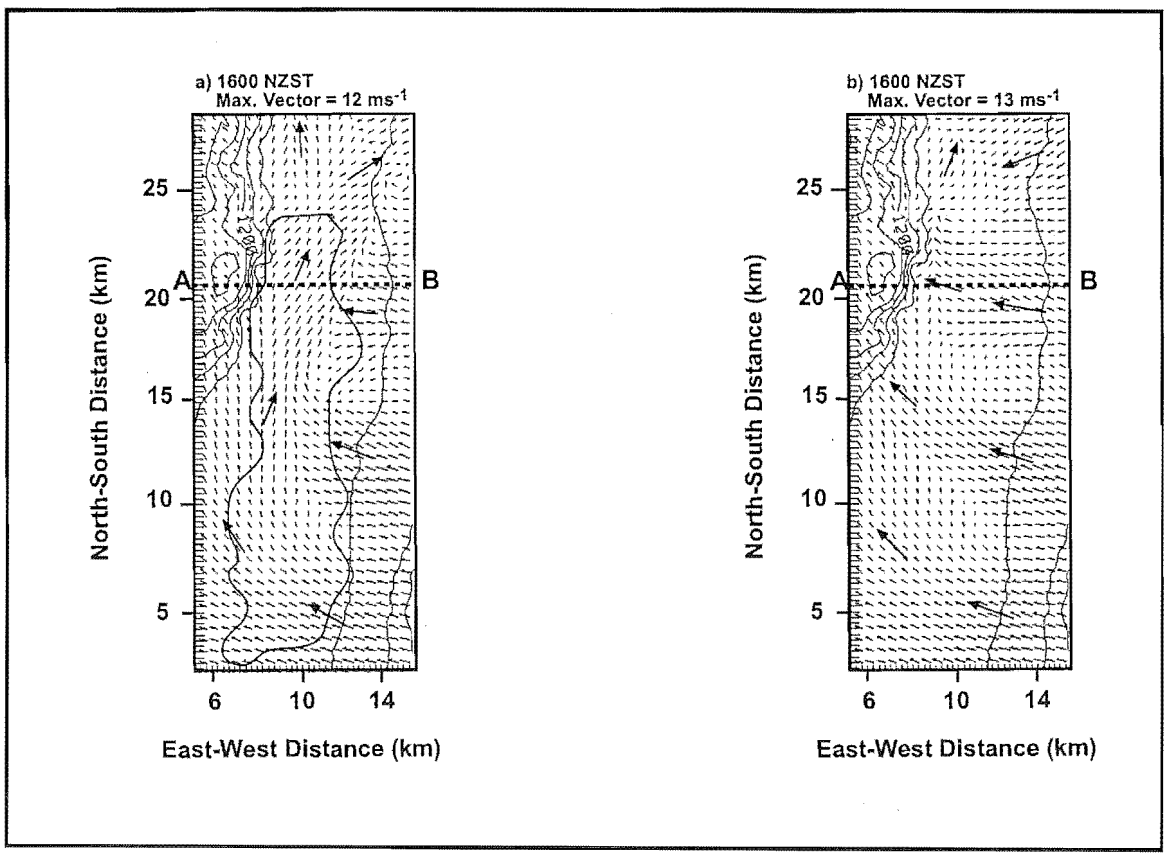

Figure 6.5: Topography (200 m contour interval) and wind vectors on grid 4 at 24 m AGL at 1600 NZST for (a) LOC-LAKE, and (b) LOC-LAND simulations respectively. The solid line in (a) indicates the lake's boundary.

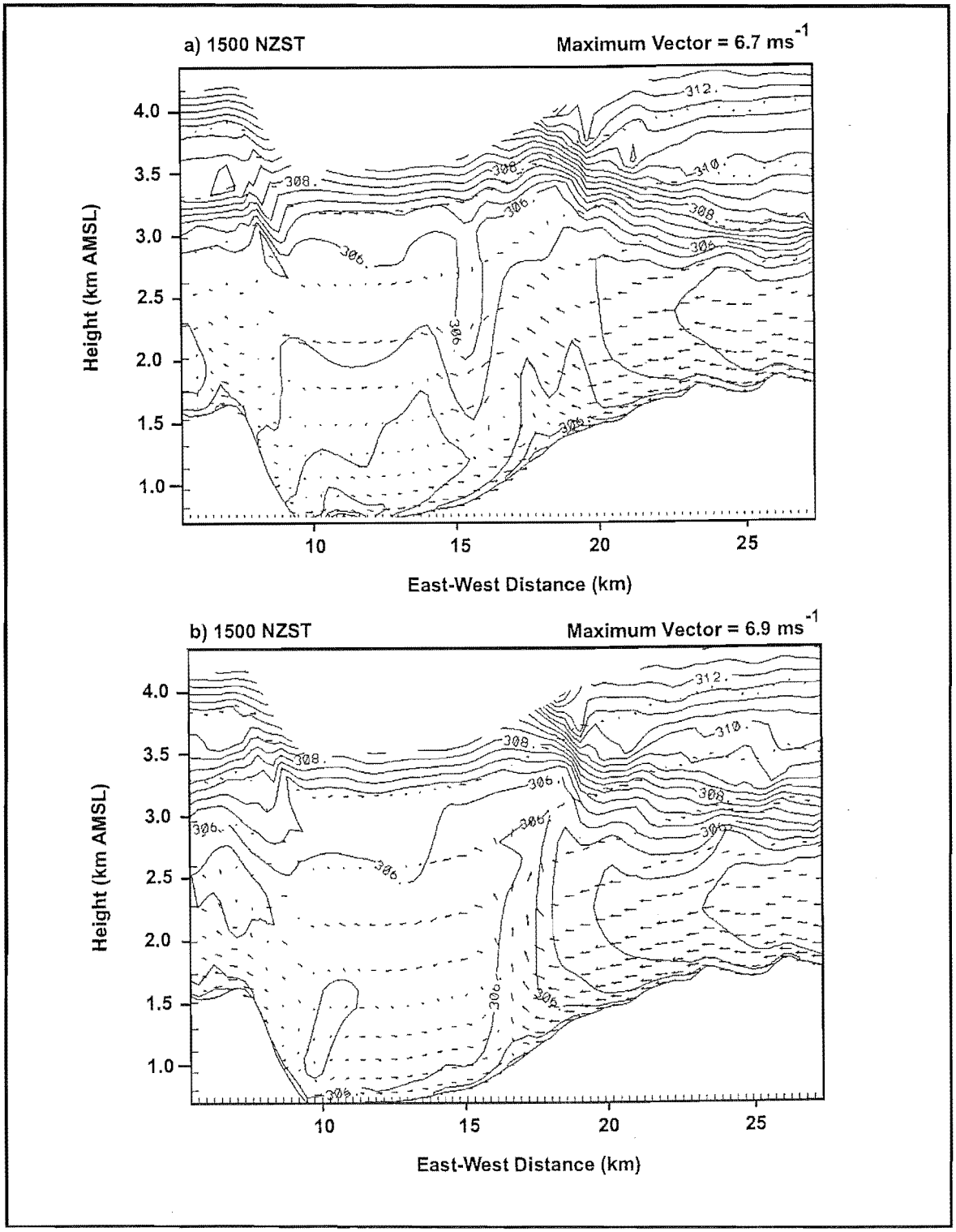

Figure 6.6: Vertical cross-sections of potential temperature and wind vector in the east-west direction through line A-B (location indicated in Figure 6.5), of grid 4 at 1500 NZST for (a) LOC-LAKE, and (b) LOC-LAND simulations.

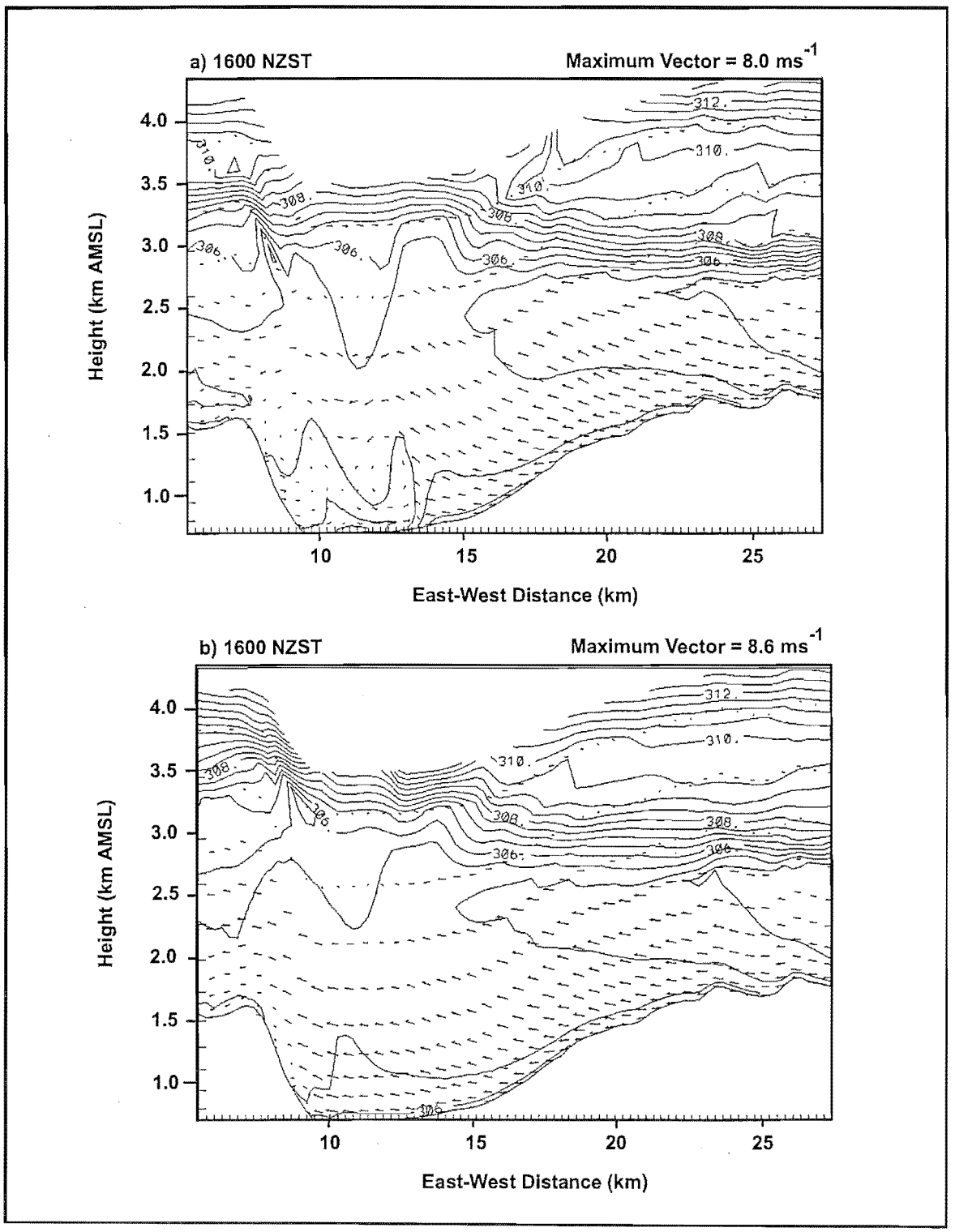

Figure 6.7: Vertical cross-sections of potential temperature and wind vector in the east-west direction through line A-B (location indicated in Figure 6.5), of grid 4 at 1600 NZST for (a) LOC-LAKE, and (b) LOC-LAND simulations.

6.4 Discussion of Results

Since smoothing techniques had to be applied to the topography in order to obtain numerically stable runs, some of the complexity in local relief was lost. For example, even though the horizontal grid spacing for grid 4 was 267 m, Mt. John was not resolved at all on this grid and its influence on the intruding wind system was not simulated. Figure 2.11c clearly showed the deflection of the gap wind through Tekapo Saddle by Mt. John, and this feature would obviously be absent in the model runs described here. However, the complexity of thermally forced wind systems in the Lake Tekapo region was simulated well by the model. The model was able to show that the CPB has a dominating influence on surface flow in the afternoon, by flowing through the mountain gaps and setting up a complex flow system (including stagnation zones) in the vicinity of the lake. Indeed, during the field campaign it became obvious that more weather stations needed to be added to the surface monitoring network. For example, station A13 at Boundary Stream (Figure 2.3) was placed between two saddles and according to model results the gap wind would not be detected there.

Another interesting result from the high resolution simulations is that the cold air pool created by the presence of the lake can affect surface flow fields. Simulation results showed that erosion of the stable layer created by the lake is necessary before the CPB is detected at the surface. A similar situation was modelled by Segal *et al.* (1983) in the case of a cold pool created by a lake confined in a valley. They proposed two mechanisms for erosion of the cold air pool before the prevailing synoptic winds could reach the valley bottom. The first mechanism is the development of an internal gravity wave resulting in flushing of the cold air (Figure 6.8a), and the second mechanism involved erosion from the top due to shear-induced turbulence (Figure 6.8b).

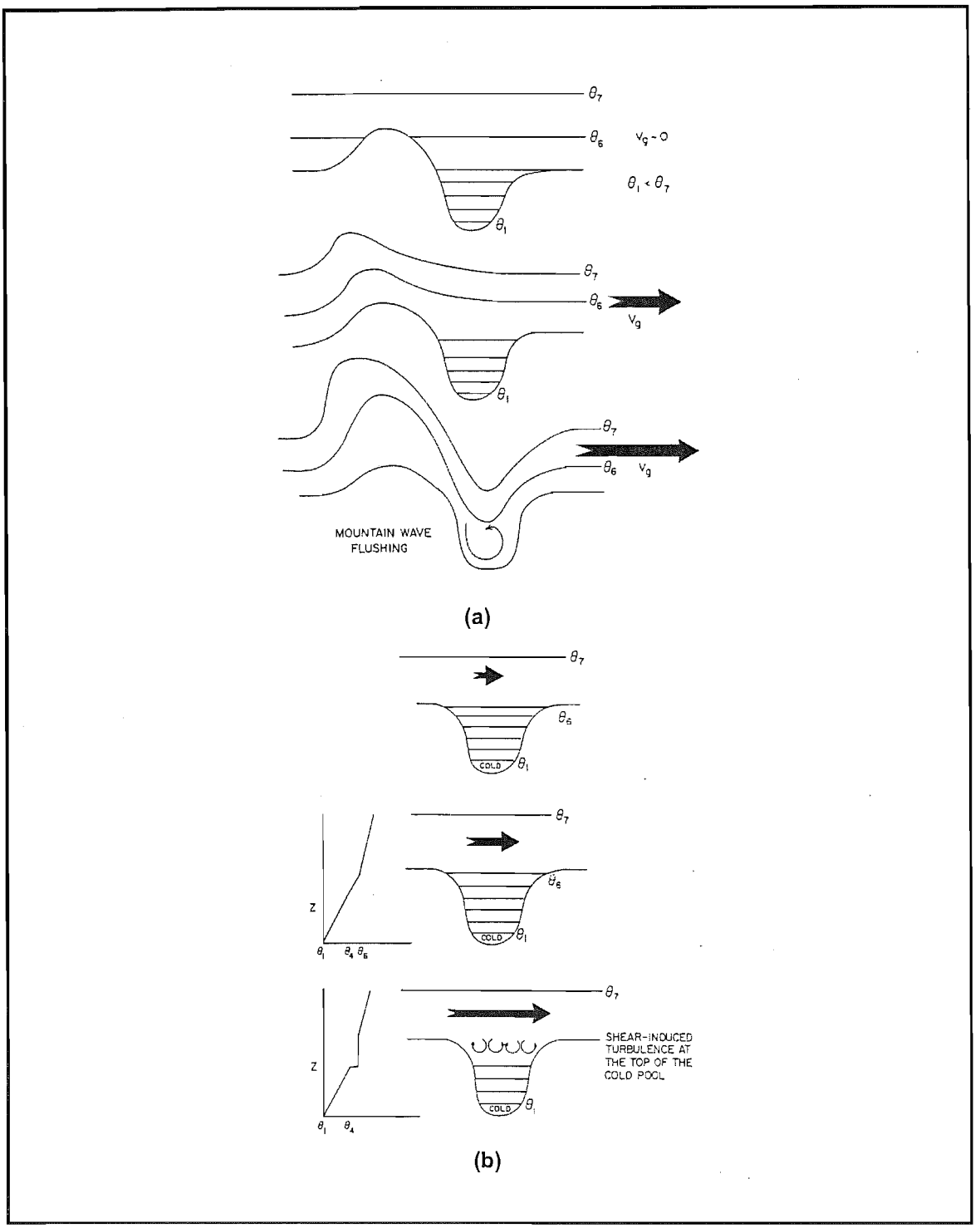

Figure 6.8: Schematic illustration of (a) the flushing of cold air in a valley as a forced internal gravity wave develops over an upwind terrain barrier in response to strengthening synoptic flow, (b) the erosion of cold air in a valley due to shear-induced turbulence at the top of the cold pool (after Segal *et al.*, 1983).

6.5 Conclusion

Results from two high-resolution numerical experiments showed a complex interaction between locally generated thermal circulations and the Canterbury Plains Breeze. In the vicinity of the lake, the CPB dominates the surface flow field in the afternoon by flowing-in through mountain passes. The lake can affect this intrusion by altering the thermal structure of the valley atmosphere through the formation of a stable surface air layer. Simulation results suggest that the CPB has to erode this stable layer before reaching the valley floor.

Chapter 7

Conclusions

Evidence has been presented from both field observations and numerical model results of the existence of a recurring plain-to-basin circulation system, named the Canterbury Plains Breeze (CPB), which dominates the surface flow regime of the MacKenzie Basin region of the South Island in the afternoon of fair weather days. Emphasis was placed on investigating the physical mechanisms responsible for generating the CPB using an atmospheric mesoscale model.

7.1 Summary of Conclusions

It is appropriate at this stage to revisit the original objectives of this thesis from Chapter 1. The objectives were to determine:

- What types of thermally driven circulation systems develop in the vicinity of MacKenzie Basin?
- If the CPB is an intrusion of the sea breeze that forms along the Canterbury coast.
- What are the characteristics of this circulation system and what are the causal mechanisms?
- How variations in ground wetness affect the characteristics of the CPB through its effect on boundary layer growth.

The following sections provide a review of the major findings of this thesis, which were obtained mainly through numerical modelling, but also supported by observations.

7.1.1 Observed Characteristics of the Canterbury Plains Breeze

Observational evidence suggested the presence of a high-speed (> 8ms^{-1}) easterly wind system, that dominated the surface flow field of the basin in the afternoon, when synoptic pressure gradients were weak. The surface monitoring stations situated in the basin showed a predictable onset and cessation time for the CPB, suggesting a thermally driven origin for this circulation. However, the intrusion characteristics of the CPB in the Lake Tekapo region were somewhat more complicated. During the 2nd February case study, a high-speed wind was detected in the basin in the afternoon, but the airflow did not seem to intrude into the lake area until after sunset, when it blew down the western slopes of the Two Thumb Range. On the 12th February case study day, the easterly intrusion was again detected in the basin, and it manifested itself in the Lake Tekapo region as a strong gap wind flowing through Tekapo Saddle. Measurements from surface stations and vertical temperature profiles measured by an aircraft suggest that the Canterbury Plains Breeze advects colder coastal air into the basin, therefore having an important impact on the climate of the region.

7.1.2 Numerical Simulations of the CPB

Three-dimensional numerical experiments configured to represent mesoscale forcings on a regional scale showed that the CPB can form exclusively as a result of terrain heating. The three-dimensional idealized simulations with and without the ocean surrounding the South Island showed no difference in the onset and cessation time of the CPB in the basin, although there was a decrease of 1 ms^{-1} in the intensity of wind in the simulation with no ocean. This result suggests that the CPB is a separate circulation system from the sea breeze that forms over the Canterbury Plains due to land-sea contrasts, and is only affected to a small degree by the ocean surrounding the South Island.

Subsequently, results from twelve two-dimensional numerical experiments showed that the CPB is a plain-to-basin circulation system forced by horizontal temperature

gradients between the air inside the basin and that over the surrounding plains at the same elevation. The physical forcing mechanism can be explained in the following way, daytime heating of the atmosphere over the basin results in a hydrostatically created horizontal pressure gradient force directed from the plains to the basin. This pressure gradient force causes movement of air towards the basin. The resulting airflow can either go through mountain saddles or gaps, or flow into the basin over the ridge lines. When the mixed layer growth outside the basin is suppressed by cold air advection, due to either a sea breeze or high soil moisture content of the surface of the plains, the intensity of the CPB increases. The two-dimensional experiments suggest that the reason for this increase is the reduced heating of air above the plains (at a level above the basin floor height) due to the reduced mixed layer growth. This results in an increase in the horizontal pressure gradient that drives the CPB. Therefore, factors that enhance (suppress) mixed layer growth over the plains decrease (increase) the intensity of the plain-to-basin circulation system. Hence, even though the sea breeze circulation over the Canterbury Plains does not have a direct impact on the CPB, it has an indirect influence by reducing the mixed layer height over the plains (outside the basin).

7.1.3 Interaction of the CPB with Smaller Scale Flows

Results from two high-resolution three-dimensional simulations show how the CPB affects the surface flow regime in the vicinity of Lake Tekapo, and suggest ways that it can interact with the cold layer of air created by the presence of the lake. The simulations clearly showed the intrusion of the CPB as gap winds through several saddles in the Two Thumb Range which the observational network mostly missed (except for the Base site). The existence of these flows has implications for the other components of the LTEX research project, and has to be considered when along-valley budget studies of mass and heat are performed. The model runs suggest that the plain-to-basin wind will not be detected at some places by surface weather stations until the stable surface layer created by the lake is eroded.

7.1.4 Broader Implications

High-resolution numerical analysis of thermally generated wind systems has only been possible in the past decade due to the development of high-speed computers. Research projects that use mesoscale models in conjunction with observational evidence have had some success in describing the nature of such flow systems. Due to the large horizontal extent of the forcing, even the most ambitious field projects like the IMADA-AVER experiment in Mexico City Basin (Doran *et al.* 1998) were not able to offer a complete description of this flow system. Therefore, the findings from the numerical experiments in this research provides additional information relating to the development of plain-to-basin type flows, especially for basins that are situated in coastal areas. Broader implications of this research are that land use patterns can affect the characteristic features of the plain-to-basin wind, so that anthropogenic land use change may affect these wind systems. For example, planting trees for forestry practices or setting up extensive irrigated areas for agriculture use can reduce the mixed layer growth in the MacKenzie Basin leading to a weakened CPB circulation. In addition, the persistence and intensity of the CPB suggests that it can transport air pollutants from the Canterbury Plains into the mountain basins, adversely affecting the air quality in this region. As a result, it is clear that degradation of air quality over the Canterbury Plains could adversely affect the air quality in alpine regions of the South Island.

7.2 Suggestions for Future Research

Obviously, more research is necessary to understand more fully the exact nature of regional scale circulations such as the Canterbury Plains Breeze. Currently, more observational data are needed to confirm the simulated characteristic features of the CPB. Since the model runs suggest that horizontal pressure gradients are a forcing factor for the plain-to-basin type flows, it would be highly desirable to have concurrent vertical profiles of thermodynamic variables over both the basin (plateau) and the adjacent plains. It would also be advantageous to have wind measurements over the slopes, mountain gaps and

passes. The observational data could be used for further investigation of the phenomenon, through both model initialization and verification of model results.

The numerical modelling aspects of this research could also be expanded on. Suggestions for improvement of model formulation are not made here, since the topic was not investigated in this research. However, there is a need for even higher-resolution model runs to be performed. With higher resolution runs, local topographic features such as Mt. John, that have an important influence in diverting airflows could be resolved by the model. This improvement would enable a more direct comparison between observations and model results. The simulations in Chapter 6 were performed with a horizontal grid spacing of 267 m and a vertical grid spacing of 50 m for the first level near the surface. Both grid spacings could be made smaller using a numerical code like RAMS. However, this was impractical for this research due to the large amount of computational time required. In spite of this limitation, the high-resolution runs were able to simulate some observed (although not fully measured) characteristics of the CPB, and suggested the way that it might interact with the stable layer created by the cold surface of Lake Tekapo.

It is also suggested that in future meteorological studies in areas of complex terrain, a preliminary numerical modelling study of the experimental site be conducted in order to have a better understanding of types of thermally driven winds that can affect the region. This would hopefully aid in the design of the surface monitoring network.

References:

Anthes, R. A., 1978: The height of the planetary boundary layer and the production of circulation in a sea breeze model. *J. Atmos. Sci.*, **35,** 1231-1239.

Anthes, R. A., and T. T. Warner, 1978: Development of hydrodynamic models suitable for air pollution and other mesometeorological studies. *Mon. Wea. Rev.*, **106,** 1045-1078.

Arya, S. P., 1988: *Introduction to Micrometeorology.* Academic Press, 307 pp.

Atkinson, B. W., 1981: *Meso-scale Atmospheric Circulations.* Academic Press, 495 pp.

Avissar, R., and R. A. Pielke, 1989: A parameterization of heterogenous land surface for atmospheric numerical models and its impact on regional meteorology. *Mon. Wea. Rev.*, **117,** 2113-2136.

Barry, R. G., 1992: *Mountain Weather and Climate.* 2d Ed. Routledge, 402 pp.

Bossert, J. E., 1997: An investigation of flow regimes affecting the Mexico City regions. *J. Appl. Meteorol.*, **36,** 119-140.

Bossert, J. E., and W. R. Cotton, 1994a: Regional-scale flows in mountainous terrain. Part I: A numerical and observational comparison. *Mon. Wea. Rev.*, **122,** 1449-1471.

Bossert, J. E., and W. R. Cotton, 1994b: Regional-scale flows in mountainous terrain. Part II: Simplified numerical experiments. *Mon. Wea. Rev.*, **122,** 1472-1489.

Brown, R. A., 1991: *Fluid Mechanics of the Atmosphere.* Academic Press, 489 pp.

Businger, J. A., C. J. Wyngaard, Y. Izumi, and E. F. Bradley, 1971: Flux-profile relationship in the atmospheric surface layer. *J. Atmos. Sci.*, **28,** 181-189.

Carpenter, K. M., 1979: An experimental forecast using a nonhydrostatic mesoscale model. *Q. J. R. Meteorol. Soc.*, **105,** 629-655.

Chen, C., and W. R. Cotton, 1983: A one-dimensional simulation of the stratocumulus-capped mixed layer. *Bound.-Layer Meteor.*, **25,** 289-321.

Clark, T. L., 1977: A small-scale dynamic model using a terrain-following coordinate transformation. *J. Comput. Phys.*, **24,** 186-215.

Clark, T. L., and R. D. Farley, 1984: Severe downslope windstorm calculations in two and three spatial dimensions using anelastic interactive grid nesting: a possible mechanism for gustiness. *J. Atmos. Sci.*, **41,** 329-350.

Clark, T. L., and W. D. Hall, 1991: Mutli-domain simulations of the time dependent Navier-Stokes equations: benchmark error analysis of some nesting procedures. *J. Comput. Phys.*, **92,** 456-481.

Danard, M., 1977: A simple model for mesoscale effects of topography on surface winds. *Mon. Wea. Rev.*, **105,** 572-581.

Defant, F., 1951: Local winds. *Compendium of Meteorology*, American Meteorological Society, 655-672.

Dickerson, M. H., 1978: MASCON – a mass-consistent atmospheric flux model for regions with complex terrain. *J. Appl. Meteorol.*, **17,** 241-253.

Dickerson, M. H., and P. H. Gudiksen, 1980: "ASCOT FY-1979 Progress Report", UCRL-52899/ascot/1. Lawrence Livermore National Laboratory, Livermore, California.

Dickerson, M. H., and P. H. Gudiksen, 1981: "ASCOT F-1981 Progress Report", UCID-18878-81, ASCOT-2.

De Wekker, S. F. J., S. Zhong, J. D. Fast, and C. D. Whiteman, 1998: A numerical study of the thermally driven plain-to-basin wind over idealized basin topographies. *J. Appl. Meteor.*, **37,** 606-622.

Doran, J. C., and E. D. Skyllingstad, 1992: Multiple-scale terrain forcing of local wind fields. *Mon. Wea. Rev.*, **120,** 817-825.

Doran, J. C., and S. Zhong, 1994: Regional drainage flows in the Pacific Northwest. *Mon. Wea. Rev.*, **122,** 1158-1167.

Doran, J. C., and Coauthors, 1998: The IMADA-AVER boundary layer experiment in the Mexico City area. *Bull. Amer. Meteor. Soc.*, **79,** 2497-2508.

Doran, J. C., and S. Zhong, 2000: Thermally driven gap winds into the Mexico City Basin. *J. Appl. Meteor.*, **39,** 1330-1340.

Droegemeier, K. K., M. Xue, K. Johnson, K. Mills, and M. O'Keefe, 1993: Experiences with the scalable-parallel ARPS cloud/mesoscale prediction model on massively parallel and workstation cluster architectures. *Parallel Supercompting in Atmospheric Science,* G. R. Hoffman and T. Kauranne, Eds., World Scientific, 99-129.

Fast, J. D., 1995: Mesoscale modelling and four-dimensional data assimilation in areas of highly complex terrain. *J. Appl. Meteorol.*, **34,** 2762-2782.

Fast, J. D., S. Zhong, and C. D. Whiteman, 1996: Boundary layer evolution within a canyonland basin. Part II: numerical simulations of nocturnal flows and heat budgets. *J. Appl. Meteor.*, **35,** 2162-2178.

Flohn, H., 1969: Local wind systems. World Survey of Climatology, Vol 2, Elsevier, New York: 139-171.

Gal-Chen, T., and R. C. J. Somerville, 1975: On the use of a coordinate transformation for the solution of the Navier-Stokes equations. *J. Comput. Phys.*, **17,** 209-228.

Garr, G. E., and B. B. Fitzharris, 1991: A climate classification of New Zealand based on numerical techniques. *New Zealand Geographer,* **47,** 60-71.

Helfand, H. M., and J. C. Labraga, 1988: Design of a nonsingular level 2.5 second-order closure model for the prediction of atmospheric turbulence. *J. Atmos. Sci.,* **45,** 113-132.

Holton, J. R., 1979: *An Introduction to Dynamical Meteorology.* 2d ed. Academic Press, 391 pp.

Hsu, H.-M., 1979: Numerical simulations of mesoscale precipitation systems. Ph.D. dissertation, Department of Atmospheric and Oceanic Sciences, University of Michigan, Ann Arbor.

Jeffreys, H., 1922: On the dynamics of the wind. *Quart. J. Roy. Meteor. Soc.* **48,** 29-47.

Kikuchi, Y., S. Arakawa, F. Kimura, K. Shirasakin, and Y. Nagano, 1981: Numerical study on the effects of mountains on the land and sea breeze circulation in the Kanto district. *J. Meteorol. Soc. Jpn.,* **59,** 723-738.

Kimura, F., and T. Kuwagata, 1993: Thermally induced wind passing from plain to basin over a mountain range. *J. Appl. Meteor.*, **32,** 1538-1547.

Klemp, J. B., and R. B. Wilhelmson, 1978a: The simulation of three-dimensional convective storm dynamics. *J. Atmos. Sci.,* **35,** 1070-1096.

Klemp, J. B., and R. B. Wilhelmson, 1978b: Simulations of right- to left-moving storms produced through storm splitting. *J. Atmos. Sci.,* **35,** 1097-1110.

Kondo. J., T. Kuwagata, and S. Haginoya, 1989: Heat budget analysis of nocturnal cooling and daytime heating in a basin. *J. Atmos. Sci.,* **46,** 2917-2933.

Kurita, H., H. Ueda, and S. Mitsumoto, 1990: Combination of local wind systems under light gradient wind conditions and its contribution to the long-range transport of air pollutants. *J. Appl. Meteor.,* **29,** 331-348.

Lee, T. J., R. A. Pielke, R. C. Kessler, and J. Weaver, 1989: Influence of cold pools down-stream of mountain barriers on down-slope winds and flushing. *Mon. Wea. Rev.,* **117,** 2041-2058.

Ligda, M. G. H., 1951: Radar storm observation. *Compendium of Meteorology,* American Meteorological Society, 1265-1282.

Louis, J-.F, 1979: A parameteric model of vertical eddy fluxes in the atmosphere. *Bound-Layer Meteor.,* **17,** 187-202.

Lu, R., and R. P. Turco, 1994: Air pollutant transport in a coastal environment. Part I: Two-dimensional simulations of sea-breeze and mountain effects. *J. Atmos. Sci.*, **51,** 2285-2308.

Lu, R., and R. P. Turco, 1995: Air pollutant transport in a coastal environment. Part II: Three-dimensional simulations over Los Angeles Basin. *Atmos. Env.*, **29,** 1499-1518.

Mahrer, Y., and R. A., Pielke, 1976: Numerical simulation of air flow over Barbados. *Mon. Wea. Rev.*, **104,** 1392-1402.

Mahrer, Y., and R. A. Pielke, 1977a: A numerical study of the airflow over irregular terrain. *Beitr. Phys. Atmos.*, **50,** 98-113.

Mahrer, Y., and R. A., Pielke, 1977b: The effects of topography on the sea and land breezes in a two-dimensional numerical model. *Mon. Wea. Rev.*, **105,** 1151-1162.

Mahrer, Y., and R. A. Pielke, 1978: The meteorological effect of the changes in surface albedo and moisture. *Isr. Meteorol. Res. Pap.*, **2,** 55-70.

Mannouji, N., 1982: A numerical experiment on the mountain and valley winds. *J. Meteor. Soc. Japan*, **60,** 1085-1105.

McGowan, H. A., I. Owens, and A. P. Sturman, 1995: Thermal and dynamic characteristics of alpine lake breezes, Lake Tekapo, New Zealand. *Bound.-Layer Meteor.*, **76,** 3-24.

McGowan, H. A., and A. P. Sturman, 1996: Interacting multi-scale wind systems within an alpine basin, Lake Tekapo, New Zealand. *Meteorol. Atmos. Phys.*, **58,** 165-177.

McKendry, I. G., A. P. Sturman, and I. F. Owens, 1986: A study of interacting multi-scale wind systems, Canterbury Plains, New Zealand. *Meteorol. Atmos. Phys.*, **35,** 242-252.

McNider, R. T., 1981: Investigation of the impact of topographic circulations on the transport and dispersion of air pollutants. Ph.D. dissertation, University of Virginia, Department of Environmenta Sciences, Charlottesville, Va.

McPherson, R. D., 1970: A numerical study of the effect of a coastal irregularity on the sea breeze. *J. Appl. Meteorol.*, **9,** 767-777.

Mellor, G. L., and T. Yamada, 1974: A hierarchy of turbulence closure models for planetary boundary layers. *J. Atmos. Sci.*, **31,** 1791-1806.

Mellor, G. L., and T. Yamada, 1982: Development of a turbulence closure model for geophysical fluid problems. *Rev. Geophys. Space Phys.*, **20,** 851-875.

Mesinger, F., and A. Arakawa, 1976: Numerical methods used in atmospheric models. GARP Publication Series, No. 14, WMO/ICSU Joint Organizing Committee, 64 pp.

Morris, C., J. R. Fairweather, and S. R. Swaffield, 1997: *Investigating Community: Imperatives For but Constraints Against Land Use Change in the MacKenzie/Waitaki Basin.* Research Report No. 236, Agribusiness & Economics Research Unit, Lincoln University, Canterbury, New Zealand, 96 pp.

Monin, A. S., and A. M. Obukhov, 1954: Basic regularity in turbulent mixing in the surface layer of the atmosphere. *Akad. Nauk. S.S.S.R. Trud. Geofiz. Inst.,* **24,** 163-187.

Oke, T. R., 1992: *Boundary Layer Climates.* 2d Ed. Routledge, 435 pp.

Oliphant, A., 2000: Spatial and temporal variability of surface energy fluxes in an alpine catchment. Ph.D. dissertation. University of Canterbury, 200 pp.

Orlanski, I., 1975: A rational subdivision of scales for atmospheric processes. *Bull. Amer. Meteor. Soc.,* **56,** 529-530.

Patnack, P. C., B. E. Freeman, R. M. Traci, and G. T. Phillips, 1983: *Improved Simulations of Mesoscale Meteorology.* Report Atmospheric Science Laboratory, White Sands Missile Range, NM, ASL CR-83-0127-1.

Pielke, R. A., 1974: A three-dimensional numerical model of the sea breezes over south Florida. *Mon. Wea. Rev.,* **102,** 115-139.

Pielke, R. A., 1984: *Mesoscale Meteorological Modeling.* Academic Press, 612 pp.

Pielke, R. A., 1985: The use of mesoscale numerical models to asses wind distribution and boundary-layer structure in complex terrain. *Bound.-Layer Meteor.,* **31,** 217-231.

Pielke, R. A., W. R. Cotton, R. L. Walko, C. J. Tremback, W. A. Lyons, L. D. Grasso, M. E. Nicholls, M. D. Moran, D. A. Wesley, T. J. Lee, and J. H. Copeland, 1992: A comprehensive meteorological modeling system – RAMS. *Meteorol. Atmos. Phys.,* **49,** 69-91.

Revell, M. J., D. Purnell, and M. K. Lauren, 1996: Requirements for large-eddy simulation of surface wind gusts in a mountain valley. *Bound.-Layer Meteor.,* **80,** 333-353.

Rider, D. J., and M. Armendariz, 1970: Vertical wind component estimates up to 1.2 km above ground. *J. Appl. Meteor.,* **5,** 64-71.

Segal, M., Y. Mahrer, and R. A. Pielke, 1983: A numerical model study of meteorological patterns assiciated with a lake confined by mountains – the dead sea case. *Quart. J. Roy. Meteorol. Soc.,* **109,** 549-564.

Smagorinsky, J., 1963: General circulation experiments with the primitive equations. Part I, The basic experiment. *Mon. Wea. Rev.*, **91,** 99-164.

Steinacker, R., 1984: Area-height distribution of a valley and its relation to the valley wind. *Contrib. Atmos. Phys.*, **57,** 64-71.

Stull, R. B., 1988: *An Introduction to Boundary Layer Meteorology.* Kluwer, 666 pp.

Sturman, A. P., and N. Tapper, 1996: *The Weather and Climate of Australia and New Zealand.* Oxford University Press, 476 pp.

Sturman, A. P., S. Bradley, P. Drummond, K. Grant, P. Gudiksen, V. Hipkin, M. Kossman, H. A. McGowan, A. Oliphant, I. F. Owens, S. Powell, R. Spronken-Smith, T. Webb, and P. Zawar-Reza, 2000: The Lake Tekapo Experiment (LTEX): an investigation of atmospheric boundary layer processes in complex terrain. *Bulletin of American Meteorological Society (to be submitted).*

Tang, M., and E. R. Reiter, 1984: Plateau monsoons of the Northern Hemisphere: a comparison between North America and Tibet. *Mon. Wea. Rev.*, **112,** 617-637.

Tannehill, J. C., D. A. Anderson, and R. H. Pletcher, 1997: *Computational Fluid Mechanics and Heat Transfer.* Taylor & Francis, 792 pp.

Tremback, C. J., and R. Kessler, 1985: A surface temperature and moisture parameterization for use in mesoscale numerical models. Preprints, *7th Conference on Numerical Weather Prediction*, 17-20 June 1985, Montreal, Canada, AMS.

Tremback, C. J., 1990: Numerical simulation of a mesoscale convective complex: Model development and numerical results. Ph.D. dissertation. Colorado State University, 247 pp.

Tripoli, G. J., and W. R. Cotton, 1981: The use of ice-liquid water potential temperature as a variable in deep atmospheric models. *Mon. Wea. Rev.*, **109,** 1094-1102.

Tripoli, G. J., and W. R. Cotton, 1982: The Colorado State University three-dimensional cloud/mesoscale model – 1982. Part I: General theoretical framework and sensitivity experiments. *J. de Rech. Atmos.*, **16,** 185-220.

Tyson, P. D., and R. A. Preston-Whyte, 1972: Observations of regional topographically-induced wind systems in Natal. *J. Appl. Meteor.*, **11,** 643-650.

Vinnichenko, N. K., 1970: The kinetic energy spectrum in the free atmosphere – one second to five years. *Tellus,* **22,** 158-166.

Wagner, A., 1938: Theorie und Beobachtung der periodischen gebirgwinde. *Gerlands Beitr. Geophys.*, **52,** 408-449. [English translation: Whiteman C. D., and E. Dreiseitl, 1984: Alpine meteorology. Translation of classic contributions by A. Wagner, E. Ekhart and F. Defant. PNL-5141/ASCOT-84-3. Pacific Northwest Laboratory, Richland, WA, 121pp.]

Wallace, J. M., and P. V. Hobbs, 1977: *Atmospheric Science: An Introductory Survey.* Academic Press, 467 pp.

Warner, T. J., R. A. Anthes, and A. L. McNab, 1978: Numerical simulations with a three-dimensional mesoscale model. *Mon. Wea. Rev.*, **106,** 1079-1099.

Whiteman, C. D., 1990: Observations of thermally developed wind systems in mountainous terrain. *Atmospheric Processes Over Complex Terrain, Meteor. Monogr.,* No. 45, Amer. Meteor. Soc., 5-42.

Whiteman, C. D., T. B. McKee, and J. C. Doran, 1996: Boundary layer evolution within a canyonland basin. Part I: mass, heat, and moisture budgets from observations. *J. Appl. Meteor.*, **35,** 2145-2161.

Whiteman, C. D., 2000: *Mountain Meteorology.* Oxford University Press, 355 pp.

Wratt, D. S., R. N. Ridley, M. R. Sinclair, H. Larsen, S. M. Thompson, R. Henderson, G. L. Austin, S. G. Bradley, A. Auer, A. P. Sturman, I. Owens, B. Fitzharris, B. F. Ryan, and J.-F. Gayet, 1996: The New Zealand Southern Alps Experiment. *Bulletin of American Meteorological Society,* **77,** 683-692.

Wratt, D. S., and M.R. Sinclair, 1996: SALPEX – The Southern Alps Experiment. *Water and Atmosphere,* **4(2),** 26-28.

Yamada, T., 1981: A numerical simulation of nocturnal drainage flow. *J. Meteorol. Soc. Jpn,* **59,** 108-122.

Zhong, S., J. D. Fast, and X. Bian, 1996: A case study of the Great Plains low-level jet using profiler network data and a high-resolution mesoscale model. *Mon. Wea. Rev.,* **124,** 785-806.

Appendix A

Effects of Early Morning Initialization on the Simulated Development of the CPB

As previously discussed, high resolution simulations in Chapter 6 were initialized horizontally homogeneously early in the morning at 0600 NZST 12 February. Therefore, unlike the simulations in the rest of this thesis, the runs did not cycle through a nocturnal phase. Bypassing the nocturnal phase results in the following differences between the runs early in the morning:

1) without a simulated nocturnal phase, spatially variable lower level stratification is not generated and the thermal stratification between the air inside and outside the basin at the same level is identical (no cold air pool in the basin early in the morning)
2) nocturnal flows resulting from overnight surface radiative cooling will be absent in the run that is initialized in the morning (since the atmosphere starts at rest)

Therefore, the effects of such an initialization on the development of the CPB needs to be investigated. The approach used is to perform a simplified two-dimensional numerical experiment with the "basin" topographic configuration (description provided in Chapter 5) using the initialization procedures for the high resolution simulations in Chapter 6.

Two-Dimensional Simulation Development

The two-dimensional test was only performed with the "basin" topographic configuration, since the characteristic features of the density current did not differ much between the different configurations. The model setup parameters for this run are the same as the BASO simulation in Chapter 5, except that the roughness length was set to 5 cm to conform with the value selected for the high resolution simulations. The model run was initialized at 0600 NZST 12th February 1999 with near zero initial winds, and with the vertical profile of temperature and humidity presented in Chapter 6. Hence, except for the time of initialization and the initial thermal stratification, this run is the same as the BASO run and is designated as BASO-0600.

Simulation Results

Figure A.1 presents simulated potential temperature and u-component wind fields after 6, 8 and 10 hours of integration (1200, 1400, 1600 NZST respectively). At 1200 NZST the Canterbury Plains Breeze has already propagated down the basin side slope (Figures A.1a, b). The mixed layer inside the basin has grown to a depth of approximately 900 m, although, due to the initial thermal stratification, the mixed layer depth over the slope on the plain side is approximately 300 m resulting in a shallower CPB circulation. This is in contrast to the BASO run, where the current was 1 km deep above the ridge top, highlighting the fact that thermal stratification outside the basin plays an important role in the characteristics of the CPB. This characteristic feature cannot be confirmed due to lack of observations. By 1400 NZST the current has propagated halfway across the basin with an intensity of 4 ms^{-1}. At this time, the head of the current is about 10 km ahead of the flow simulated in the BASO run (Figures A.1c, d). By 1600 NZST the CPB has reached the main divide and is dominating the flow throughout the basin, whereas in the BASO run the head of the current was 5 km away from reaching the main divide.

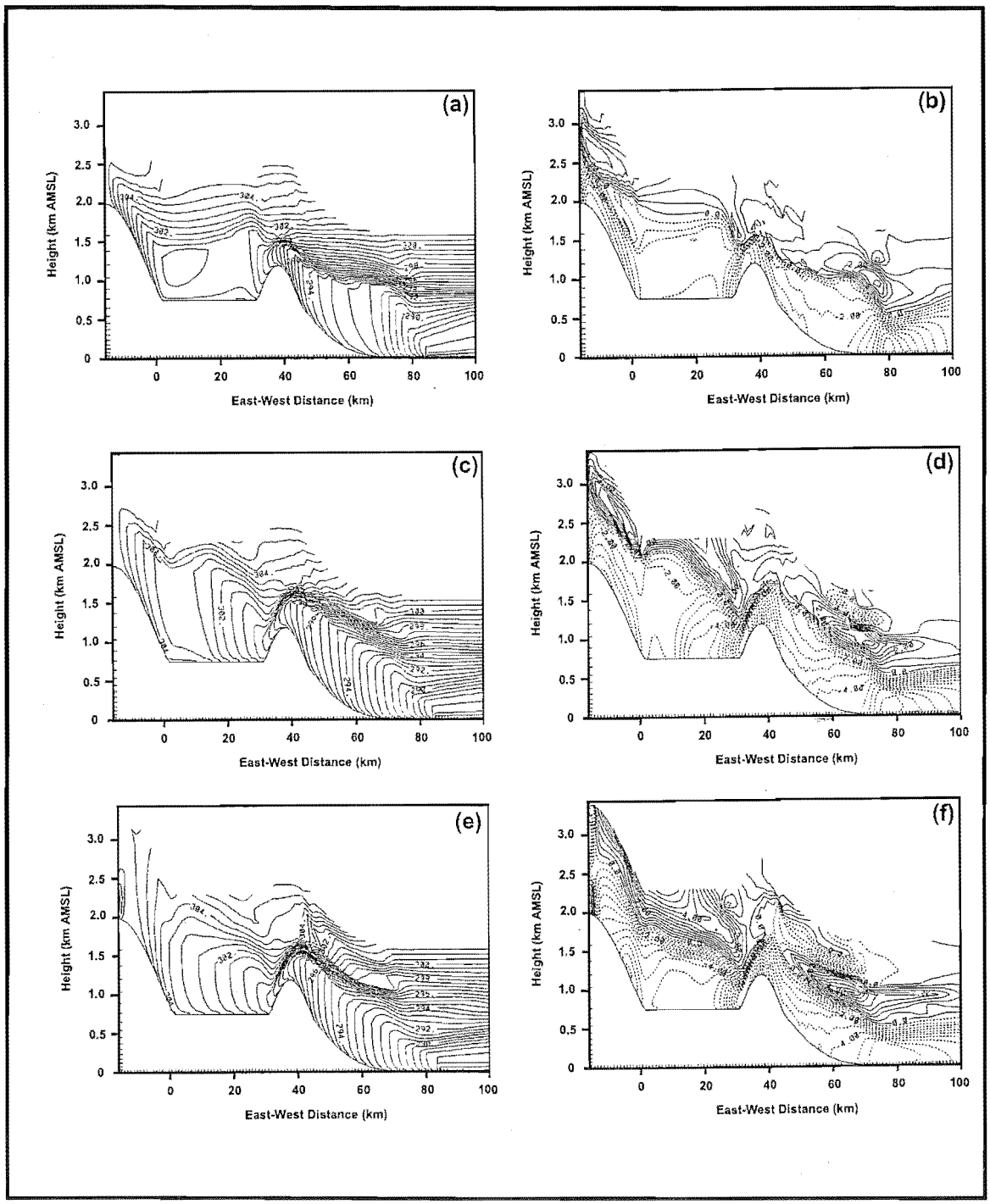

Figure A.1: Simulated *u*-component wind isopleths (ms^{-1}) on the right and potential temperature field (K) on the left for the BASO-0600 experiment at (a & b) 1200, (c & d) 1400 and (e & f) 1600 NZST. Dashed isopleths indicate negative *u*-component (winds blowing from right to left). Contour interval is 0.5 K for the potential temperature fields, and 0.5 ms^{-1} for the isopleths.

Time series of the *u*-component of wind at the surface (same location as indicated in Figure 5.1) shows that the CPB reached this site about an hour and a half earlier than the BASO run (Figure A.2). The onset of the breeze was much more gradual, but it ceased as quickly as the BASO run. Also, the maximum intensity of the

current was about 1 ms^{-1} less than the BASO run. De Wekker *et al.* (1998) reported that if they initialized their two-dimensional simulations in the morning, the plain-to-basin circulation had a stronger intensity. Their finding seems to be in contradiction with the results here. However, in their simulations the topographic configuration is symmetrical (both peaks have the same elevation), and the plain-to-basin intrusion generally occurs after the upslope flows have ceased. With the asymmetric configuration used here, the effect on the plain-to-basin circulation is the earlier intrusion time leading to a slightly less intense inflow.

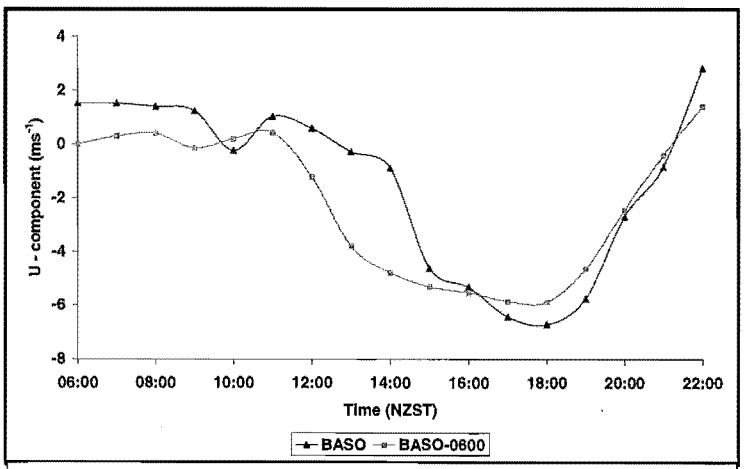

Figure A.2 Time series of *u*-component winds for BASO and BASO-0600 simulations.

Appendix B

The following is an example of the namelist file (RAMSIN) used to configure the BAS model simulation in Chapter 5. Note that only the relevant portions of this file are included below.

MODEL_GRIDS

```
  Simulation title (64 chars)
  EXPNME  =    '3a-0610' ,
  IOTYPE   = 0,                          ! -1=diagnostic, 0=normal run
  RUNTYPE = 'INITIAL',
  TIMEUNIT = 'h',                        ! 'h','m','s' - Time units of
                                         !   TIMMAX, TIMSTR, VTIME
  TIMMAX= 30.,                           ! Final time of simulation
  NGRIDS  =   1,                         ! Number of grids to run
  NNXP    =  465,                        ! Number of x gridpoints
  NNYP    =  5,                          ! Number of y gridpoints
  NNZP    =  42,                         ! Number of z gridpoints
  NNZG    =  11,                         ! Number of soil gridpoints
  NXTNEST =   1, 1, 2, 3,                ! Grid number which is the next
                                            !   coarser grid
```

Coarse grid specifications

```
   IHTRAN  =      1,                     ! 0-Cartesian, 1-Polar stereo
   DELTAX  =   1000.,
   DELTAY  =   1000.,                     ! X and Y grid spacing
   DELTAZ  =     35.,                     ! Z grid spacing (set to 0. to
use ZZ)
   DZRAT   =    1.12,                     ! vertical grid stretch ratio
   DZMAX   =    1000.,                    ! maximum delta Z for vertical
stretch
   ZZ=   0.0,   50.0,  100.0,  200.0,  300.0,  400.0,
                                          ! Vertical levels if DELTAZ = 0
   DTLONG  =     10.,                     ! Coarse grid long timestep
   NRATIO  =      3,                      ! Small timestep ratio
   IMONTH1 =   2,       ! Month
   IDATE1  =  11,       ! Day
   IYEAR1  =  99,       ! Year
   STRTIM  = 7.0,       ! GMT of model TIME = 0.
```

```
                                        ! Nest ratios between this
grid
                                        !  and the next coarser grid.
   NSTRATX =   1, 4,                   ! x-direction
   NSTRATY =   1, 4,                   ! y-direction
   NNDTRAT =   1, 5,                   ! time
   NESTZ = 0,                           ! contort coarser grids if
negative
   NSTRATZ=4,4,3,3,3,3,2,2,2,2,1,1,1,1,  !
   POLELAT   =  -44.0,                  ! Latitude of pole point
   POLELON   =   170.4,                 ! Longitude of pole point
   CENTLAT=    -44.0, -44.0,
   CENTLON=   170.4, 170.4,

                                        ! Grid point on the next
coarser
                                        ! nest where the lower
southwest
                                        ! corner of this nest will
start.
                                        ! IF NINEST or NJNEST = 0,
   NINEST  =   0, 0, 0, 0,              ! i-point
   NJNEST  =   0, 0, 0, 0,              ! j-point
   NKNEST  =   1, 1, 1, 1,              ! k-point
   NNSTTOP =   1,  1,  1, 1,            ! Flag (0-no or 1-yes) if
this
   NNSTBOT =   1,  1,  1, 1,            ! nest goes the top or bottom
of the
                                        ! coarsest nest.

   GRIDU   =  0.,  0.,  0., 0.,         ! u-component for moving
grids
   GRIDV   =  0.,  0.,  0., 0.,         ! v-component for moving
grids
```

MODEL_FILE_INFO

```
 IOUTPUT=       1,                      ! 0-no files, 1-save/dispose
 HFILOUT='3a-basin.h',                  ! history file prefix
 AFILOUT='3a-basin.a',                  ! analysis file prefix
 HFUNITS='h',      AFUNITS='h',         ! history/anal file units
 FRQHIS  =72000.,   FRQANL  =3600.,     ! history/anal file frequency
 INITIAL =   1,                         ! Initial fields -
 IVWIND =       0,          ! initial winds ( only 0 works)

 NUDLAT   =     5,          ! number of points in the lateral bnd
region
 TNUDLAT  =  900.,          ! nudging time scale (s) at lateral
boundary
 TNUDCENT =  0.,            ! nudging time scale (s) in center of
domain
 TNUDTOP  =  7200.,         ! nudging time scale (s) at top of domain
 ZNUDTOP  =  7000.,         ! nudging at top of domain above this
height (m)
```

Printed output controls

```
  FRQPRT  =    3600.,    ! Printout frequency
  FRQIPR  =   10800.,    ! Integral print frequency
  FRQIST  =   10800.,    ! Integral store frequency
```

```
  ISTPFL  =         1,     ! Timestep message frequency flag
  INITFLD =         1,     ! Initial field print flag 0=no print,
1=print
  INPRTFL =         1,     ! Namelist print flag 0=no print, 1=print

                 ! Input topography variables

   SFCFILES = 'NONE',

   ITOPTFLG = 2,2,2,2,              ! 2 - Fill data in "ruser"
   IPCTLFLG = 2,2,2,2,              ! 1 - Interp data from latlon
dataset
   ISSTFLG  = 2,2,2,2,              ! 0 - Interpolate from coarser grid
   IVEGTFLG  = 2,2,2,2,
   SILAVWT  = 1., 1., 1., 1.,      ! Weighting of topo silhouette
averaging
   TOPTWVL  = 4., 4., 4., 4.,      ! Topo wavelength cutoff in filter
   PCTLWVL  = 2., 2., 2., 2.,      ! Land pct wavelength cutoff in
filter
   SSTWVL   = 2., 2., 2., 2.,      ! Land pct wavelength cutoff in
filter
```

MODEL_OPTIONS

```
  NADDSC    =    0, 0, 0, 0,
  NTOPSMTH  =       0,    ! Number of passes for topography smoother
  IZFLAT    =       0,    ! Width of flat margin around domain
```

Numerical schemes

```
  ITMDIFF =       2,    ! 1=forward, 2=leapfrog, 3=hybrid
  NONHYD  =       1,    ! nonhydrostatic=1, hydrostatic=0
  SSPCT   =       0.,   ! Sound speed fraction for the nonhydrostatic
model
  IMPL    =       1,    ! Implicit flag for acoustic model  -  0=off,
1=on
  ICNTEQ  =       2,    ! Hyd - continuity equation - 1 -incomp, 2 -
anelastic
  WTKD    =       0.,   ! Klemp/Durran - current timestep weighting

  ICORFLG =       1,    ! Coriolis flag/2D v-component  -  0=off, 1=on

  IBCTOP =        0,    ! top boundary condition
                        ! 0-wall on top(nonhyd)      2-prognostic sfc
prs(hyd)
                        ! 1-Klemp-Durran(nonhyd/hyd) 3-material
surface(hyd)

  IBND    =       1,    ! Lateral boundary condition flags
  JBND    =       4,    ! 1-Klemp/Wilhelmson, 2-Klemp/Lilly, 3-Orlanski
                        ! 4-cyclic
  CPHAS   =     20.,    ! Phase speed if IBND or JBND = 1
  LSFLG   =      1,     ! Large-scale gradient flag for variables other
than
                        ! normal velocity:
                        ! 0 = zero gradient inflow and outflow
                        ! 1 = zero gradient inflow, radiative b.c.
outflow
                        ! 2 = constant inflow, radiative b.c. outflow
                        ! 3 = constant inflow and outflow
  NFPT    =     10,     ! Rayleigh friction - number of points from
the top
  DISTIM  =    200.,    !                   - dissipation time scale
```

```
  TIMSCL  =      0.,    ! Initial wind spin-up - time scale
  KSPIN   =      33,    !                      - below this level
(velocity)
  KMSPIN  =      10,    !                      - below this level
(momentum)

  IPRSPLT =       0,    ! precipitation time-split scheme - 0=off, 1=on
  IADVL   =       2,    ! Order of advection - Leapfrog - 2 or 4
  IADVF   =       2,    ! Order of advection - Forward - 2 or 6
  IPGRAD  =       1,    ! Pressure gradient scheme for topo.: 1-
transform
                        !                                     2-
interpolate
  FILT4   =       0.,   ! Fourth order filter coefficient (0 - off)
                        !    ( > 0  timestep at which 2 delta waves are
                        !    totally removed)
  FXLONG  =    0.0000,  ! Long filter coefficient 0=off
  FYLONG  =    0.0000,  ! Long filter coefficient 0=off
```

Radiation parameters

```
  ISWRTYP =    1,   ! Shortwave radiation type 0-none, 2-Mahrer/Pielke,
1-Chen
  ILWRTYP =    1,   ! Longwave radiation type 0-none, 2-Mahrer/Pielke,
1-Chen
  RADFRQ  = 1200.,  ! Frequency of radiation tendency update in
seconds
  LONRAD  =    1,   ! Longitudinal variation of shortwave  (0-no, 1-
yes)
```

Cumulus parameterization parameters

```
  NNQPARM =   0, 0, 0, 0,          ! convective parameterization flag
                                   !  0-off, 1-on
  CONFRQ  =   60.,   ! Frequency of conv param. updates in seconds
  WCLDBS  =  .001,   ! vertical motion needed at cloud base for
convection
```

Surface layer and soil parameterization

```
  ISFCL   =      1,    ! surface layer/soil/veg model
                       ! 0-specified surface layer gradients
                       ! 1-soil/vegetation model

  NVGCON  =      8,     ! Vegetation type
                        ! 1 -- Crop/mixed farming         2 -- Short
grass
                        ! 3 -- Evergreen needleleaf tree  4 --
Deciduous
                        ! 5 -- Deciduous broadleaf tree   6 --
Evergreen
                        ! 7 -- Tall grass                 8 -- Desert
                        ! 9 -- Tundra                    10 --
Irrigated crop
                        !11 -- Semi-desert               12 -- Ice
                        !13 -- Bog or marsh              14 -- Inland
water
                        !15 -- Ocean                     16 --
Evergreen
                        !17 -- Deciduous shrub           18 -- Mixed
woodland
  TSEASN  =   298.,     ! Average seasonal temp
  TVGOFF  =     0.,     ! Initial veg temp offset
  VWTRCON =     .000,   ! Initial veg water storage (not working)
```

```
  UBMIN   =   0.25,      ! Minimum U value to use in computing U_*
  PCTLCON =  1.0,        ! constant land percentage if for all domain
  NSLCON  =    3,        ! constant soil type if for all domain
                        !  1=sand              2=loamy sand      3=sandy
loam
                        !  4=silt loam        5=loam            6=sandy
clay loam
                        !  7=silty clay loam 8=clay loam       9=sandy
clay
                        ! 10=silty clay     11=clay           12=peat

  ZROUGH  =  0.05,       ! constant roughness if for all domain
  ALBEDO  =   0.2,       ! constant albedo when not running soil model
  SEATMP  = 289.,        ! constant water surface temperature
  DTHCON  =  -0.,       ! constant surface layer temp gradient for no
soil
  DRTCON  = .000,        ! constant surface layer moist gradient for no
soil
  SOILDZ  =   0.,        ! soil model grid spacing
  SLZ    = -.50,-.40,-.30,-.25,-.20,-.16,
           -.12,-.09,-.06,-.03,  0.,! soil grid levels
  SLMSTR  =  0.3, 0.3, 0.3, 0.3, 0.3,       ! initial soil moisture
             0.3, 0.3, 0.3, 0.3, 0.3, 0.3,
  STGOFF=  -11.,-11.,-11.,-11.,-11.,-11.,-11.,-11.,-11.,-11.,-11.,
```

Eddy diffusion coefficient parameters

```
  IDIFFK = 1,1,1,1,    ! K flag:
                       ! 1 - Horizontal deformation/ Vertical
Mellor-Yamada
                       ! 2 - Anisotropic deformation (horiz and vert
differ)
                       ! 3 - Isotropic deformation (horiz and vert
same)
                       ! 4 - Deardorff TKE (horiz and vert same)
  CSX = .20,      ! Adjustable parameter, deformation horiz. K's
coefficient
  CSZ = .20,      ! Adjustable parameter, deformation vert. K's
coefficient
  XKHKM = 3.,     ! Ratio of horizontal K_h to K_m for TKE or
deformation
  ZKHKM = 1.,     ! Ratio of vertical K_h to K_m for TKE or deformation
  AKMIN= 1.0,     ! Ratio of minimum horizontal eddy viscosity
coefficient
                  !    to typical value from deformation K
```

Microphysics

```
   NLEVEL  =  1,   1, 1, 1,     ! moisture complexity level

   ICLOUD =   0,
   IRAIN  =   0,         ! Microphysics flags
   IPRIS  =   0,         !-------------------
   ISNOW  =   0,         ! where x= R - rain
   IAGGR  =   0,         !          P - pristine crystals
   IGRAUP =   0,         !          S - snow
   IHAIL  =   0,         !          A - aggregates

   CPARM  =  0.,  0.,
   RPARM  =  0.,  0.,         !          G - graupel
   PPARM  =  0.,  0.,         !          H - hail
   SPARM  =  0.,  0.,         ! NIxCNFL = 0 - no species
   APARM  =  0.,  0.,         !           1 - diagnostic concen.
```

```
  GPARM  =  0.,  0.,        !          2 - specified mean diameter
  HPARM  =  0.,  0.,        !          3 - specified y-intercept
                            !          4 - specified concentration
                            !          5 - prognostic concen.
  AMI0   =  0.0000001,  ! minimum crystal mass (gm)
  CON    =   300.0 ,    ! CCN concentration (number/cc)
  THOMO  =  233.0,      ! homogeneous nucleation temperature
```

MODEL_SOUND

```
! Sounding specification
! Flags for how sounding is specified

  IPSFLG=1,     ! specifies what is in PS array
                ! 0 - pressure (mb), 1 - heights (m), PS(1)=sfc
press(mb)

  ITSFLG=2,     ! specifies what is in TS array
                ! 0 - temp(C), 1 - temp(K), 2 - pot. temp(K)

  IRTSFLG=0,    ! specifies what is in RTS array
                ! 0 - dew pnt.(C), 1 - dew pnt.(K), 2 - mix rat(g/kg)
                ! 3 - relative humidity on %, 4 - dew pnt depression(K)

  IUSFLG=0,     ! specifies what is in US and VS arrays
                ! 0 - u,v component(m/s), 1 - umoms-direction, vmoms-
speed

  IUSRC = 0,    !  source of wind profile:
                !  0  - umoms, vmoms, valid at sounding levels (PS)
                !  -1 - usndg, vsndg, valid at model levels    (Z)


    PS=  1031,  100,  200,  300,  400,  500,  600,  700,  761,  800,
          900, 1000, 1100, 1200, 1250, 1300, 1400, 1500, 1600, 1700,
         2750, 2800, 3000, 3100, 3200, 3300, 3350, 3400, 3500, 3600,
         3700, 3800, 3900, 4000, 4100, 4200, 4300, 4400, 4500, 4600,
         4700, 4800, 4900, 4950, 5000, 6000, 7000, 8000, 9000,10000,
        11000,12000,13000,14000,15000,16000,17000,18000,19000,20000,

    TS = 304., 304., 304., 304., 304., 304., 304., 304., 304., 304.,
         304., 304., 304., 304., 304.5,305., 306.,306.5, 307.,
         309.7,310., 310., 310., 310., 310.,310.2,310.3,310.3,310.5,
         310.7,310.8,311., 311.3,312.,312.5, 313.,313.5, 314.,314.5,
         315., 315.5,316., 316.,316.3,320., 323.7,330.6,332.3,336.4,
         338.7,341.,342.6,347.6,373.9,393.8,408.5,430.7,465.5,479.9,

    RTS = 12., 10.4, 9.9,  9.7,  9.3, 9. , 8.7, 8.45, -11.5, -14.1,
          -16.1,-16.7,-12.5,-11.8,-10.,-10.7,-12.3,-24.1,-25.3,-25.5,
          -22.7,-23.1,-18.6,-19.3,-20.,-20.9,-20.9,-20.9,-20.9,-20.9,
          -20.9,-20.7,-20.7,-20.7,-20.7,-20.7,-20.6,-21.1,-22.4,-23.7,
          -25.0,-26.3,-27.5,-27.7,-28.0,-33.8,-39.0,-37.7,-46.0,-51.2,
          -75.,-75.,-75.,-75.,-75.,-75.,-75.,-75.,-75.,-75.,

  US =  0.01, 0.01, 0.01, 0.01, 0.01, 0.01, 0.01, 0.01, 0.01, 0.01,
        0.01, 0.01, 0.01, 0.01, 0.01, 0.01, 0.01, 0.01, 0.01, 0.01,
        0.01, 0.01, 0.01, 0.01, 0.01, 0.01, 0.01, 0.01, 0.01, 0.01,
        0.01, 0.01, 0.01, 0.01, 0.01, 0.01, 0.01, 0.01, 0.01, 0.01,
        0.01, 0.01, 0.01, 0.01, 0.01, 0.01, 0.01, 0.01, 0.01, 0.01,
        0.01, 0.01, 0.01, 0.01, 0.01, 0.01, 0.01, 0.01, 0.01, 0.01,
        0.01, 0.01, 0.01, 0.01, 0.01, 0.01, 0.01, 0.01, 0.01, 0.01,
```

```
 VS =  0.,0.,0.,0.,0.,0.,0.,0.,0.,0.,0.,0.,0.,0.,0.,0.,0.,0.,0.,0.,
       0.,0.,0.,0.,0.,0.,0.,0.,0.,0.,0.,0.,0.,0.,0.,0.,0.,0.,0.,0.,
       0.,0.,0.,0.,0.,0.,0.,0.,0.,0.,0.,0.,0.,0.,0.,0.,0.,0.,0.,0.,
       0.,0.,0.,0.,0.,0.,0.,0.,0.,0.,0.,0.,0.,0.,0.,0.,0.,0.,0.,0.,

 USNDG = 0.,    ! Wind components if IUSRC= -1
 VSNDG = 0.,    !
 KMEAN1 = 0,    !  lower model level for calculation of (umean,vmean)
 KMEAN2 = 0,    !  upper model level for calculation of (umean,vmean)

 UMEAN = 0.0,   !  u-component for Galilean transformation
 VMEAN = 0.0,   !  v-component for Galilean transformation
```

MODEL_USER

```
  ICONV  = 0,     ! = 1 Kuo cumulus parameterization, = 2 Grell scheme
  IVEGE  = 0,     ! = 1 for batstobats, = 0 for usgstobats
  ISFCF  = 1,     ! = 1 for ascii surface file, = 0 for default values
  IFDDA  = 0,     ! = 1 to activate four-dimensional data assimilation
  ITOUT  = 1,     ! = 1 to activate output of tendency terms
  ITGRID = 1,     ! = nest grid of subdomain (tendency terms)
  ITIB   = 182,     ! = beg i-node of subdomain (tendency terms)
  ITIE   = 465,     ! = end i-node of subdomain (tendency terms)
  ITJB   = 1,     ! = beg j-node of subdomain (tendency terms)
  ITJE   = 5,     ! = end j-node of subdomain (tendency terms)
  ITKB   = 1,     ! = beg k-node of subdomain (tendency terms)
  ITKE   = 20,     ! = end k-node of subdomain (tendency terms)
  FRQIT  = 900., ! = frequency of tendency output
```

MODEL_PRINT

```
  ! Specifies the fields to be printed during the simulation
  NPLT  =  8,                ! Number of fields to be printed at each
time
                             !    for various cross-sections (limit of
50)
  IPLFLD = 'THETA','TFZ','QFZ','SLM','RLONG','RSHORT',
           'TG','TVEG',
                             ! Field names - see table below
  PLFMT(1) = '3PF7.1',     ! Format specification if default is
unacceptable
  PLFMT(2) = '3PF7.1',      ! Format specification if default is
unacceptable
  PLFMT(3) = '6PF7.1',      ! Format specification if default is
unacceptable
  PLFMT(5) = '0PF7.1',
  PLFMT(6) = '0Pf7.1',
  PLFMT(7) = '0Pf7.1',
  XSCTN = 3,3,3,3,3,3,3,3,3,3,3,
                             ! Cross-section type (1=XZ, 2=YZ, 3=XY)
  ISBVAL = 1,1,1,1,1,1,1,1,1,1,1,1,1,
                             ! Grid-point slab value for third
direction
! The following variables can also be set in the $PRNT namelist:  IAA,
! IAB, JOA, JOB, NAAVG, NOAVG, PLTIT, PLCONLO, PLCONHI, and PLCONIN.

C      'UP'     - UP(M/S)      'RC'    - RC(G/KG)     'PCPT' - TOTPRE
C      'VP'     - VP(M/S)      'RR'    - RR(G/KG)     'TKE'  - TKE
C      'WP'     - WP(CM/S)     'RP'    - RP(G/KG)     'HSCL' - HL(M)
C      'PP'    - PRS(MB)      'RA'    - RA(G/KG)     'VSCL' - VL(M)
C      'THP'   - THP(K)
C      'THETA'- THETA(K)      'RL'    - RL(G/KG)     'TG'   - TG (K)
C      'THVP'  - THV'(K)      'RI'    - RI(G/KG)     'SLM'  - SLM (PCT)
C      'TV'    - TV(K)        'RCOND'- RD(G/KG)     'CONPR'- CON RATE
```

```
C     'RT'    - RT(G/KG)     'CP'    - NPRIS        'CONP' - CON PCP
C     'RV'    - RV(G/KG)     'RTP'   - RT'(G/KG)    'CONH' - CON HEAT
C                                                   'CONM' - CON MOIS
C     'THIL' - Theta-il (K)    'TEMP' - temperature (K)
C     'TVP'   - Tv' (K)        'THV'   - Theta-v     (K)
C     'RELHUM'-relative humidity (%)         'SPEED'- wind speed (m/s)
C     'FTHRD'- radiative flux convergence (??)
C     'MICRO'- GASPRC
C     'Z0'    - Z0 (M)       'ZI'    - ZI (M)       'ZMAT' - ZMAT (M)
C     'USTARL'-USTARL(M/S) 'USTARW'-USTARW(M/S) 'TSTARL'-TSTARL (K)
C     'TSTARW'-TSTARW(K)   'RSTARL'-RSTARL(G/G) 'RSTARW'-RSTARW(G/G)
C     'UW'    - UW  (M*M/S*S)                    'VW'    - VW (M*M/S*S)
```